



Universität Hamburg  
DER FORSCHUNG | DER LEHRE | DER BILDUNG

FAKULTÄT  
FÜR MATHEMATIK, INFORMATIK  
UND NATURWISSENSCHAFTEN

# Development and Study of Refractive Phase Retrieval and X-ray Multibeam Ptychography

## Dissertation

zur Erlangung des Doktorgrades  
an der Fakultät für Mathematik,  
Informatik und Naturwissenschaften  
Fachbereich Physik  
der Universität Hamburg

vorgelegt von  
Felix Wittwer  
aus Zittau

Hamburg  
2020

The work described in this thesis was done at the Photon Science division of Deutsches Elektronen-Synchrotron, a Research Centre of the Helmholtz Association.

Gutachter der Dissertation:	Prof. Dr. Christian G. Schroer Prof. Dr. Peter Modregger
Zusammensetzung der Prüfungskommission:	Prof. Dr. Daniela Pfannkuche Prof. Dr. Christian G. Schroer Prof. Dr. Peter Modregger Dr. habil. Thomas Keller Prof. Dr. Dorota Koziej
Vorsitzende der Prüfungskommission:	Prof. Dr. Daniela Pfannkuche
Datum der Disputation:	19.03.2021
Vorsitzender Fach-Promotionsausschusses PHYSIK:	Prof. Dr. Günter H. W. Sigl
Leiter des Fachbereichs PHYSIK:	Prof. Dr. Wolfgang Hansen
Dekan der Fakultät MIN:	Prof. Dr. Heinrich Graener

# Abstract

The advent of phase retrieval techniques has increased the resolution in X-ray microscopy by nearly an order of magnitude. With conventional imaging, X-ray microscopes cannot reach their full potential due to the lack of strong focusing options for X-rays. While the wavelength of X-rays is a thousand times smaller than visible light, the resolution of X-ray microscopes is only ten times smaller than the resolution of light microscopes. Phase retrieval algorithms are not limited by the numerical aperture of the focusing optics and can therefore resolve much smaller features.

Conventional phase retrieval algorithms reconstruct the complex transmission function of the sample. Most microscopic samples are nearly transparent for X-rays and are only visible through their phase contrast. The phase shift however is  $2\pi$  periodic, which means a specific phase value cannot be distinguished from another one that is larger or smaller by  $2\pi$ . This phenomenon is called phase wrapping and is problematic for samples that have a maximum phase shift of more than  $2\pi$ . Phase unwrapping algorithms aim to solve these ambiguities, but are not always successful, because phase wraps can lead to artefacts and phase singularities during the phase retrieval. Phase wrapping is especially challenging for tomography, because the wrapped phase is not a simple projection and also not proportional to the sample density.

In this thesis, new algorithms are developed that reconstruct the projected refractive index of the sample instead of the complex transmission. The projected refractive index is in a trivial way directly proportional to the refractive index of the sample. In contrast to the phase of the transmission function, the projected refractive index requires no phase unwrapping, as it is not limited to a specific range. This thesis presents three refractive algorithms for three widely used phase retrieval techniques: ptychography, holography and coherent diffractive imaging. All three refractive algorithms are demonstrated and evaluated on simulated data sets, in the case of refractive ptychography also on two experimental data sets. Refractive ptychography and refractive holography surpass conventional algorithms for samples with a phase shift of more than  $2\pi$ . In the case of refractive coherent diffractive imaging, the new algorithm surpasses the conventional one even for samples with no phase wrapping.

In the second part of this thesis, a new method to scan large samples is presented. Due to the long scan times, large samples are problematic to measure with scanning techniques such as ptychography. To scan large samples in a shorter time, Bevis *et al.* have developed multibeam ptychography, a technique that uses multiple simultaneous beams [*Ultramicroscopy*, **184**, 164 (2018)]. This thesis presents a set-up for X-ray multibeam ptychography that allows arbitrary numbers and geometries of multibeams. This is made possible through the use of a lens array manufactured with two-photon lithography. The lens array is evaluated for a two and a six beam geometry using experimental data. Compared to a single beam, the multibeam set-up scans the same area up to three times faster.



# Zusammenfassung

Das Aufkommen von Methoden zur Phasenrückgewinnung hat die Auflösung in der Röntgenmikroskopie um fast eine Größenordnung verbessert. Durch das Fehlen von stark fokussierenden Röntgenoptiken können Röntgenmikroskope mit konventioneller Bildgebung nicht ihr volles Potenzial entfalten. Zwar ist die Wellenlänge von Röntgenstrahlen tausendmal kleiner als die von sichtbarem Licht, die Auflösung von Röntgenmikroskopen übertrifft die Auflösung von Lichtmikroskopen jedoch nur um das Zehnfache. Verfahren zur Phasenrückgewinnung sind nicht durch die numerische Apertur der Optiken begrenzt und können daher sehr viel kleinere Details auflösen.

Konventionelle Algorithmen zur Phasenrückgewinnung rekonstruieren die komplexe Transmissionsfunktion der Probe. Die meisten Proben in der Mikroskopie sind für Röntgenstrahlen nahezu transparent und nur durch ihren Phasenkontrast sichtbar. Der Phasenschub ist jedoch  $2\pi$  periodisch. Das bedeutet, dass ein bestimmter Phasenwert nicht von einem anderen unterschieden werden kann, der sich genau um  $2\pi$  unterscheidet. Dieses Phänomen führt zu Sprüngen in der Phase und ist problematisch für Proben die einen maximalen Phasenschub von mehr als  $2\pi$  aufweisen. Sogenannte *phase unwrapping* Verfahren zielen darauf ab, diese Mehrdeutigkeiten zu lösen, sind aber nicht immer erfolgreich weil Phasensprünge zu Artefakten und Phasensingularitäten in der Rekonstruktion führen können. Die Mehrdeutigkeit der Phase ist für die Tomographie eine besondere Herausforderung, da die Phasensprünge keine einfache Projektion sind und auch nicht proportional zur Probendichte sind.

In dieser Arbeit werden neue Algorithmen entwickelt, die anstelle der komplexen Transmission den projizierten Brechungsindex der Probe rekonstruieren. Der projizierte Brechungsindex ist auf triviale Weise direkt proportional zum Brechungsindex der Probe. Im Gegensatz zur Phase der Transmissionfunktion ist die Projektion des Brechungsindex nicht auf *phase unwrapping* angewiesen, da sie nicht auf einen bestimmten Bereich beschränkt ist. Diese Arbeit stellt drei refraktive Algorithmen für drei weitverbreitete Phasenrückgewinnungstechniken vor: Ptychographie, Holographie und kohärente diffraktive Bildgebung. Alle drei Algorithmen werden an simulierten Datensätzen demonstriert, im Falle der refraktiven Ptychographie zusätzlich an zwei experimentellen Datensätze. Die refraktive Ptychographie und die refraktive Holographie übertreffen den jeweiligen konventionellen Algorithmus für Proben die Phasensprünge aufweisen. Im Fall der refraktiven kohärenten diffraktiven Bildgebung übertrifft der neue Algorithmus den konventionellen sogar für Proben ohne

Phasensprünge.

Im zweiten Teil dieser Arbeit wird eine neue Methode zum Scannen großer Proben vorgestellt. Aufgrund der langen Scanzeiten sind große Proben problematisch für Rastertechniken wie die Ptychographie. Um große Proben in kürzerer Zeit zu scannen, haben Bevis *et al.* die Mehrstrahl-Ptychographie entwickelt, eine Technik, bei der mehrere Strahlen die Probe gleichzeitig scannen [*Ultramicroscopy*, **184**, 164 (2018)]. In dieser Arbeit wird ein Aufbau für Röntgen-Mehrstrahl-Ptychographie vorgestellt, der eine beliebige Anzahl und Geometrie von Strahlen erlaubt. Ermöglicht wird dies durch die Verwendung eines Linsenarrays, das mit Zwei-Photonen-Lithographie hergestellt wurde. Das Linsenarray wird in einer Zwei- und einer Sechs-Strahl-Geometrie experimentell getestet. Im Vergleich zu einem Einzelstrahl scannt die Mehrstrahlanordnung die gleiche Fläche bis zu dreimal schneller.

# Contents

<b>1</b>	<b>Introduction</b>	<b>1</b>
1.1	Outline . . . . .	2
1.2	Contributions . . . . .	3
<b>2</b>	<b>X-rays</b>	<b>5</b>
2.1	Wave theory . . . . .	5
2.1.1	Wave propagation . . . . .	5
2.1.2	Coherence . . . . .	8
2.1.3	Complex index of refraction . . . . .	11
2.2	Synchrotron radiation . . . . .	13
2.2.1	Brightness . . . . .	13
2.2.2	Synchrotron light sources . . . . .	13
2.2.3	P06 Beamline . . . . .	14
2.3	X-ray optics . . . . .	16
2.3.1	KB-mirrors . . . . .	16
2.3.2	Fresnel zone plates . . . . .	17
2.3.3	Compound refractive lenses . . . . .	18
2.4	Phase problem . . . . .	20
<b>3</b>	<b>Ptychography</b>	<b>21</b>
3.1	Classic ptychography . . . . .	21
3.2	Parallel ptychography . . . . .	26
3.3	Upsampling ptychography . . . . .	27
3.4	Momentum accelerated ptychography . . . . .	29
3.5	Practical ptychography implementation . . . . .	32
3.5.1	Resolution and field of view in ptychography . . . . .	32
3.5.2	Position refinement . . . . .	32
3.5.3	Software . . . . .	33
<b>4</b>	<b>Refractive Ptychography</b>	<b>35</b>
4.1	Basics . . . . .	35
4.2	Simulation tests . . . . .	36
4.3	Zeolite experiment . . . . .	40
4.4	Micrometeorite . . . . .	45

4.5	Conclusion	48
<b>5</b>	<b>Refractive Phase Retrieval</b>	<b>51</b>
5.1	Inline near-field holography	51
5.1.1	Reconstruction algorithm	52
5.1.2	Numerical simulation	54
5.2	Refractive coherent diffractive imaging	57
5.3	Conclusion	63
<b>6</b>	<b>Multibeam X-ray ptychography</b>	<b>67</b>
6.1	Multibeam algorithm	68
6.2	X-ray lenses by additive 3D nano-manufacturing	70
6.3	Multibeam experiments	73
6.3.1	2-Beam experiment	74
6.3.2	Sensitivity to incorrect probe separation	77
6.3.3	6-Beam experiment	78
6.4	Conclusion	82
<b>7</b>	<b>Conclusion and Outlook</b>	<b>83</b>
<b>A</b>	<b>Appendix</b>	<b>87</b>
A.1	Wirtinger derivatives	87
A.2	Align reconstructions and remove ambiguities	88
A.3	Calculate reconstruction errors	89
<b>B</b>	<b>Abbreviations</b>	<b>91</b>
	<b>Bibliography</b>	<b>93</b>
	<b>List of Publications</b>	<b>101</b>

# 1 Introduction

Modern synchrotron radiation sources are multi tools for science, providing a wide range of analytic methods and techniques [Sch+19b]. Synchrotron radiation helps to answer questions from various scientific fields ranging from chemistry [GWD13] and biology [Wei+12] to material science [Zha+17] and cultural heritage [Jan+13]. Imaging samples in high-resolution is often crucial to solve these questions [SA10]. Compared to classical light microscopy, X-ray microscopy offers superior resolution owing to the shorter wavelength of X-rays.

The two main characteristics of X-rays, their short wavelength and weak interaction, make X-rays attractive for imaging as this allows to image samples in situ with high-resolution. On the other hand, those same characteristics make it difficult to build high-performance X-ray optics [SL12]. This lack of strong focusing options limits the resolution in X-ray microscopy and prevents the direct imaging of atoms. In lieu of real imaging lenses, virtual lenses are used to surpass the physical limitations. The virtual lenses use the massive computing power of modern graphics card and multi-core processors to calculate in silicon what is inaccessible in the real world [CN10].

The wave scattered by the sample can only be virtually propagated if the amplitude and phase of the wave are known. However, X-ray detectors only measure the amplitude of the wave, the phase information is lost. To circumvent this difficulty, Dennis Gabor invented his *new microscopic principle*, which recovers the missing phase information and reconstructs the sample image [Gab48]. Gabor's method is also known as inline near-field holography and belongs to a group of techniques called phase retrieval algorithms, all of which are designed to recover the phase of the scattered wave from the amplitude measurements alone [She+15].

Most phase retrieval algorithms reconstruct both the absorption and the phase shift of the sample. In general, the phase shift is more important as many microscopic samples absorb X-rays only weakly. This can be problematic because the phase shift is only defined modulo  $2\pi$  and larger phase shifts are wrapped. Especially in computed tomography, where many projections from different angles are combined to create a 3D reconstruction of the sample, phase projections must be unwrapped before they can be used [Gui+11]. The success of the phase unwrapping depends on the reconstruction quality of the phase retrieval [Sto+15].

The unwrapped phase shift is proportional to the projected refractive index of the sample [Dia+12]. If phase retrieval algorithms could reconstruct this projection

directly, any conversion or phase unwrapping could be completely avoided. Chowdhury *et al.* developed such a refractive algorithm for Fourier ptychography [Cho+19]. The first part of this thesis expands this idea by developing refractive algorithms for more phase retrieval methods, namely ptychography, near-field holography and coherent diffractive imaging.

Refractive phase retrieval is especially advantageous for large samples that are tens or hundreds of micrometer in size. That is to say, as the phase shift of these samples is wrapped multiple times, conventional algorithms are prone to artefacts in the reconstruction. While refractive phase retrieval solves this problem, large samples also pose a challenge for scanning techniques such as ptychography. Because beamtime at synchrotron radiation sources is scarce, only a small number of large scans can be measured.

To accelerate ptychographic scans, Bevis *et al.* developed multibeam ptychography [Bev+18]. By scanning the sample with multiple parallel beams, large samples can be scanned in a fraction of the time that was previously required. Following the pioneering work of Hirose *et al.* on X-ray multibeam ptychography [Hir+20], the second part of this thesis concerns the development of an advanced, more flexible scheme to create X-ray multibeams.

## 1.1 Outline

This thesis is structured as follows: In Chapter 2, an overview on the properties and interactions of X-rays is given. In Chapter 3, a discussion of ptychography is presented containing a derivation of the commonly used ePIE algorithm and how to adapt ptychography to different experimental conditions.

In Chapter 4, the new refractive ptychography algorithm is developed and tested. Three tests are presented: a simulated experiment, a scan of a 2  $\mu\text{m}$  zeolite particle and a scan of a 80  $\mu\text{m}$  micrometeorite. In the first two tests, the respective phase shift of the sample is small and shows only weak or no phase wrapping. Consequently, the refractive reconstruction is nearly identical to a conventional reconstruction. In contrast, the micrometeorite has a maximum phase shift of close to 15 rad and the novel refractive ptychography is able to reconstruct the sample with a notably improved quality compared to conventional ptychography.

In Chapter 5, the idea of refractive phase retrieval is expanded with the development of refractive algorithms for holography and coherent diffractive imaging. The newly developed algorithms are each tested on a simulated experiment. Refractive holography fulfils the expectations and reconstructs the simulated sample without phase wraps or artefacts. Significantly, even though the test sample for refractive CDI has only a weak phase shift with no phase wrappings, the refractive reconstruction is

still reliable closer to the ground truth than the conventional reconstruction.

In Chapter 6, the novel multibeam set-up is presented. In previous works a single focusing optic was used to focus all beams. Due to the small numerical aperture of X-ray optics, this limits the maximum separation between the individual beams and in consequence the scan speed-up. The main distinction of this thesis is the use of a lens array, manufactured with two-photon lithography, where each of the lenses focuses one beam. This allows to increase the number of beams and enlarge the distance between the beams. The performance of the lens array is verified with two scans using two and six multibeams. The multibeam scans achieve a respective speed-up of 1.8 and 3 compared to a single beam scan.

All the results are summarized in chapter 7 together with an outlook on the possible future developments of refractive phase retrieval and X-ray multibeam ptychography.

## 1.2 Contributions

The experiments presented in this thesis are the result of a team effort; this section serves to explicitly describe for each chapter the contributions from the author, Felix Wittwer, and from collaborations.

### Chapter 4

- Derived the refractive ptychography algorithm and implemented the refractive reconstruction code for ptycho; performed simulations.
- Assisted in the measurement of the zeolite particle during the beamtime of Thomas Sheppard; reconstructed and analysed the scan.
- Reconstructed and analysed the micrometeorite scan.

### Chapter 5

- Derived the refractive holography algorithm, implemented the reconstruction code and performed simulations.
- Derived the reconstruction algorithm for refractive coherent diffractive imaging, implemented the reconstruction code and performed simulations.

### Chapter 6

- Planned the multibeam experiment and wrote the beamtime proposal in collaboration with Mikhail Lyubomirskiy.

- Performed the experiment together with Mikhail Lyubomirskiy, Maik Kahnt, Martin Seyrich, Frieder Koch and support from the beamline scientists.
- Reconstructed and analysed the data.

## 2 X-rays

X-ray radiation is the part of the electromagnetic spectrum with wavelengths between 10 nm and 10 pm. X-ray photons have a corresponding energy of 100 eV to several 100 keV. All experiments in this thesis used hard X-rays between 5 keV to 20 keV at the P06 beamline at the synchrotron light source PETRA III in Hamburg. This chapter gives an overview of the wave properties of X-rays, synchrotron radiation, different X-ray focusing optics and the P06 beamline. A more extensive overview is given by Als-Nielsen & McMorrow [AM11].

### 2.1 Wave theory

In this section, we outline how the propagation of X-rays can be described in the paraxial approximation, how coherence distinguishes different X-ray sources and how the interaction between X-rays and matter can be described with the complex index of refraction. A theoretical description of optical wave theory can be found in Born & Wolf [BW99].

#### 2.1.1 Wave propagation

In general, the propagation and evolution of electromagnetic waves is described by Maxwell's equations. However, finding a closed-form solution for the propagation is often difficult or impossible. Therefore, we will approximate the equations to find simpler solutions. As we are only interested in the propagation of X-rays inside a homogeneous medium that shows no polarization effects and all involved angles are small, we can replace the full vectorial equations by a single scalar wave equation. The X-rays at a synchrotron light source propagate mostly through air or vacuum, which fulfil these criteria.

We base our description of wave propagation on the Huygens-Fresnel principle, which states that every point of the wavefront is a source of a spherical secondary wave and all these secondary waves interfere and overlap to form the new wavefront. This principle is valid for all length scales much larger than the wavelength. In mathematical form, the principle describes how a wave  $\psi$  propagates from the  $(\xi, \eta)$

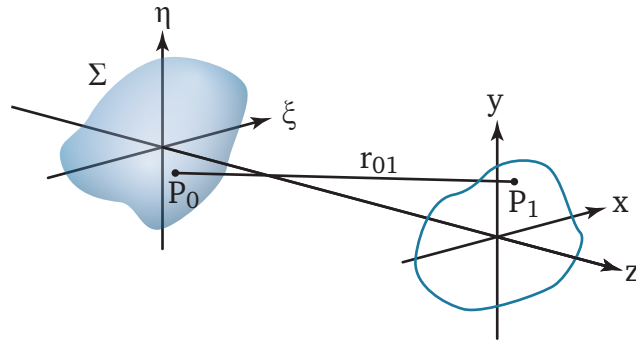


**Figure 2.1 Huygens-Fresnel principle.** Each point  $P_0$  in the wavefront  $\Sigma$  generates a secondary wave. The wavefront in plane  $z$  is formed by the sum of all the secondary waves. Adapted from [Goo05].

plane at  $z = 0$  to a point  $\mathbf{r} = (x, y, z)$ ,

$$\psi(\mathbf{r}) = \frac{z}{i\lambda} \iint_{\Sigma} \psi(\xi, \eta, 0) \cdot \frac{e^{ikr_{01}}}{r_{01}^2} d\xi d\eta. \quad (2.1)$$

The distance  $r_{01}$  is given by

$$r_{01} = \sqrt{(x - \xi)^2 + (y - \eta)^2 + z^2}. \quad (2.2)$$

A detailed derivation of Equation 2.1 is given by Goodman in [Goo05].

Equation 2.1 can be calculated in a closed form only for special cases and in general must be calculated computationally. The propagation of a field of  $N \times N$  elements requires on the order of  $N^4$  calculations, due to the evaluation of the double integral for each point. Therefore, using Equation 2.1 in iterative reconstructions, which require thousands of propagations, is impractical. As the typical propagation distances for ptychography and holography are larger than the typical dimensions of the wavefield, we can approximate  $r_{01}$  to quicken the calculation. The first approximation, called Fresnel propagation, is best suited for intermediate propagation distances. For even longer distances, the approximation can be simplified even further using the Fraunhofer propagation.

### Fresnel propagation

If the propagation distance  $z$  is much larger than the extent of the wavefield, then only points close to the optical axis contribute notably to the propagation. In this paraxial approximation, the square root calculation of  $r_{01}$  can be simplified using the

linear term of its binomial expansion, yielding

$$r_{01} \approx z \cdot \left[ 1 + \frac{1}{2} \left( \frac{x - \xi}{z} \right)^2 + \frac{1}{2} \left( \frac{y - \eta}{z} \right)^2 \right]. \quad (2.3)$$

We use Equation 2.3 to replace  $r_{01}$  in the exponential in Equation 2.1. As the denominator in Equation 2.1 is dependent on  $r_{01}^2$ , we can simplify Equation 2.3 even further by dropping all terms except  $z$ . Using these two approximations, we have

$$\psi_z(x, y) = \frac{e^{ikz}}{i\lambda z} \iint_{\Sigma} \psi_0(\xi, \eta) \exp \left\{ \frac{ik}{2z} [(x - \xi)^2 + (y - \eta)^2] \right\} d\xi d\eta. \quad (2.4)$$

Equation 2.4 is a convolution

$$\psi_z(x, y) = \iint_{\Sigma} \psi_0(\xi, \eta) h_z(x - \xi, y - \eta) d\xi d\eta \quad (2.5)$$

of the original wavefield  $\psi_0$  with the Fresnel kernel

$$h_z(x, y) = \frac{e^{ikz}}{i\lambda z} \exp \left[ \frac{ik}{2z} (x^2 + y^2) \right]. \quad (2.6)$$

Convolutions can be quickly calculated with Fourier transforms using the convolution theorem. This theorem states that the Fourier transform of the convolution of two functions is equal to the pointwise product of the Fourier transforms of the individual functions. For our situation, this means

$$\mathcal{F}(\psi_z) = \mathcal{F}(\psi_0 * h_z) = \mathcal{F}(\psi_0) \cdot \mathcal{F}(h_z). \quad (2.7)$$

We can therefore write the Fresnel propagation as

$$\psi_z = \mathcal{P}_z(\psi) = \mathcal{F}^{-1}(\mathcal{F}(\psi_0) \cdot H_z), \quad (2.8)$$

where  $H_z$  is the Fourier transform of the Fresnel kernel  $h_z$

$$H_z = e^{ikz} \exp(-i\lambda z [q_X^2 + q_Y^2] / 2), \quad (2.9)$$

with the reciprocal space variables  $q_X$  and  $q_Y$ . One thing to note is that complex conjugating the Fresnel kernel

$$H_z^* = e^{-ikz} \exp(i\lambda z [q_X^2 + q_Y^2] / 2) = H_{-z} \quad (2.10)$$

is the same as propagating in the opposite direction.

### Fraunhofer propagation

For the longest distances, when the propagation distance is much greater than the extensions of the wavefield

$$z \gg \frac{\max(\xi^2 + \eta^2)}{\lambda}, \quad (2.11)$$

the terms in Equation 2.3 that do not depend on  $x$  or  $y$  vanish. Conversely, only the terms that are at most linearly dependent on  $\xi$  and  $\eta$  contribute to the distance

$$r_{01} \approx z + \frac{x^2 + y^2}{2z} - \frac{x\xi}{z} - \frac{y\eta}{z}. \quad (2.12)$$

The propagated wavefield is then given by

$$\psi_z(x, y) = \frac{e^{ikz} \cdot e^{i\frac{k}{2z}(x^2+y^2)}}{i\lambda z} \iint_{\Sigma} \psi_0(\xi, \eta) \exp\left[-\frac{ik}{\lambda z}(x\xi + y\eta)\right] d\xi d\eta. \quad (2.13)$$

If we replace  $x$  and  $y$  with the reciprocal space variables

$$\begin{aligned} q_x &= kx/z \\ q_y &= ky/z, \end{aligned} \quad (2.14)$$

then the propagated wavefield becomes the Fourier transform of the original wave, multiplied with a phase term

$$\psi_z(q_x, q_y) = \frac{e^{ikz} \cdot e^{i\frac{z}{2k}(q_x^2+q_y^2)}}{i\lambda z} \iint_{\Sigma} \psi_0(\xi, \eta) \exp[-i(q_x\xi + q_y\eta)] d\xi d\eta, \quad (2.15)$$

$$= \frac{e^{ikz} \cdot e^{i\frac{z}{2k}(q_x^2+q_y^2)}}{i\lambda z} \cdot \mathcal{F}(\psi_0). \quad (2.16)$$

This is the far-field or Fraunhofer propagation. The prefactor is often omitted.

### 2.1.2 Coherence

The frequency of X-rays is in the Peta- or even Exahertz range, due to their short wavelength. Detectors cannot operate at these frequencies and cannot directly detect the oscillations of the X-ray waves. X-ray detectors always average over many oscillation periods and only measure the mean strength of the field, even at the shortest possible exposures. Wave phenomena such as diffraction and interference are only visible if different parts of the wave have a constant phase relation over time and space. If the relative phase changes, then the averaging in the detector blurs the constructive and destructive interference. The stability of the phase relation is measured by correlating different parts of the wave. This is mostly done in two different ways. In the first, a

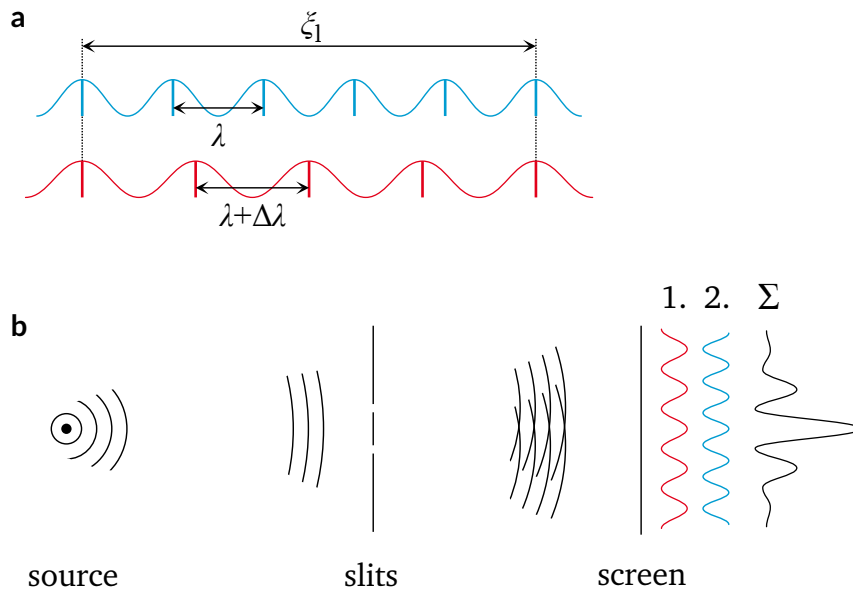


**Figure 2.2 Lateral coherence.** **a** Two waves with wavelengths  $\lambda$  and  $\lambda + \Delta\lambda$  are in phase again after one coherence length  $\xi_l$ . **b** A polychromatic source emits white light. A double slit creates two beams that overlap on the screen and form the diffraction pattern. Each wavelength generates a different diffraction pattern, which add up incoherently. At the centre of the pattern, they are in phase and create a maximum. With growing distance, the patterns are more and more out of phase and the contrast vanishes. Adapted from [Sch14].

point in space is fixed and the correlation is calculated solely for the time evolution. In the second, the correlation is calculated between different points of the wavefield at the same time. A rigorous description of optical coherence can be found in Born & Wolf [BW99].

### Temporal/Lateral coherence

The first way to calculate the correlation is called temporal coherence because it is determined by the time evolution of the wave. For this, the wave is correlated for different time delays at a fixed point in space. The time over which the waves are correlated is called the coherence time  $\tau_l$ . During this time, the wave moves a certain distance

$$\xi_l = c\tau_l, \quad (2.17)$$

called the lateral coherence length. For the situation illustrated in Figure 2.2a, where two monochromatic waves propagate in parallel, they are in phase every  $N$  and  $N + 1$  wavelengths respectively. The coherence length is therefore

$$N(\lambda + \Delta\lambda) = \xi_l = (N + 1)\lambda \quad (2.18)$$

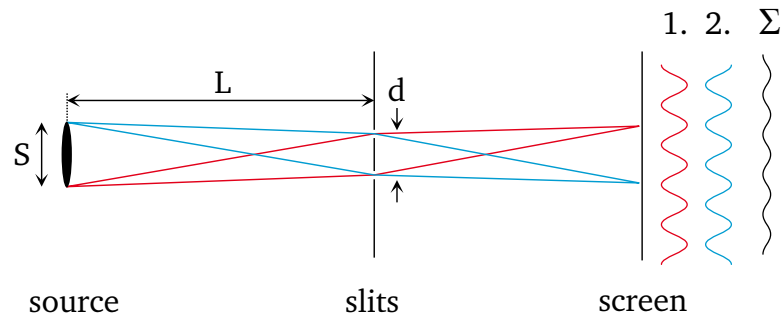


**Figure 2.3 Transverse coherence.** Each point of a monochromatic, chaotic source emits waves independent of all other points. Due to this, the waves are incoherent with each other. Because of the different geometry and direction of each wave, they each create their own diffraction pattern. For thin samples, the different patterns are simply transversally shifted. Overall, this blurs the measured diffraction pattern and can possibly eliminate any fringes. Adapted from [Sch14].

$$N = \lambda/\Delta\lambda \quad (2.19)$$

For narrow bandwidths, where  $\lambda \gg \Delta\lambda$ , the number of periods  $N$  is very large and nearly identical to  $N + 1$ . Therefore, the coherence length can be approximated as

$$\xi_l = \frac{\lambda}{\Delta\lambda} \lambda. \quad (2.20)$$

For diffraction experiments, the lateral coherence length limits the possible size of the samples. For constructive and destructive interference in a detector pixel, it is crucial that the length difference between the path to the closest and the path to the furthest point of the sample is smaller than the coherence length. Third-generation synchrotron light sources typically use silicon-111 monochromators that have a bandwidth  $\Delta E/E$  of around  $10^{-4}$ . For  $1 \text{ \AA}$  X-rays the lateral coherence length is thus about  $1 \mu\text{m}$ .

### Spatial/transverse coherence

Previously we described how the correlations change for a fixed point in space at different time delays. Now, we keep the time delay fixed and look how the correlations change between different points along the wavefront. The spatial coherence is mostly influenced by the apparent size of the radiation source. The reason lies in the mostly chaotic nature of the emission process in typically sources. The radiation in the sun, an X-ray tube or a synchrotron is emitted by individual electrons, which radiate independently of each other. The emission processes are all uncorrelated. In contrast, a laser synchronizes the elementary emission processes via stimulated emission. Subsequently, lasers exhibit a high degree of transverse coherence.

To calculate the coherence length, we consider the classic double-slit experiment of Young, illustrated in Figure 2.3. A monochromatic, extended source emits waves with wavelength  $\lambda$  that are diffracted at two slits that are a distance  $d$  apart. In the paraxial approximation, every point of the source creates the same, but shifted, diffraction pattern on the screen. Since the emission of each point is statistically independent of all other points, the different diffraction patterns show no interference with each other. Viewed from the slits, the faraway source appears under an angular size of

$$\alpha = \frac{S}{L}. \quad (2.21)$$

On the other side of the slits, the fringe maxima of the diffraction pattern occur for integers  $n$  under angles

$$\theta = \frac{n\lambda}{d}. \quad (2.22)$$

Hence, the angular separation between two adjacent fringes is  $\Delta\theta = \lambda/d$ . The diffraction patterns created by the different points on the source are correlated, if the source size  $\alpha$  is smaller than the angular separation  $\Delta\theta$  of the fringes. The coherence length  $\xi_t$  is the characteristic slit separation where the two angles are equal

$$\frac{S}{L} = \frac{\lambda}{\xi_t} \Rightarrow \xi_t = \frac{\lambda L}{S}. \quad (2.23)$$

For a typical nanofocusing beamline at a third-generation synchrotron light source, the experiment is about 100 m away from the X-ray source. The electrons that circle inside the storage ring and create the X-rays are grouped into bunches. Each electron bunch is about 100  $\mu\text{m}$  wide and slightly less than 10  $\mu\text{m}$  high. Consequently, the coherence lengths for 1  $\text{\AA}$  X-rays at the experiment are around 100  $\mu\text{m}$  in the horizontal direction and 1000  $\mu\text{m}$  in the vertical one.

### 2.1.3 Complex index of refraction

The refractive index for X-rays is marginally smaller than one and is commonly written as

$$n = 1 - \delta + i\beta, \quad (2.24)$$

with small, but positive  $\delta$  and  $\beta$  [Tho+09]. The refractive index decrement  $\delta$  is on the order of  $10^{-5}$  to  $10^{-6}$  and the imaginary part  $\beta$  is typically even smaller.  $\beta$  accounts for photo absorption, Compton scattering and other processes that attenuate the monochromatic beam. The real part of the refractive index is smaller than one because X-ray waves oscillate at frequencies higher than most resonance frequencies in atoms. Similar to a driven oscillator, the electrons then resonate out of phase

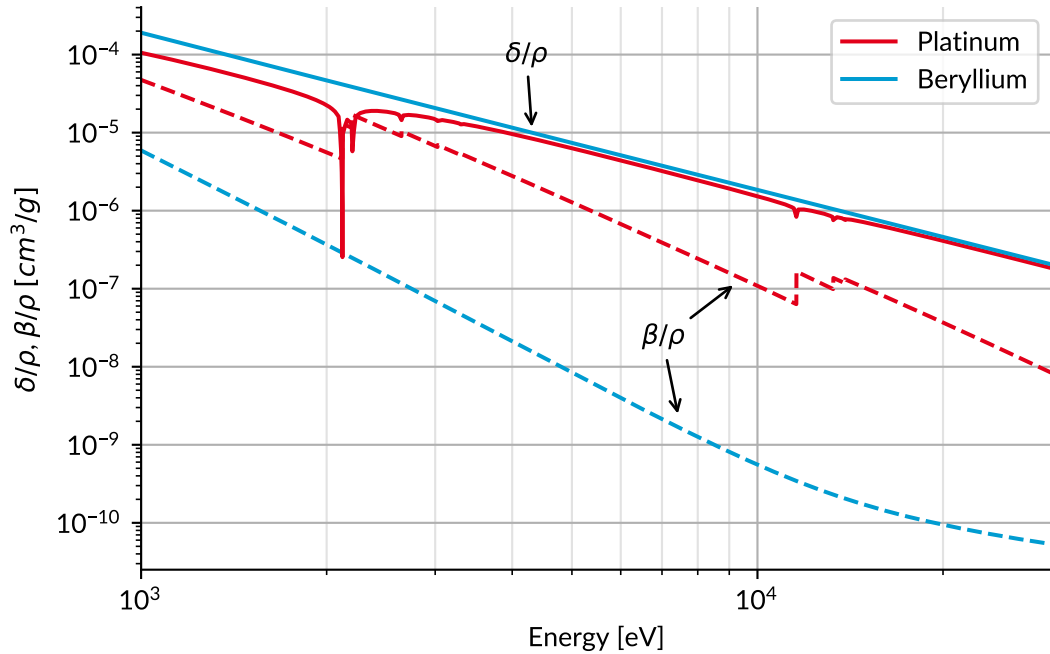


**Figure 2.4 Refractive index for platinum and beryllium.** The curves are divided by the density  $\rho$  to highlight that  $\delta$  follows a nearly universal curve for all elements. Deviations occur only at absorption edges, where  $\beta$  increases. The absorption is higher for elements with a higher atomic number  $Z$ .

with the wave. A refractive index smaller than one implies a phase velocity greater than the speed of light  $c$  in vacuum. This is no contradiction, as the relevant speed to transmit information is the group velocity, which is always smaller than  $c$ . The refractive index approaches one as the wavelengths become shorter, see Figure 2.4. This trend is only disrupted close to absorption edges and for very short wavelengths, where pair production and other new effects occur.

The wavelength of hard X-rays is in the Ångström range, the same length scale as atomic orbitals and inter-atomic distances. As the resolution in X-ray microscopy is currently above one nanometre, the atomic nature of all matter can be neglected and treated as a continuous. In crystals, the atoms have long-range order, which gives rise to Bragg peaks. For a perfect single crystal, more than 99% of the X-rays can be reflected [Shv+10]. However, the Bragg condition is highly anisotropic and only fulfilled for very narrow angles. The chances of randomly exciting a Bragg peak for a natural sample are negligible. For X-ray microscopy, the complex index of refraction is usually sufficient to describe the interaction between X-rays and the sample.

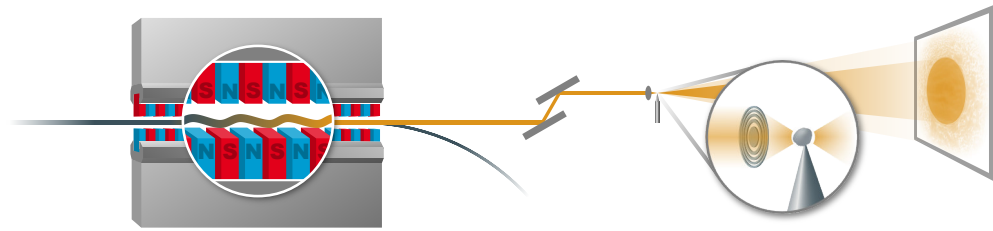


**Figure 2.5 Synchrotron diffraction experiment.** Strong magnets inside an undulator force ultra-relativistic electrons onto a slalom course. Due to this deflection, the electrons emit very bright X-rays. For the experiment, the X-rays are monochromatized and focused onto the sample. The resulting diffraction pattern is recorded with an imaging detector. Adapted from [DL18].

## 2.2 Synchrotron radiation

This section describes the generation of X-rays at synchrotron light sources and gives an outline of the P06 beamline at PETRA III where all experiments were performed.

### 2.2.1 Brightness

The brightness of a photon source is a measure of the coherent flux of the source. It can be used as a figure-of-merit to compare different sources, for example X-ray tubes to synchrotron light sources. For experiments using coherent photons, the difference in brightness translates directly into the exposure time that is required to reach a given signal-to-noise. The brightness  $\mathcal{B}$  is calculated as

$$\mathcal{B} = \frac{F}{\Omega \cdot A \cdot \Delta E/E}, \quad (2.25)$$

a ratio between the photon flux  $F$  and the source divergence  $\Omega$ , the source size  $A$  and the monochromaticity  $\Delta E/E$ . The brightness is typically given as  $[\mathcal{B}] = \text{ph/s/mrad}^2/\text{mm}^2/0.1\%$ . In these units, PETRA III can reach an average brightness above  $10^{20}$  for 8 keV photons. In comparison, an X-ray tube at this energy has a brightness of about  $10^{10}$ , a difference of ten orders of magnitude [Tho+09].

### 2.2.2 Synchrotron light sources

If electrons are forced onto a curved path by a static magnetic field, they emit synchrotron radiation. Synchrotron light sources use ultra-relativistic electrons to produce highly brilliant X-rays as synchrotron radiation. With typical energies around 5 GeV, these electrons have a Lorentz factor  $\gamma$  of 10 000 [AM11]. Due to this, the emitted radiation is shaped by relativistic effects. The two most prominent effects are the

Doppler shift and the relativistic addition of velocities. In the rest frame of the electrons, the electrons emit radio waves in all directions. Due to the Doppler effect, the radio waves are shifted to X-ray frequencies in the laboratory frame. A detailed theoretical description of synchrotron radiation can be found in Jackson [Jac99]. In general, the spectrum of synchrotron radiation is broad and covers a large part of the electromagnetic spectrum. With the transformation from the electron rest frame to the laboratory frame, the X-rays are collimated into a narrow cone around the instantaneous direction of the electrons. The opening angle of the cone is  $1/\gamma$ , around 0.1 mrad for synchrotron light sources. In comparison, an X-ray tube emits X-rays into a solid angle of  $4\pi$ .

At the centre of third-generation synchrotron light sources such as the ESRF or PETRA III is an electron storage ring that circulates electrons at relativistic speeds. Synchrotron light sources achieve the high brightness with wigglers and undulators, special installations that are dedicated purely to produce synchrotron radiation. These insertion devices contain a row of alternating magnets to increase the photon flux and can tune the wavelength of the emitted radiation by changing the distance between the magnets. Wigglers emit over a broad spectrum, whereas Undulators emit radiation concentrated at harmonics of a specific fundamental wavelength. The width of these undulator harmonics is a few hundred electronvolts. Each insertion device is part of a beamline for dedicated experiments, shown schematically in Figure 2.5. All experiments in this thesis were performed at the P06 beamline at PETRA III.

### 2.2.3 P06 Beamline

The P06 beamline is the hard X-ray micro-/nanoprobe beamline at PETRA III. The beamline is specialized for scanning applications by focusing X-rays onto a sub-micrometer spot and raster scan samples with different contrast techniques such as X-ray fluorescence, X-ray diffraction or X-ray beam induced current. P06 houses two experimental endstations called microprobe and nanoprobe. The microprobe is optimized for sub-micrometer resolutions and quick scanning of large samples. The nanoprobe is dedicated to resolutions below one hundred nanometer. To achieve this, it has an emphasis on high stability and low background signal. The focusing optics in the nanoprobe can achieve focal spot sizes of 40 nm.

Together with P05, P06 forms sector 4 of the Max-von-Laue-hall of PETRA III, see Figure 2.6. A detailed description of the layout and beamline components of P06 is given by Schroer *et al.* [Sch+16]. The components relevant for the experiments in this thesis are briefly described here.

The first components downstream of the source and directly before the optics hutch are high-power slits that define the beam aperture and reduce the heat-load on all following components. In the optics hutch, a monochromator allows to select an

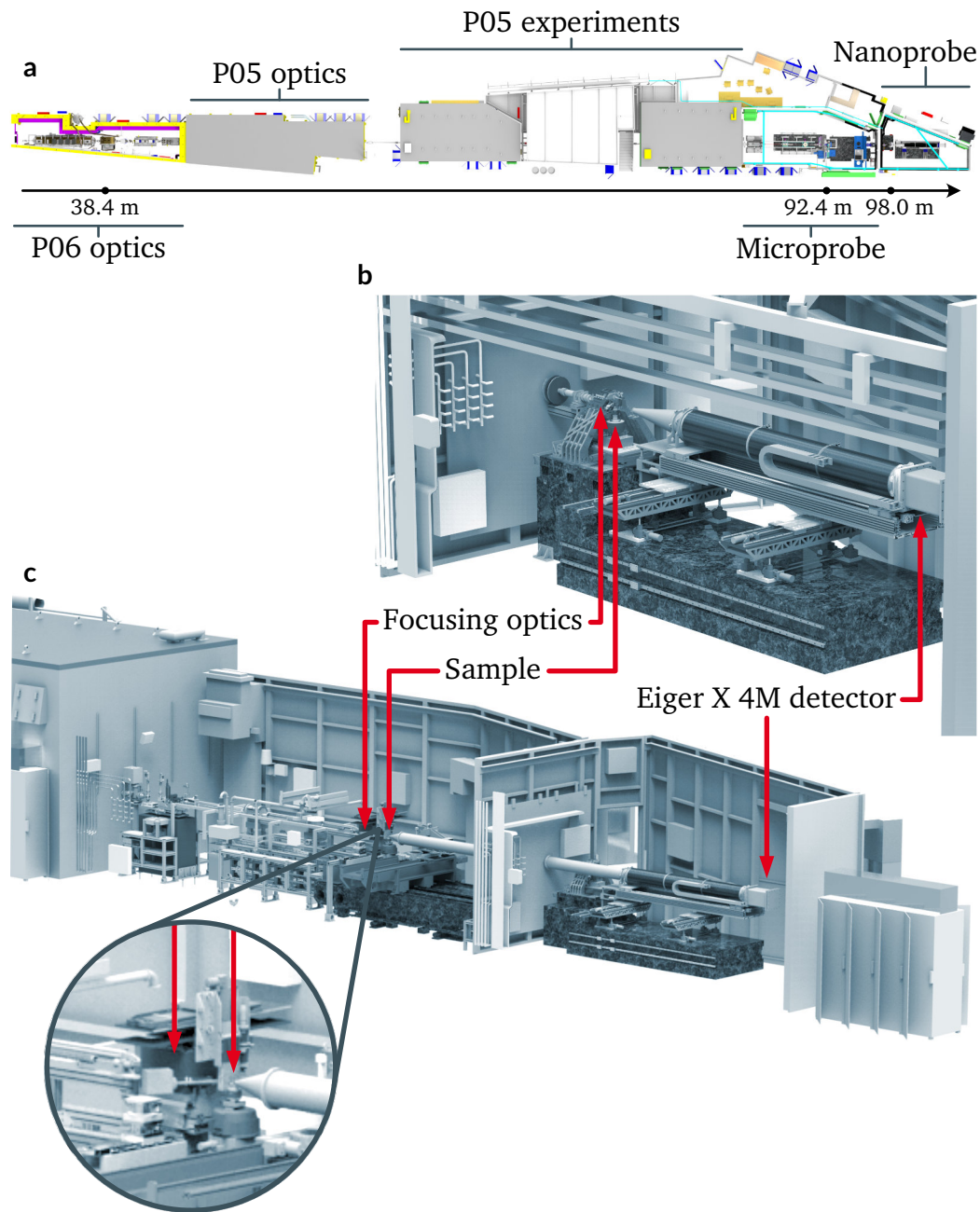


**Figure 2.6 P06 beamline layout.** **a** General layout of sector 4 which contains the two beamlines P05 and P06. The distances are measured from the center of the undulator. **b** The nanoprobe houses the Eiger detector inside an evacuated and movable flight tube. A thin diamond window allows X-rays to enter the flight tube and is, apart from a short air path, the only element between the sample and the detector panel. **c** For microprobe operation, the Eiger detector remains in the Nanohutch to maximise the distance between the sample and the detector. The scanning station in the Nanohutch can be moved to the side so that the flight tube can be extended through both hutch. Original images courtesy of R. Döhrmann.

energy band from the polychromatic spectrum that the undulator produces. The band has a relative width  $\Delta E/E$  of about  $10^{-4}$ . The monochromator contains a pair of silicon crystals in a vertical fixed-offset geometry and uses the (111) Bragg reflection. With Bragg reflections, it is difficult to filter the higher harmonics  $3E, 5E, \dots$  as these wavelengths also fulfil the Bragg-condition. To remove these higher energies, a pair of flat horizontally deflecting mirrors downstream of the monochromator acts as a low-pass filter that transmits only X-rays below a certain energy. The mirrors use total external reflection and have three different coatings made from silicon, chromium and platinum. For a reflection angle of 2.5 mrad, their respective cut-off energies are 12 keV, 20 keV and 30 keV.

The microprobe begins at 87 m from the source and contains the fast shutter that controls exposure times of 100 ms or longer. The main focusing optics are a pair of KB-mirrors with a focal length of 250 mm. Alternatively, other optics like CRLs can be used.

The nanoprobe aims for high-resolution imaging well below 100 nm. To achieve this, the experimental setup is designed with an emphasis on high stability. To this end, the scanning unit, which houses the focusing optics and the sample scanners, sits on a granite block and most structural elements are made from titanium and Invar, both materials that combine a high strength with a low thermal expansion. The nanoprobe uses laser interferometers to track the sample position with nanometer-precision [Sch+17]. Air scattering between the sample and the detector is another factor that limits the resolution [Rei+17]. To minimize the air path, the nanoprobe features an in-vacuum imaging detector inside an evacuated flight-tube [Sch+19a]. The vacuum chamber can house detectors up to an Eiger 4M (Dectris, [Joh+14]) in size.

## 2.3 X-ray optics

Wilhelm Röntgen already noted that normal glass lenses do not focus X-rays and he discovered that X-rays are not reflected by mirrors [Rön95]. In fact, special optics are required to focus X-rays for X-ray microscopy. A broad overview on various X-ray optics can be found in Schroer & Lengeler [SL12]. In this section, we describe three commonly used optics: Kirkpatrick-Baez-mirrors (KB-mirrors), Fresnel zone plates (FZPs) and compound refractive lenses (CRLs). These optics were used in the experiments in Section 4.4, Section 4.3 and Chapter 6, respectively.

### 2.3.1 KB-mirrors

X-rays show no regular reflection. Nevertheless, at very shallow angles they exhibit total reflection, similar to visible light. KB-mirrors use this total reflection to focus

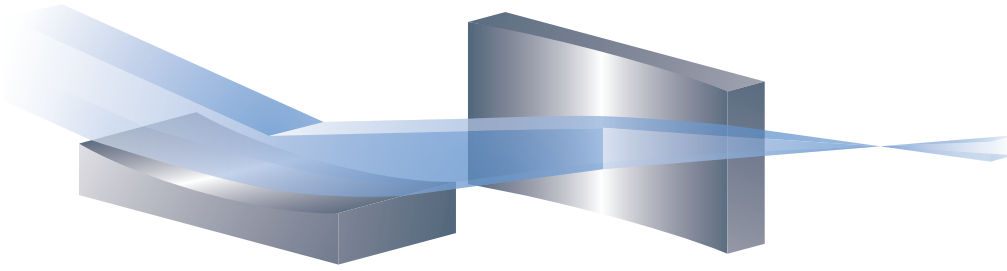


**Figure 2.7 Kirkpatrick-Baez-mirror set-up.** Each mirror focuses the beam in one direction. The upstream mirror focuses the beam vertically, the downstream mirror focuses it horizontally. For the beam to be focused into a spot, the two mirrors must be well aligned. Otherwise the beam will be astigmatic.

X-rays [KB48]. However, because the refractive index for X-rays is slightly smaller than one, X-rays exhibit total *external* reflection. This means that at the air-to-mirror interface, X-rays reflect away from the denser mirror material. The maximum numerical aperture of KB-mirrors is limited by the critical angle  $\alpha_c$ . The critical angle is determined by the refractive index decrement  $\delta$  of the surface material

$$\alpha_c = \sqrt{2\delta}. \quad (2.26)$$

Because  $\delta$  is on the order of  $10^{-6}$ ,  $\alpha_c$  is in the range of a few milliradians. To maximise the critical angle, KB-mirrors are often coated with heavy materials such as Gold or Platinum. For perfect focusing, the surface of the mirror must be smooth to a few Ångströms and should not deviate more than a few nanometer from the ideal shape. The ideal shape for a focusing X-ray mirror is an ellipsoid of revolution with one focal point of the ellipse at the X-ray source. This way, all X-rays are focused into the second focal point of the ellipse. Because it is easier to accurately polish a cylindrical surface instead of an ellipsoidal one, KB-mirrors employ two crossed cylindrical mirrors. The mirrors are curved like an elliptic cylinder, so that one mirror focuses the beam horizontally and one vertically. Figure 2.7 illustrates how such a two mirror system focuses the X-ray beam to a spot. It also shows how the KB-mirrors change the optical axis after the reflection. The big advantage of KB-mirrors compared to other X-ray optics is their achromaticity, which makes them ideal tools for spectroscopy.

### 2.3.2 Fresnel zone plates

Fresnel zone plates (FZPs) are diffraction gratings that are designed to diffract an X-ray beam so that part of the beam is focused to a spot [Kir74; SR69]. They consist

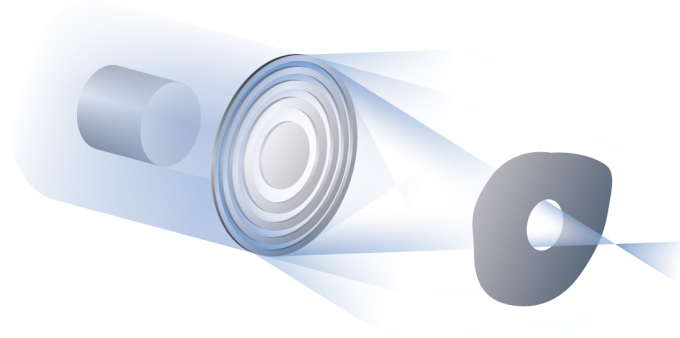


**Figure 2.8 Fresnel zone plate set-up.** The zone plate diffracts the beam into different focusing and defocusing orders. Shown here are the following orders: the first and third focusing order; the first defocusing order and the undiffracted zeroth order. All but the first focusing order are blocked by the central stop and the order-sorting aperture.

of concentric rings called zones, whose radii follow the formula

$$r_n = \sqrt{n\lambda f}, \quad (2.27)$$

with the wavelength  $\lambda$  and the focal length  $f$ . The zones alternate between filled and empty. The first zone from  $r_0$  to  $r_1$  is filled, the second zone from  $r_1$  to  $r_2$  is empty, the next is filled again and so on. The outermost filled zone, which is also the thinnest, determines the focal spot size.

Similar to a diffraction grating, FZPs also diffract into different orders. Each order is characterized by an integer number and has a unique focal length. Defocusing orders are designated by negative, focusing orders by positive numbers. The undiffracted beam is called the zeroth order. For a clean focus, all orders but one must be filtered out. This is achieved by a combination of two highly absorbing optical elements. The first is a central stop upstream of the FZP that blocks all radiation close to the optical axis. The second element is a pinhole, called order-sorting aperture (OSA). The OSA is placed downstream of the zone plate, close to the focal plane, and it blocks all orders except one. To fully block the direct beam, the diameter of the OSA must be smaller than the diameter of the central stop. Compared to KB-mirrors, FZPs are easier to produce, aberration-free and need less space for precise alignment motors.

### 2.3.3 Compound refractive lenses

For more than a century, X-ray lenses were thought impossible or impractical to make [KB48; Mic91; Rön95]. As the refractive index for all elements is very close to one, the focal length of a lens with constructable dimensions is on the order of hundreds of meters. However, Snigirev *et al.* realised that stacking many individual lenses

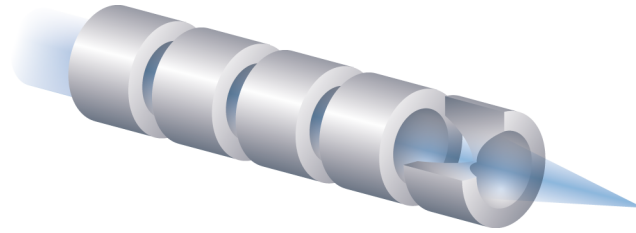


**Figure 2.9 Compound refractive lens set-up.** Concave lenses are used for focusing because the refractive index for X-rays is smaller than one. Depending on the X-ray energy, a lens stack contains typically 10 to 200 lenses.

shrinks the total focal length [Sni+96]. Because the refractive index for X-rays is smaller than one, X-rays are focused by concave lenses and defocused by convex lenses. For a thin lens, the ideal surface shape to focus a parallel beam into a point is a circular paraboloid. For visible light, the paraboloid can be approximated by spherical surfaces. Due to the strong curvatures of X-ray lenses, spherical lens shapes show strong aberrations for X-rays [Len+05]. The focal length of a thin stack of  $N$  double-curved lenses in vacuum is given by

$$f = \frac{R}{2N\delta}, \quad (2.28)$$

where  $R$  is the radius of curvature at the apex of the paraboloid and  $\delta$  is the refractive decrement of the lens material. Typical values for the curvature and the decrement are  $100 \mu\text{m}$  and  $10^{-6}$  respectively. The individual focal length of such a lens is  $50 \text{ m}$ , but a stack of one hundred lenses has a focal length of only  $0.5 \text{ m}$ . Effectively, stacking multiple lenses reduces the curvature.

Most commonly, X-ray lenses are produced in a coining process by pressing two opposing paraboloid stamps into a metal foil. The quality of the lenses depends on the shape fidelity of the stamps and their alignment onto a single axis. While the process is highly reproducible, the stacking of multiple lenses amplifies even small shape errors. Shape deviations as small as  $500 \text{ nm}$  per lens can already cause strong aberrations [Sei+17].

For short focal lengths and small focal spots, so-called nano-focusing lenses (NFLs) are produced using reactive ion-etching [Sch+03]. This approach is also used for refractive lamellar lenses [Sei+14] and adiabatically focusing lenses [Pat+17]. The latter offer the tightest focusing of all X-ray lenses with spot sizes below  $20 \text{ nm}$ . However, only two-dimensional features can be structured into the lens material with etching. Alternatively, additive manufacturing methods such as 3D printing can be employed to produce small lenses with small curvatures in arbitrary shapes. Section 6.2 describes this in more detail.

## 2.4 Phase problem

The phase problem describes the inability to directly measure the phase of X-ray waves. The electromagnetic field of X-rays oscillates faster than any detector can measure it, only the average amplitude of the field, the intensity, can be detected. This is an issue especially for X-ray crystallography, which measures the far-field scattering pattern  $I$  and aims to retrieve the original sample  $\psi$  [Tay03]. The scattering pattern is related to the sample through the Fourier transform

$$I = |\mathcal{F}(\psi)|^2, \quad (2.29)$$

and if the phases  $\varphi$  were known, it could be easily inverted

$$\psi = \mathcal{F}^{-1}(\sqrt{I} \cdot e^{i\varphi}), \quad (2.30)$$

to recover the sample. Without the phase information, however, the scattering pattern cannot be uniquely inverted, as many different objects produce the same scattering pattern. All that can be recovered is the autocorrelation

$$\mathcal{F}^{-1}(I) = \psi * \psi^*. \quad (2.31)$$

Phase retrieval techniques are algorithms that solve the phase problem. These algorithms recover the phases by using additional information about the sample to recover a unique solution [MKS00; OS08] or prepare the scattering in such a way that the auto-correlation can be resolved [McN+92].

In holography the phase problem is often called the twin-image problem. Due to the symmetry of the Fresnel propagation, the hologram reconstructs two solutions. Each solution is always overlaid with the defocused wave from the other solution. Suppressing or eliminating the twin image results in a unique solution and is equivalent to recovering the missing phase information.

## 3 Ptychography

Ptychography is a coherent imaging technique that solves the phase problem we described in Section 2.4 [Hop69]. Among imaging techniques, ptychography is unique in imaging the sample independent of the quality of the imaging optics. In ptychography, the sample is illuminated by a coherent beam that has a compact support. For the measurement, the sample is scanned across the beam in discrete steps. The beam is scattered by the sample and forms a diffraction pattern that is recorded with an imaging detector. This principle set-up is illustrated in Figure 3.1. For a successful reconstruction, it is necessary that the steps are small enough that the illuminated areas overlap between adjacent positions; the rule of thumb is to have 60 % overlap [MR09]. This ensures that parts of the sample are illuminated by two or more probe beams and that the resulting diffraction patterns share information. This shared information constrains the possible solutions and allows to robustly solve the phase problem.

Ptychography reconstructs both the complex transmission of the sample and the complex wavefield of the illuminating beam. Due to the separate reconstruction of the two, the reconstruction of the sample is not affected by the aberrations of the beam. Additionally, the resolution of the reconstruction is better than the beam size. An overview on X-ray ptychography can be found in Pfeiffer [Pfe18] and a comprehensive overview on ptychography in general can be found in Rodenburg & Maiden [RM19].

In this chapter, we shortly summarize the current state of ptychography, before introducing the novel refractive algorithm in the next chapter. We start by describing the commonly used ePIE algorithm for ptychography [MR09], using an approach similar to the maximum likelihood description from Thibault & Guizar-Sicairos [TG12]. Afterwards, we will outline three different improvements to ePIE, which reduce the noise in the reconstruction, increase the resolution of the diffraction patterns or improve the convergence speed of the algorithm. Finally, the last section will give details about implementing ptychography in practice.

### 3.1 Classic ptychography

In ptychography, the approach for the reconstruction is to model the diffraction patterns and refine the model until the simulated diffraction patterns match the measured patterns. It is an iterative process that improves the estimate with each

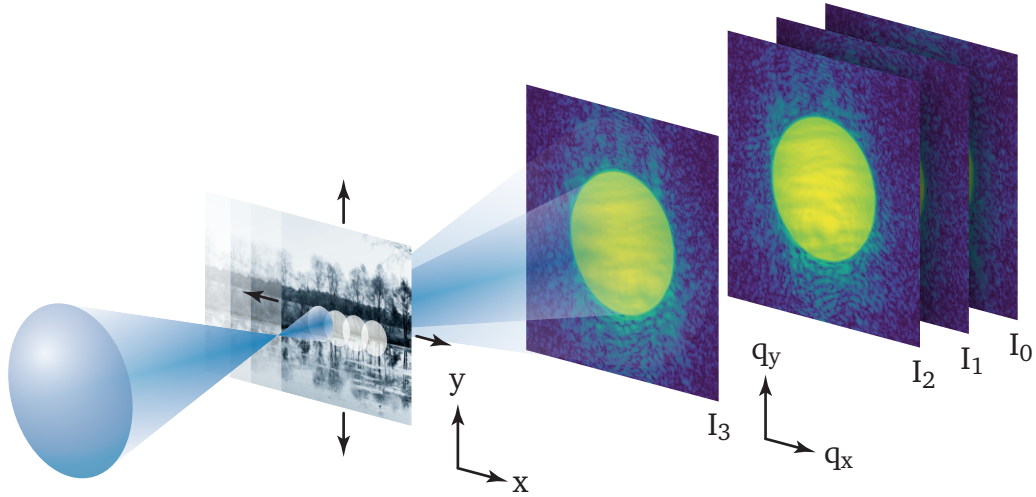


**Figure 3.1** Experimental set-up for ptychography. The incoming beam is focused and the sample is placed near the focal plane. For the scan, the sample is moved transversally to the propagation direction. The scattered light for each scan position is recorded by an image detector.

iteration. The reconstruction is deemed finished if the changes between subsequent iterations are small enough. There are many different variants of this basic scheme, a commonly used one is the extended ptychographical iterative engine (ePIE) algorithm by Maiden & Rodenburg [MR09]. This section gives a derivation of this algorithm, using the minimization approach of Thibault & Guizar-Sicairos [TG12].

For classic ptychography, the illuminating beam is modelled as a two-dimensional, complex-valued field  $P$  called probe. The wave is defined in a plane transversal to the propagation direction. The interaction of the probe with the sample is modelled as an element-wise multiplication with the object transmission function  $O$ , another two-dimensional, complex-valued field. This is a good description for thin samples, that show no multi-scattering effects and where the propagation of the probe inside the sample volume can be neglected. A detailed evaluation of this assumption can be found in the supporting material to Thibault *et al.* [Thi+08]. Under this thin sample assumption, the scattered wavefield  $\psi$  is modelled as

$$\psi_{\mathbf{r}} = O_{\mathbf{r}} \cdot P_{\mathbf{r}}, \quad (3.1)$$

where  $\mathbf{r} = (x, y)$  describes the discrete coordinates in the field. In a ptychography scan, the probe is moved across the object

$$\psi_{j,\mathbf{r}} = O_{\mathbf{r}} \cdot P_{\mathbf{r}-\mathbf{R}_j} \quad (3.2)$$

in step positions  $\mathbf{R}_j$  that ensure sufficient coverage of the sample. For each position,

the far-field of the wavefield is recorded with the detector. The propagation to the detector, situated in the Fraunhofer regime, can be described with a Fourier transform

$$\Psi_{\mathbf{q}} = \mathcal{F}(\psi) = \frac{1}{\sqrt{N}} \sum_{\mathbf{r}} \psi_{\mathbf{r}} \cdot e^{i\mathbf{q}\mathbf{r}}, \quad (3.3)$$

where  $N$  is the number of elements in the field, as described in Section 2.1.1. As we outlined for the phase problem in Section 2.4, the detectors for visible light and for X-rays can only record the intensity of the wavefield. We therefore square the modulus of the modelled wavefield

$$I_{\mathbf{q}} = |\Psi_{\mathbf{q}}|^2. \quad (3.4)$$

To reconstruct object and probe, we compare the modelled intensities to the measurements using a quadratic error function

$$L = \sum_j \sum_{\mathbf{q}} \left( \sqrt{I_{j,\mathbf{q}}} - \sqrt{n_{j,\mathbf{q}}} \right)^2. \quad (3.5)$$

This error function quantifies how well the modelled diffraction patterns  $I_j$  match the measured diffraction patterns  $n_j$ . In the absence of vibrations and detector noise, the  $n_j$  will be Poisson distributed. Calculating the square root equalizes the shot noise so that bright and dark pixels influence  $L$  equally. A detailed description of various noise models and their influence on the reconstruction can be found in Godard *et al.* [God+12]. The object and probe with the minimum error solve the phase problem owing to the redundancy of the data. Typical sizes for the object and probe are in the megapixel range, reconstructed from gigapixels of diffraction data. To find the minimum error, we calculate the gradient by differentiating  $L$  with respect to the object and probe, using Wirtinger derivatives. Appendix A.1 defines Wirtinger derivatives and gives an overview of some important properties. We start with the gradient with respect to the object

$$\frac{\partial L}{\partial O_{\mathbf{r}}} = \sum_j \sum_{\mathbf{q}} \frac{\partial \left( \sqrt{I_{j,\mathbf{q}}} - \sqrt{n_{j,\mathbf{q}}} \right)^2}{\partial I_{j,\mathbf{q}}} \cdot \frac{\partial I_{j,\mathbf{q}}}{\partial O_{\mathbf{r}}}. \quad (3.6)$$

Because object and probe are symmetric in the multiplication in Equation 3.1, the probe gradient follows similarly. We can calculate the first factor, containing the squared difference, straightforward

$$\frac{\partial \left( \sqrt{I_{j,\mathbf{q}}} - \sqrt{n_{j,\mathbf{q}}} \right)^2}{\partial I_{j,\mathbf{q}}} = \left( 1 - \frac{\sqrt{n_{j,\mathbf{q}}}}{\sqrt{I_{j,\mathbf{q}}}} \right). \quad (3.7)$$

For the second factor in Equation 3.6, the derivative of the intensity, we use the definition of the Fourier transform to commute the sum and the derivative

$$\frac{\partial I_{j,\mathbf{q}}}{\partial O_{\mathbf{r}}} = \Psi_{j,\mathbf{q}}^* \cdot \frac{\partial \Psi_{j,\mathbf{q}}}{\partial O_{\mathbf{r}}} = \frac{\Psi_{j,\mathbf{q}}^*}{\sqrt{N}} \cdot \sum_{\mathbf{r}'} e^{i\mathbf{q}\mathbf{r}'} \cdot P_{\mathbf{r}'-\mathbf{R}_j} \frac{\partial}{\partial O_{\mathbf{r}}} O_{\mathbf{r}'}. \quad (3.8)$$

The product rule is not applied here due to our use of Wirtinger derivatives (see Appendix A.1). Multiplying the two factors in Equation 3.6 and changing the summation order results in a Fourier transform of the conjugated far-field

$$\frac{\partial L}{\partial O_{\mathbf{r}}} = \sum_j \sum_{\mathbf{q}} \frac{P_{\mathbf{r}-\mathbf{R}_j}}{\sqrt{N}} \cdot \left( 1 - \frac{\sqrt{n_{j,\mathbf{q}}}}{\sqrt{I_{j,\mathbf{q}}}} \right) \Psi_{j,\mathbf{q}}^* \cdot e^{i\mathbf{q}\mathbf{r}}. \quad (3.9)$$

We abbreviate the product of the parantheses and the wavefield as

$$\Phi_{j,\mathbf{q}} := \left( 1 - \frac{\sqrt{n_{j,\mathbf{q}}}}{\sqrt{I_{j,\mathbf{q}}}} \right) \Psi_{j,\mathbf{q}} \quad (3.10)$$

to clear up the equation. Since the difference is real, it is identical to its complex conjugate. The gradient is now

$$\frac{\partial L}{\partial O_{\mathbf{r}}} = \sum_j \frac{P_{\mathbf{r}-\mathbf{R}_j}}{\sqrt{N}} \cdot \sum_{\mathbf{q}} \Phi_{j,\mathbf{q}}^* \cdot e^{i\mathbf{q}\mathbf{r}}. \quad (3.11)$$

The sum over  $\mathbf{q}$  is a Fourier transform

$$\frac{\partial L}{\partial O_{\mathbf{r}}} = \sum_j P_{\mathbf{r}-\mathbf{R}_j} \mathcal{F}(\Phi_j^*)_{\mathbf{r}}, \quad (3.12)$$

and we can replace  $\Phi_j$  with its inverse Fourier transform  $\phi_j = \mathcal{F}^{-1}(\Phi_j)$ , to get

$$\frac{\partial L}{\partial O_{\mathbf{r}}} = \sum_j P_{\mathbf{r}-\mathbf{R}_j} \mathcal{F}([\mathcal{F}(\phi_j)]^*)_{\mathbf{r}}. \quad (3.13)$$

Conjugating the inner Fourier transform converts it into an inverse transform, which counteracts the outer transform. In the end only  $\phi_j$  remains, yielding

$$\frac{\partial L}{\partial O_{\mathbf{r}}} = \sum_j P_{\mathbf{r}-\mathbf{R}_j} \cdot \phi_{j,\mathbf{r}}^*. \quad (3.14)$$

The gradient for the probe is similar, using the symmetry between  $O$  and  $P$  in the

multiplication, we get

$$\frac{\partial L}{\partial P_{\mathbf{r}}} = \sum_j O_{\mathbf{r}+\mathbf{R}_j} \cdot \phi_{j,\mathbf{r}+\mathbf{R}_j}^* \quad (3.15)$$

Ideally, we would set the two gradients to zero and solve for the corresponding object and probe. This is difficult because the two equations are coupled and non-linear. As no closed-form solution exists, we must depend on iterative methods. One of the simplest iterative methods is line search, which searches for the minimum along the direction given by the gradient, reducing the complexity to a one dimensional search. At the minimum of the line, the next iteration starts by calculating the new gradient and then searches along this new direction. However, line search requires many evaluations of the error function in each iteration before the line minimum is found. In the case of ptychography this is slow, as each evaluation runs a loop over all diffraction patterns.

In place of line search, we use gradient descent. In each iteration of gradient descent, we calculate the gradient and take one step proportional to the negative of the gradient. The ePIE algorithm uses stochastic gradient descent, which splits the gradient calculation and gradient step further into subiterations. For ptychography, the natural choice for the subiterations are the individual diffraction patterns. Instead of taking the gradient step only after we calculated the full gradient, we randomly select a diffraction pattern and calculate the gradient only for this pattern. Then, we take the gradient step for this diffraction pattern. In the next subiteration, we randomly select a new diffraction pattern that was not used in the previous subiterations, calculate the new gradient and take a step in this new direction. One iteration is complete once we have used each diffraction pattern once. Due to the large redundancy in the dataset, this stochastic approach converges quicker than always calculating the full gradient.

In each subiteration  $l$ , we randomly choose a diffraction pattern  $n_j$  that has not yet been used in this iteration, calculate the gradient just for this pattern and add the negative of the respective gradient to object and probe

$$O_{l+1,\mathbf{r}} = O_{l,\mathbf{r}} + \alpha \frac{-\phi_{j,\mathbf{r}}}{\max |P_{l,\mathbf{r}-\mathbf{R}_j}|^2} \cdot P_{l,\mathbf{r}-\mathbf{R}_j}^* \quad (3.16a)$$

$$P_{l+1,\mathbf{r}} = P_{l,\mathbf{r}} + \beta \frac{-\phi_{j,\mathbf{r}+\mathbf{R}_j}}{\max |O_{l,\mathbf{r}+\mathbf{R}_j}|^2} \cdot O_{l,\mathbf{r}+\mathbf{R}_j}^* \quad (3.16b)$$

The factors  $\alpha$  and  $\beta$  adjust the update strength. The division by the maximum of the squared modulus ensures that the update remains stable and it scales the object and probe update to the same order of magnitude. The modulus of the object is typically between zero and one, while the probe modulus is fixed by the beam intensity during the experiment. The conjugation switches from  $\phi$  to  $O$  and  $P$  due to the definition of the Wirtinger derivatives, which are defined for complex numbers  $z = x + iy$

as  $\partial/\partial z = \partial/\partial x - i\partial/\partial y$ . After every diffraction pattern has been used once, one iteration is complete. Typically, the reconstruction is converged after 100 to 1000 iterations.

## 3.2 Parallel ptychography

The previously described ePIE algorithm is a robust ptychography algorithm for a broad range of situations. However, ePIE has difficulties to fully converge to the optimal solution. Iterative ptychography algorithms, such as ePIE, use two nested loops for the reconstruction. The outer loop repeats the iterations, while the inner loop runs in subiterations over all diffraction patterns to calculate their update contribution. In ePIE, the object and probe are updated after every subiteration, which is similar to a local optimization for the current diffraction pattern. As the patterns contain noise, the local optimum of each pattern is in general different from the global optimum. As the order in which the patterns are used in the inner loop is reshuffled in each iteration, the object and probe never converge completely but jitter around the optimal solution. To circumvent this, the update strengths  $\alpha$  and  $\beta$  could be dynamically weakened with each iteration. Alternatively, the update from each diffraction pattern can also be applied in parallel, not sequentially. Then object and probe are only updated once per iteration after the inner loop is finished, removing all effects from the update order.

A second problem of ePIE is the slow reconstruction of certain sample regions. These are those areas of the sample that were only weakly illuminated during the scan by the dimmer parts of the probe. Due to the division in the object update by the maximum of the probe intensity, the update in these areas becomes small. Compared to brightly illuminated regions, it often takes a hundred times more iterations to reconstruct these regions. In this section, we address both drawbacks with a parallel, locally scaled ptychography algorithm. This parallel ptychography variant is also called the error reduction approach to ptychography [God+12; Yan+11].

To derive parallel ptychography, we go back to the full gradients from Equations 3.14 and 3.15. As they average the changes from all patterns, the first drawback of ePIE is eliminated. To correct the slow convergence of darkly illuminated sample parts, we change the division by the maximum to a division by the summed modulus:

$$O_{l+1,\mathbf{r}} = O_{l,\mathbf{r}} + \alpha \frac{-\sum_j \phi_{j,\mathbf{r}} \cdot P_{l,\mathbf{r}-\mathbf{R}_j}^*}{\sum_j |P_{l,\mathbf{r}-\mathbf{R}_j}|^2 + \delta} \quad (3.17a)$$

$$P_{l+1,\mathbf{r}} = P_{l,\mathbf{r}} + \beta \frac{-\sum_j \phi_{j,\mathbf{r}+\mathbf{R}_j} \cdot O_{l,\mathbf{r}+\mathbf{R}_j}^*}{\sum_j |O_{l,\mathbf{r}+\mathbf{R}_j}|^2 + \delta}. \quad (3.17b)$$

These are the parallel updates for object and probe. To avoid division by zero, a small  $\delta$  is added in the denominator, in the order of  $10^{-3}$ . In the case of the object update, we can assign a physical meaning to the sum in the denominator, it is the total illumination of the sample during the scan, the radiant exposure.

With the parallel ptychography algorithm, we can avoid the drawbacks of ePIE. Due to the sum over all positions and patterns the order is irrelevant and weakly illuminated sample areas converge faster as a result of the locally adapted denominator. However, parallel ptychography has a tendency to stagnate, which is desired if object and probe are nearly optimal, but problematic if they are far from convergence and have only few similarities with the optimal solution. Furthermore, the weakly illuminated parts of the sample are reconstructed faster than with ePIE, but the noise in the reconstruction is considerably higher. This is more a consequence of the measurement than the algorithm, nevertheless ePIE limits the noise in the reconstruction over the whole reconstructed sample area.

In practice, it is best to start with ePIE and switch to parallel ptychography when the reconstruction has nearly converged. This way, the robustness and speed of ePIE are coupled with the smoothness of parallel ptychography. In addition, the sample areas with the lowest noise are reconstructed first with high confidence and the more uncertain areas only after the algorithms have been switched. Each scan is different in how many iterations should be used for each algorithm. Nevertheless, running both algorithms for the same number of iterations is in general sufficient.

### 3.3 Upsampling ptychography

In ptychography, the diffraction patterns must be sufficiently sampled to truthfully reconstruct the sample. Whether a diffraction pattern is sufficiently sampled or not can be determined with the Nyquist-Shannon sampling theorem [Sha49]. According to this theorem, a band-limited signal is sufficiently sampled if the sampling frequency is more than twice the highest signal frequency. In the context of X-ray ptychography, a diffraction pattern is band-limited if the probe in the sample plane has a finite support  $D$ . The sampling frequency is given by the size  $p$  of the detector pixels. As the detector is situated in the far-field of the sample, the pixel size defines a field of view  $S_0$  in the sample plane. In paraxial approximation, the field of view is given by

$$S_0 = \frac{\lambda d}{p}, \quad (3.18)$$

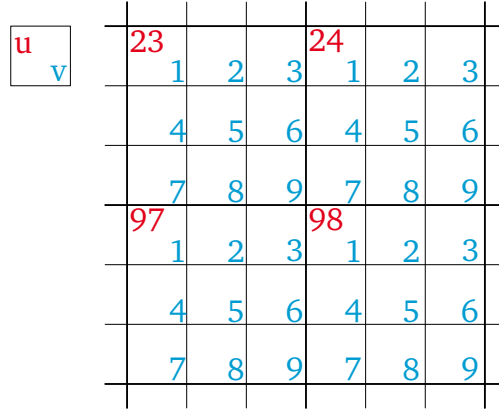


**Figure 3.2 Upsampling scheme.** Illustration of the detector pixel coordinates for an upsampling of  $s = 3$ . The detector pixels are each labelled with a unique and continuous number. Every detector pixel  $u$  is divided into  $s^2 = 9$  virtual subpixels  $v$ .

for a detector distance  $d$  and wavelength  $\lambda$ . Thus, the patterns are sufficiently sampled if the field of view  $S_0$  is more than double the size of the support  $D$ :

$$2D < S_0. \quad (3.19)$$

If Equation 3.19 is violated and the diffraction patterns are undersampled, artefacts appear in the reconstruction. For these cases the sampling ptychographical iterative engine (sPIE) has been developed [Bat+14]. sPIE allows to relax the sampling criterion by exploiting the redundancy in ptychographic measurements. It is based on the idea of virtually upsampling the diffraction patterns by a factor  $s$ . With upsampling, the reconstruction algorithm assumes a virtual detector with smaller subpixels  $p/s$  to fulfil the sampling criterion. The reconstruction is similar to ePIE, except for the far-field update, as there is a discrepancy between the number of pixels in the measured diffraction pattern and in the simulated wavefield. Figure 3.2 illustrates how the real detector pixels and the virtual subpixels are related. For each detector pixel  $u$ , the wavefield contains  $s \cdot s$  virtual subpixels  $v$ . Equation 3.10 is therefore updated so that the sum of the virtual subpixels in a given detector pixel is consistent with the measured intensity  $n_{j,u}$  in the real pixel, yielding

$$\Phi_{j,u,v} := \left( 1 - \frac{\sqrt{n_{j,u}}}{\sqrt{\sum_{v=1}^{s^2} |\Psi|_{j,u,v}^2}} \right) \Psi_{j,u,v}. \quad (3.20)$$

Here,  $u$  addresses the pixel coordinates of the real pixels,  $v$  addresses the coordinates of the virtual subpixels,  $m$  is the index of the diffraction pattern,  $n$  represents the measured intensity of the detector pixel,  $\Psi$  represents the upsampled wavefield and

$\Phi$  represents the far-field update. Because it is difficult to express the sum in the denominator of Equation 3.20 in terms of the  $\mathbf{q}$ -coordinates, the indexing is changed for this equation.

### 3.4 Momentum accelerated Ptychography

How many iterations a Ptychography reconstruction needs until it is converged, depends heavily on the initial object and probe. The accuracy of the probe estimate is the primary factor that determines how the reconstruction will converge or if at all. Most often, a good guess of the probe can be made based on the knowledge of the focusing optics and the experimental geometry. Having said that, optics can potentially suffer from unknown aberrations, making an educated guess of the probe difficult. Likewise, a diffuser of unknown structure might be used in the experiment to increase the scattering to large angles. In both situations, it can be difficult to make an accurate prediction of the probe, leading to slow reconstructions. The object estimate is less important, but still influences the final result. For most Ptychography experiments with visible light or X-rays, the empty, transparent object is an appropriate starting point. This is not the case for strongly scattering objects. If the starting probe or object are unsuitable, the reconstruction may take several thousand iterations before it converges.

In this section, we describe Nesterov accelerated gradients (NAGs) for Ptychography. The description follows the work from Maiden *et al.* [MJL17], who were the first to demonstrate that Ptychography can benefit from momentum acceleration. Adding NAG makes Ptychography algorithms more robust and accelerates the reconstruction under difficult conditions. Detailed overviews on NAG and similar momentum accelerations were written by Ruder [Rud17] and Goh [Goh17].

The Ptychography algorithms in this thesis are all error reduction algorithms. Error reduction can be pictured as a hilly landscape over all possible parameters, where the height at each point is defined by the error value  $L$  for this set of parameter values  $\theta$ . Minimizing the error means finding the lowest point among the hills. Gradient descent can be pictured as a short sighted cow in this landscape. The cow can only see slightly beyond its feet. To find the lowest point, it walks downhill in the steepest direction. The cow descends step-by-step, going from the current parameter set  $\theta_l$  to  $\theta_{l+1}$ , then  $\theta_{l+2}$  and so on, each time lowering the error until the cow finds a minimum where the landscape goes uphill in every direction. Unfortunately, it is in general hard to find out if this is the global or a local minimum. Formally, we express the downhill stepping of gradient descent as

$$\theta_{l+1} = \theta_l - \alpha \nabla L(\theta_l). \quad (3.21)$$

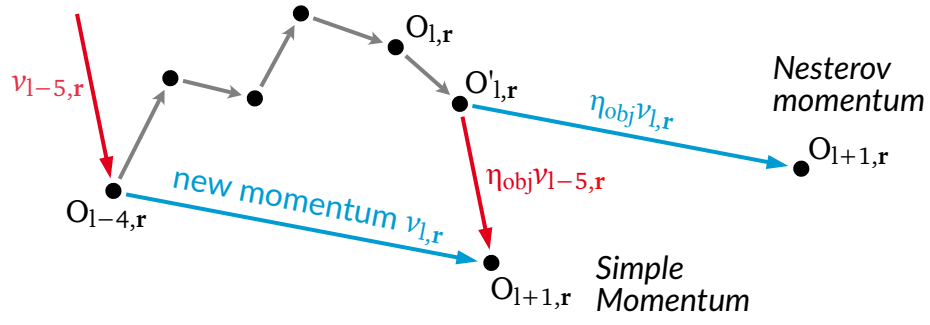


**Figure 3.3 Comparison between Nesterov' and simple momentum for ptychography.** This illustrates how a single object pixel evolves in the complex plane. It highlights the difference how Nesterov momentum is applied in comparison to simple momentum. The momentum is here added every  $T = 5$  subiterations. Adapted from [MJL17].

Momentum in contrast can be imagined as a cannonball that is rolling down the hill. As it rolls down, it gains speed, becoming faster and faster. If the surface is smooth enough, it will continue accelerating. When it reaches the bottom of a valley, it does not stop but keeps on climbing uphill on the opposite side, losing speed. Due to this, the cannonball can escape local minima. The name *momentum* is derived from the inertia of this physical analogy. In each iteration, the momentum  $v$  is updated and the updated momentum is then applied to the current parameters

$$v_{l+1} = \eta v_l - \alpha \nabla L(\theta_l), \quad (3.22)$$

$$\theta_{l+1} = \theta_l + v_{l+1}. \quad (3.23)$$

The momentum damping factor  $\eta$  acts as friction on the cannonball and is between zero and one. The closer it is to one, the more speed the ball can pick up. Typically,  $\eta$  is set to 0.9. Nesterov accelerated gradient (NAG) improves this simple momentum by doing both, a momentum and a gradient step. First, the gradient is added to the momentum like before. Afterwards, the momentum and the gradient are added to the current parameters

$$v_{l+1} = \eta v_l - \alpha \nabla L(\theta_l), \quad (3.24)$$

$$\theta_{l+1} = \theta_l + \eta v_{l+1} - \alpha \nabla L(\theta_l). \quad (3.25)$$

Nesterov accelerated gradient (NAG) updates both the gradient and the current parameters with the local gradient. If this leads to oscillating behaviour, it can be stabilized by reducing the step size  $\alpha$  of the gradient. This does not necessarily slow down the reconstruction because the momentum can increase the convergence.

We incorporate NAG into ptychography by introducing two new complex-valued fields  $v_r$  and  $u_r$  for the object and probe momentum respectively. In addition, we add

the two corresponding momentum damping factors  $\eta_{\text{obj}}$  and  $\eta_{\text{prb}}$ . The gradient in ePIE is fluctuating, changing strongly for each subiteration. For a smoother estimate, we calculate the average gradient over multiple subiterations. We introduce a new parameter  $T$ , that determines how many subiterations are calculated before the momentum is added again. Figure 3.3 shows an example for  $T = 5$ . The ePIE update is slightly changed

$$O'_{l,\mathbf{r}} = O_{l,\mathbf{r}} + \alpha \frac{-\phi_{j,\mathbf{r}}}{\max |P_{l,\mathbf{r}-\mathbf{R}_j}|^2} \cdot P_{l,\mathbf{r}-\mathbf{R}_j}^*, \quad (3.26)$$

as a subiteration finishes now after the momentum step. The momentum step consists of a check if  $T$  subiterations have passed since the last momentum update. If not, then the subiteration is finished and continues with the next diffraction pattern. If the check is positive, then we update the momentum

$$v_{l,\mathbf{r}} = \eta_{\text{obj}} v_{l-T,\mathbf{r}} + (O'_{l,\mathbf{r}} - O_{l+1-T,\mathbf{r}}) \quad (3.27)$$

by adding the changes since the last momentum step. The new momentum is then added to the object

$$O_{l+1,\mathbf{r}} = O'_{l,\mathbf{r}} + \eta_{\text{obj}} v_{l,\mathbf{r}}, \quad (3.28)$$

finishing the subiteration and resetting the counter for the next momentum step. Figure 3.3 illustrates this procedure. For four iterations, the object is updated normally. In the fifth iteration, after the ePIE update is applied, the momentum is updated and then added to the object. This also shows the difference between simple momentum and NAG because the first would add the old momentum instead of the new one.

For the reconstructions, it is best to set the object update  $\alpha$  between 0.1 and 0.2 and keep the probe update  $\beta$  at one. The momentum step should be added after 10 % to 50 % of the diffraction patterns have been used, depending on the overlap. Every object pixel should on average be updated at least once between two momentum steps. If there is less overlap between adjacent scan positions, then the momentum steps should be more scarce. The momentum damping factors  $\eta_{\text{obj}}$  and  $\eta_{\text{prb}}$  can both be set to 0.9. For parallel ptychography the procedure is the same, but it allows for more frequent momentum updates as the reconstruction is more stable.

## 3.5 Practical ptychography implementation

### 3.5.1 Resolution and field of view in ptychography

The Abbe criterion for the resolution in classical light microscopy is given by

$$\Delta x = \frac{\lambda}{2NA}, \quad (3.29)$$

half the wavelength of the light divided by the numerical aperture of the focusing lens. In ptychography on the other hand, the resolution is not determined by the focusing element. Instead, the detector acts as a virtual lens and the resolution is given by the largest detectable scattering angle. For a  $N \times N$  pixel detector with a pixel size  $p$  that is placed a distance  $d$  from the sample, the resolution in ptychography is

$$\Delta x = \frac{\lambda}{2 \sin [\arctan (Np/2d)]}. \quad (3.30)$$

In many situations, the largest detectable scattering angle is small and we can use the small angle approximation and set the sine and tangent equal. With this, we get

$$\Delta x \approx \frac{\lambda d}{Np}. \quad (3.31)$$

For a successful ptychography reconstruction, the diffraction patterns must be correctly resolved. The diffraction patterns are sufficiently sampled if the Nyquist condition is fulfilled. This is the case if the probe is small enough, as the size of the probe and the size of the speckle are inversely proportional.

### 3.5.2 Position refinement

High-resolution ptychography requires precise knowledge of the scan positions. In experiments, the scanning stages always have a limited precision and the sample can drift during the scan. Consequently, the position values are inaccurate, which limits the resolution in the reconstruction and gives rise to artefacts. The precision can be improved with laser interferometers, however these can only track a reference mirror close by the sample [Hol+12; Sch+17]. As a result, the interferometers are blind to relative movements between the sample and the reference mirror. Compared to the other positioning errors, the relative movements are small, but they still limit the achievable resolution.

Various algorithms have been developed to algorithmically correct faulty position values [Mai+12; Zha+13]. Schropp *et al.* [Sch+13] conceived a brute-force approach to search for the best fitting sample positions. Their approach optimizes the position

of each diffraction pattern individually by minimizing the error from Equation A.13 between the simulated and the measured diffraction pattern. The optimisation calculates the error for all positions in a box around the current position and chooses the one with the lowest error. To minimize the slow down of the reconstruction, the search is only run every 10 to 50 iterations.

### 3.5.3 Software

All ptychography reconstructions in this thesis were computed with the software *ptycho*. This program is written in CUDA C/C++ and uses the GPU for fast computations. Graphics cards are ideally suited, as ptychography requires many pointwise matrix operations which can be efficiently implemented on the parallel streaming processors of the GPU.

*ptycho* was started by Wolfgang Hönig as a test to compare the performance of ptychography on a CPU and a GPU [Hön10]. This test program was expanded by Robert Hoppe during his PhD studies to include more features and become an effective tool for experiments. He gives a detailed description about the design and inner workings of *ptycho* in his PhD thesis [Hop19]. After Robert Hoppe finished his studies, Felix Wittwer became the main developer and added more features, for example the momentum from Section 3.4 or the refractive ptychography in Chapter 4.



## 4 Refractive Ptychography

Most phase retrieval techniques such as ptychography, coherent X-ray diffraction imaging (CXDI) or inline holography reconstruct only the complex-valued transmission function of the sample. However, the transmission function is not linearly dependent on the object thickness or the object density and the phase shift is potentially ambiguous. In tomography, the most commonly used algorithms work on a linear model and the transmission must be transformed into linear projections before they can be reconstructed tomographically. In X-ray phase tomography, especially when combined with ptychography [Gui+11; Kah+19], both the non-linearity and the ambiguity of the phase are a problem, as a phase shift  $h$  cannot be distinguished from a shift  $h + 2\pi$  since the phase shift is  $2\pi$ -periodic.

These problems could be avoided, if ptychography would directly reconstruct the projection of the complex refractive index, as the refractive index is unambiguous and proportional to the object thickness. In Section 4.1 we develop a novel and original ptychography algorithm that directly reconstructs the real and imaginary part of the projected complex refractive index. In Section 4.2 we test this new algorithm on a simulated experiment to compare the reconstruction results to a ground truth. We demonstrate the algorithm in Section 4.3 and Section 4.4 on two experimental datasets with a weakly and strongly phase shifting sample, respectively.

### 4.1 Basics

We will start similar to Section 3.1 with the basic ptychographic model. In contrast to the conventional model, our refractive object will be in the exponent. To differentiate the two, we will call this new object  $\tilde{O}_{\mathbf{r}}$  and it is related to  $O_{\mathbf{r}}$  by

$$O_{\mathbf{r}} = e^{i\tilde{O}_{\mathbf{r}}}. \quad (4.1)$$

To avoid confusion, we will use the following nomenclature:  $O$  will remain the object and  $\tilde{O}$  will be called the refractive object. We call  $\arg(O) = \Re(\tilde{O})$  the *phase* or *phase shift* of the object,  $|O| = e^{-\Im(\tilde{O})}$  the *modulus* of the object and  $\Im(\tilde{O})$  the *projected absorption index*. We will derive the refractive object and probe updates for  $\tilde{O}_{\mathbf{r}}$  again

via the maximum likelihood. The wavefield is now

$$\psi_{\mathbf{r}} = e^{i\tilde{O}_{\mathbf{r}}} \cdot P_{\mathbf{r}} \quad (4.2)$$

and most of the calculations for  $L$  and  $\partial L/\partial I$  remain the same as in Section 3.1. The first difference occurs in Equation 3.8, where formerly the object dependence

$$\frac{\partial}{\partial O_{\mathbf{r}}} O_{\mathbf{r}} P_{\mathbf{r}-\mathbf{R}_j} = 1 \cdot P_{\mathbf{r}-\mathbf{R}_j} \quad (4.3)$$

in the derivative is one. Here, due to the invariance of the exponential function under differentiation, the object remains unchanged except for a multiplication with the imaginary unit

$$\frac{\partial}{\partial \tilde{O}_{\mathbf{r}}} e^{i\tilde{O}_{\mathbf{r}}} \cdot P_{\mathbf{r}-\mathbf{R}_j} = ie^{i\tilde{O}_{\mathbf{r}}} \cdot P_{\mathbf{r}-\mathbf{R}_j} = i\psi_{j,\mathbf{r}}. \quad (4.4)$$

From this new derivative, we calculate the new gradients and derive the new update functions

$$\tilde{O}_{l+1,\mathbf{r}} = \tilde{O}_{l,\mathbf{r}} + \alpha \frac{-\phi_{j,\mathbf{r}}}{\max |\psi_{\mathbf{r}-\mathbf{R}_j}|^2} \cdot (i\psi_{\mathbf{r}-\mathbf{R}_j})^*, \quad (4.5a)$$

$$P_{l+1,\mathbf{r}} = P_{l,\mathbf{r}} + \beta \frac{-\phi_{j,\mathbf{r}+\mathbf{R}_j}}{\max |e^{i\tilde{O}_{l,\mathbf{r}+\mathbf{R}_j}}|^2} \cdot e^{-i\tilde{O}_{l,\mathbf{r}+\mathbf{R}_j}}. \quad (4.5b)$$

We will refer to this variant as the refractive ptychographical iterative engine (refPIE). From these two updates we can derive a general rule to convert a ptychography algorithm, for example difference-map (DM), into a refractive variant that works directly on the effective absorption index and the phase shift:

- Wherever the object  $O$  is a factor in a multiplication, replace it with  $e^{i\tilde{O}}$
- In the object update replace the probe  $P$  with  $i\psi$ , the wavefield multiplied with the imaginary unit.

## 4.2 Simulation tests

We test refPIE on a simulated experiment to verify that the algorithm reconstructs the projection of the complex refractive index. The simulation imitates a typical X-ray ptychography experiment on a weakly scattering sample. All essential parameters are collected in Table 4.1. The simulated modulus and phase together with the probe are shown in Figure 4.1. The sample is scanned in a  $21 \times 21$  grid with a step size of  $1 \mu\text{m}$ . The total scanned area is indicated by a red square. Each position is randomly

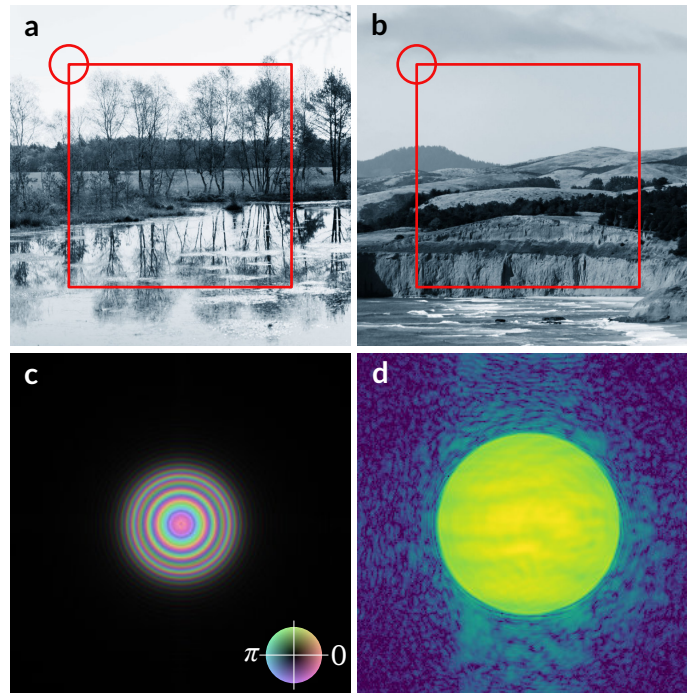


**Figure 4.1** Ptychography simulation set-up. **a** The sample modulus. **b** The sample phase shift. The squares in **a** and **b** indicate the scanned area, the circles show the extent of the illumination. **c** The probe in complex colouring. **d** A typical diffraction pattern in logarithmic display.

**Table 4.1** Parameters used in simulation.

Parameters	Simulation
Wavelength	1 Å
Detector distance	8000 mm
Detector pixel	75 μm × 75 μm
Image size	256 × 256 pixels
Pixel size (rec.)	41.7 nm
Scan size	21 × 21
Step size	1.000 ± 0.125 μm
Object modulus	[0.8; 1.0]
Object phase	[−π/2; 0]
Probe diameter	3.5 μm
Photons	10 <sup>9</sup>

offset by up to 0.125 μm in the vertical and horizontal direction to avoid scan grid artefacts [Thi+09]. The probe is modelled to replicate a CRL stack of 50 Beryllium lenses at a photon energy of 12.4 keV. Each lens has two parabolic surfaces of 50 μm

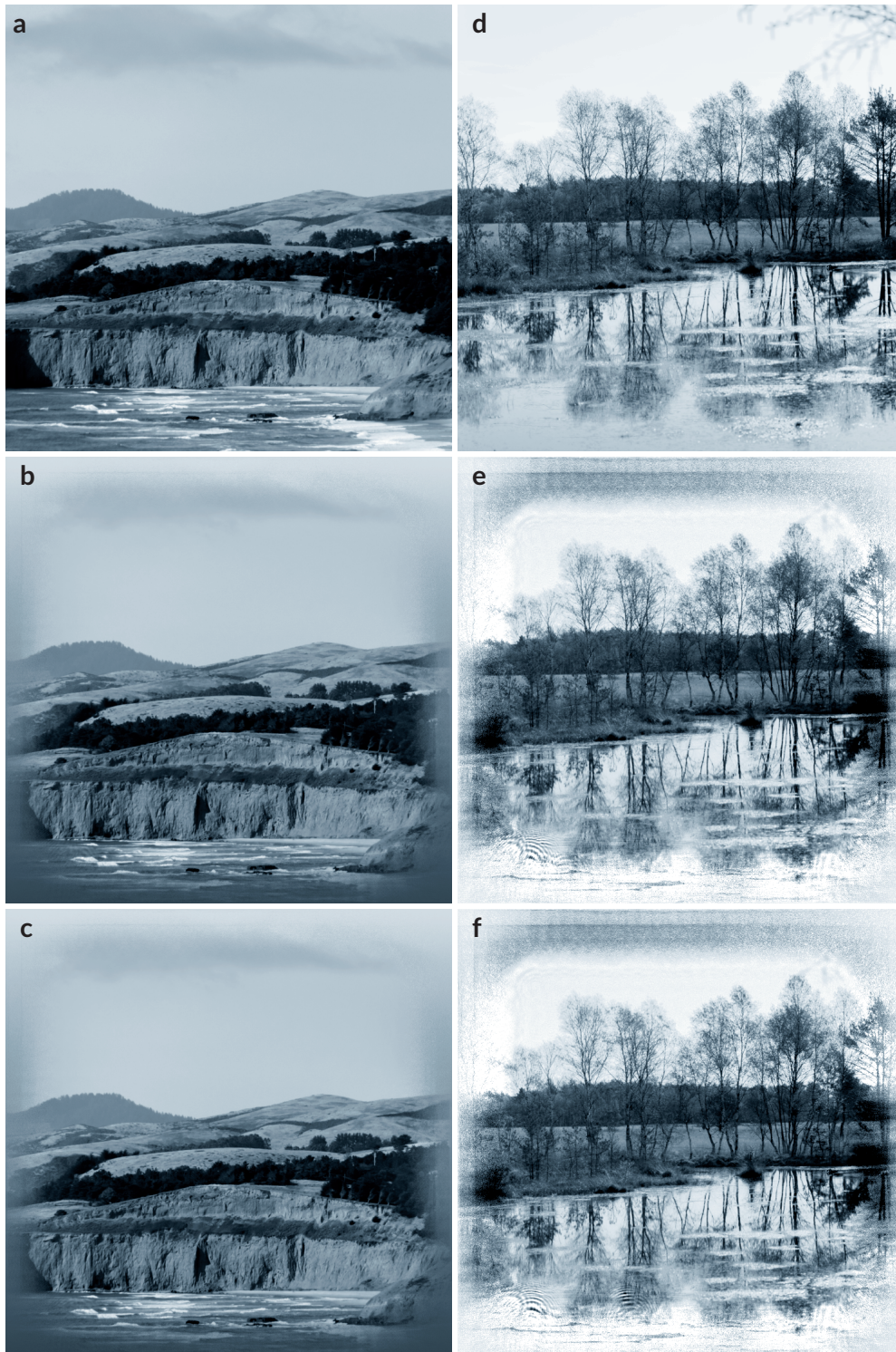
curvature, and the whole stack has a focal length of 235 mm with a diffraction-limited spot size of 72 nm. The sample is placed 3 mm downstream of the focal plane, where the probe extends to 3.5  $\mu\text{m}$  diameter. To simulate an average photon count of  $10^9$ , Poisson noise is added to each diffraction pattern.

The reconstruction is run in two ways: first with the conventional ePIE algorithm and then with the new refPIE algorithm. Both algorithms start with a transparent object and a 4  $\mu\text{m}$  sized disc with a spherical wavefront of 3 mm curvature as probe. Both reconstructions are run for 1000 iterations. The randomization seed is fixed at the start, so that the patterns are shuffled the same way for both algorithms. This ensures that no differences are introduced due to the subiteration order.

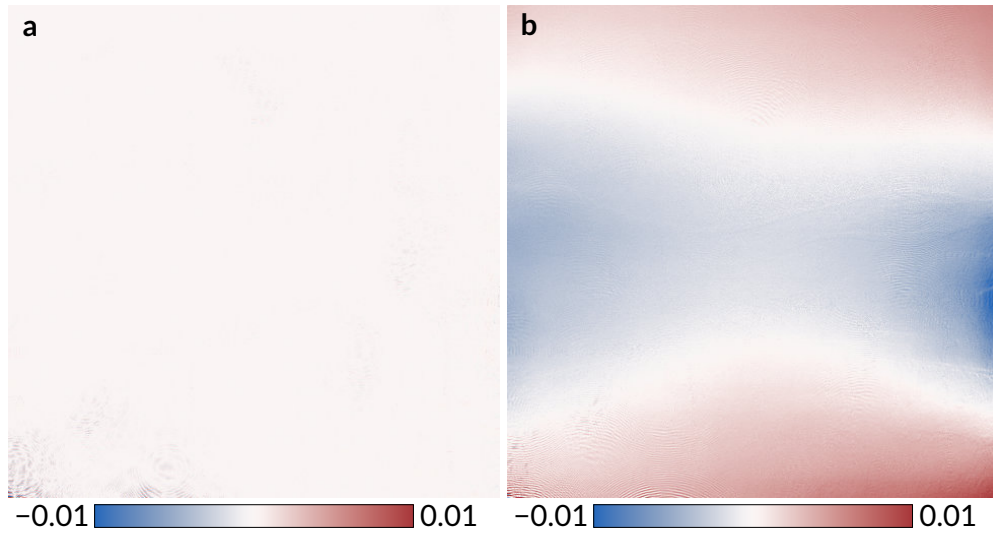
The reconstruction results from ptychography are not unique and can be ambiguous, thereby making the comparison between different runs and/or the reference challenging. For a more reliable comparison, these ambiguities must be removed; Appendix A.2 describes this procedure in detail. Here, we remove the ambiguities of the reconstructions in reference to the simulated sample.

Figure 4.2 compares the reconstructed moduli and phase shifts to the original sample. Both reconstructions match the original sample visually, they only start to deviate outside of the scanned area. The refractive reconstruction fulfills the expectations. Comparing Figure 4.2b to 4.2c and Figure 4.2e to 4.2f, the differences are imperceptible. Figure 4.2b and 4.2c both show the phase of the sample. However, it must be stressed that they are computationally two different entities. Figure 4.2b is the *argument* of the reconstructed object, whereas 4.2c is the *real part* of the reconstructed object. The situation is similar for Figure 4.2e and 4.2f, where the former shows the modulus of the reconstructed object and the latter shows the exponential of the negative imaginary part of the reconstructed object.

To see the slight distinctions between the two reconstructed objects we look at Figure 4.3 which shows the difference between the ePIE and refPIE reconstruction. Figure 4.3a shows the difference between the moduli; only faint features and a few striped patches are visible. The root mean square (rms) of the modulus difference is only  $0.24 \times 10^{-3}$ . The phase shift in Figure 4.3b, on the other hand, shows a stronger difference with a slowly varying saddle. Artifacts of low spatial frequency are a known weakness in ptychography, since it takes many iterations for local changes to affect the whole image. Apart from this saddle, there are only small differences, similar to the modulus in Figure 4.3a. Overall the  $2.7 \times 10^{-3}$  rms phase difference is an order of magnitude larger than the modulus, but still very small compared to the total phase range of  $\pi/2$ . This simulation demonstrates for weakly scattering samples that refPIE can reconstruct directly the phase shift and effective absorption index and otherwise behaves identical to ePIE.



**Figure 4.2** Reconstruction results of the ptychography simulation. **a-c** Phase shift, all scaled to the simulated phase range. **d-f** Modulus, all scaled to the simulated modulus range. **a, d** Original. **b, e** ePIE reconstruction with the ambiguities removed. **c, f** refPIE reconstruction with the ambiguities removed.



**Figure 4.3** Difference between ePIE and refPIE reconstruction. The images are cropped to the scanned area. **a** Difference between the two moduli, showing a uniform weak distribution. **b** Difference between the phase shifts, exhibiting a long range saddle but otherwise only weak errors.

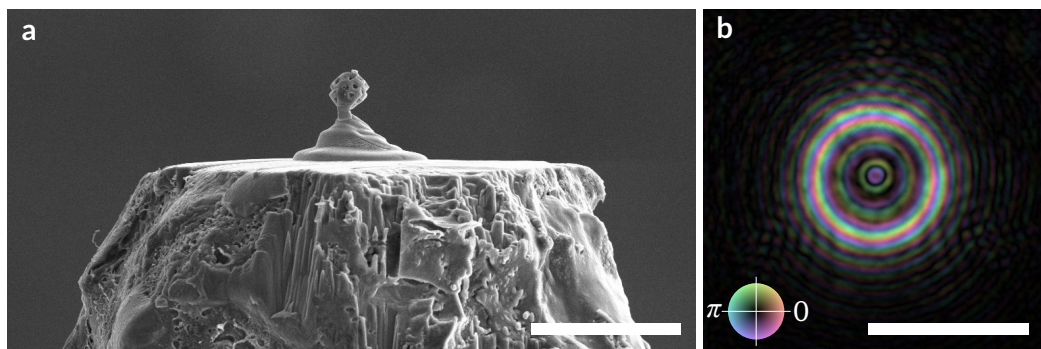


**Figure 4.4** Image of the zeolite and the probe. **a** The SEM image shows the top of the sample pin, where the zeolite is glued with platinum. The scale bar represents  $10\ \mu\text{m}$ , the zeolite particle is about  $2.6\ \mu\text{m}$  in size and the pin has a width of  $30\ \mu\text{m}$ . **b** Complex coloured display of the probe in the sample plane. The scale bar represents  $2\ \mu\text{m}$ , the probe is a little smaller with a diameter of roughly  $1.9\ \mu\text{m}$ .

### 4.3 Zeolite experiment

We continue after the successful reconstruction of the simulated experiment with data from a synchrotron radiation measurement of a zeolite particle [Kah+19; Wei+19]. The zeolite was measured at the P06 beamline at PETRA III in Hamburg using the ptychographic nano-analytical microscope (PtyNAMi) [Sch+17; Sch+20]. Zeolites are porous silicates that are important for catalysis due to their large inner surface.

**Table 4.2** Parameters of the zeolite experiment.

Parameters	Zeolite
Energy	9 keV
Flux	$2.6 \times 10^8$ ph/s
Exposure	1 s
Scan size	$11 \times 11$
Step size	$400 \pm 50$ nm
Probe diameter	1900 nm
Detector distance	2310 mm
Detector pixel	$75 \mu\text{m} \times 75 \mu\text{m}$
Image size	$512 \times 512$ pixels
Pixel size (rec.)	8.3 nm

Investigating their internal structure might help to produce new particles with a larger surface-to-volume ratio. To change the properties and catalytic activity of the zeolites, metallic atoms such as aluminium, titanium or zinc are commonly incorporated. The zeolite in this X-ray ptychographic computed tomography (XPCT) experiment is mostly made from silicon and titanium and has a diameter of  $2.6 \mu\text{m}$ . A scanning electron micrograph of the zeolite glued to the sample holder is given in Figure 4.4a. The zeolite itself scatters X-rays at 9 keV only weakly, but the platinum that glues the zeolite to the sample holder is a strong scatterer and is thick enough to cause phase wrapping in the reconstruction. To successfully reconstruct the tomogram, these phase wraps must then be unwrapped.

The experiment was conducted at 9 keV and the X-ray beam was focused by a combination of a central stop with a diameter of  $50 \mu\text{m}$ , an order sorting aperture with a diameter of  $35 \mu\text{m}$  and a FZP with a diameter of  $125 \mu\text{m}$  and with an outermost zone width of  $70 \text{ nm}$ . The sample was placed  $1.1 \text{ mm}$  downstream of the focus, where the beam diameter was  $1.9 \mu\text{m}$ . The probe in this plane is shown in Figure 4.4b in complex colouring. The sample was scanned in an  $11 \times 11$  grid of  $400 \text{ nm}$  steps where each scan point was randomly offset in the horizontal and vertical direction by up to  $\pm 50 \text{ nm}$ . At every point, a diffraction pattern with  $1 \text{ s}$  exposure was recorded with a single photon counting Eiger 4M detector [Joh+14]. The reconstructions use  $512 \times 512$  pixels of the Eiger image, resulting in a pixel size of  $8.3 \text{ nm}$  in the reconstructed images. All important scan parameters are summarized in Table 4.2.

First, we reconstruct the scan with ePIE. The initial guess for the reconstruction is a transparent object and a disc of  $1.8 \mu\text{m}$  with a wavefront curvature of  $1 \text{ mm}$  as probe. We run ePIE for 1000 iterations. The reconstructed object is shown in Figure 4.5, where the modulus of the air around the particle is normalized to one and the global gradient in the phase shift is removed. Since the zeolite is comprised of light elements,

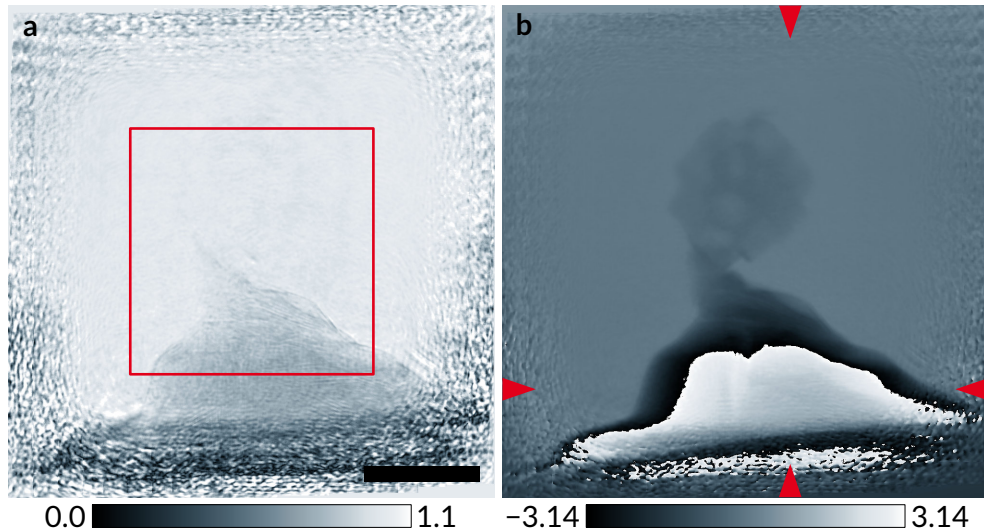


**Figure 4.5** ePIE reconstruction of the zeolite. **a** Modulus of the sample. The scale bar represents  $2\ \mu\text{m}$ . The square marks the scan area. **b** Phase shift of the sample. The arrows indicate where the line profiles in Figure 4.8 are extracted.

it is nearly invisible in the modulus of the reconstruction in Figure 4.5a. In comparison, the platinum glue below the zeolite is much more prominent. In the reconstructed phase shift in Figure 4.5b, the zeolite is well reconstructed and its internal structure is easily visible. Similar to the stronger phase contrast for the zeolite, the platinum at the bottom also has more contrast. The contrast is even strong enough to wrap the phase shift. The second phase wrap near the bottom is already part of the vastly bigger sample pin. The phase wraps are a problem for tomography, since it is not a simple projection of the three-dimensional phase distribution. Solving this requires additional procedures [CZ00; GZW88].

To circumvent the phase wraps, we reconstruct the dataset again with the refPIE algorithm, using the same initial object and probe and the identical subiteration shuffle. The reconstruction is run for 1000 iterations. For the comparison between this reconstruction and the previous one using ePIE, we first look at Figure 4.6, where the reconstruction errors over the iterations are plotted. Appendix A.3 describes how  $E_{\text{diff}}$ , the average error per diffraction pattern, is calculated. Both algorithms converge quickly to approximately the same error value, but ePIE is clearly faster. In particular, in the first iterations, the error in ePIE drops much faster, has a steeper slope, and is already well converged after 200 iterations. The error in refPIE also falls quickly, albeit slower than ePIE, and reaches a comparative level of convergence only after 300 iterations. This margin of 100 iterations between ePIE over refPIE remains the same for all following iterations. Nevertheless, the difference between the two after 1000 iterations is smaller than the jitter of each reconstruction.

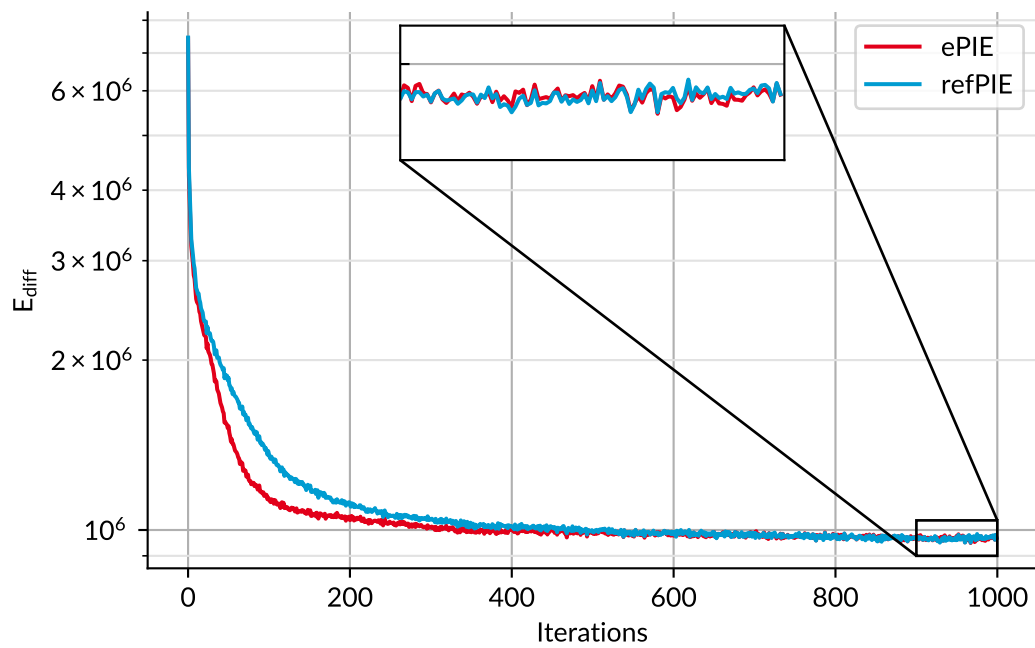


**Figure 4.6** Error of the zeolite reconstructions comparing ePIE and refPIE. The zoom-in shows the last 100 iterations. The error calculation is described in appendix A.3.

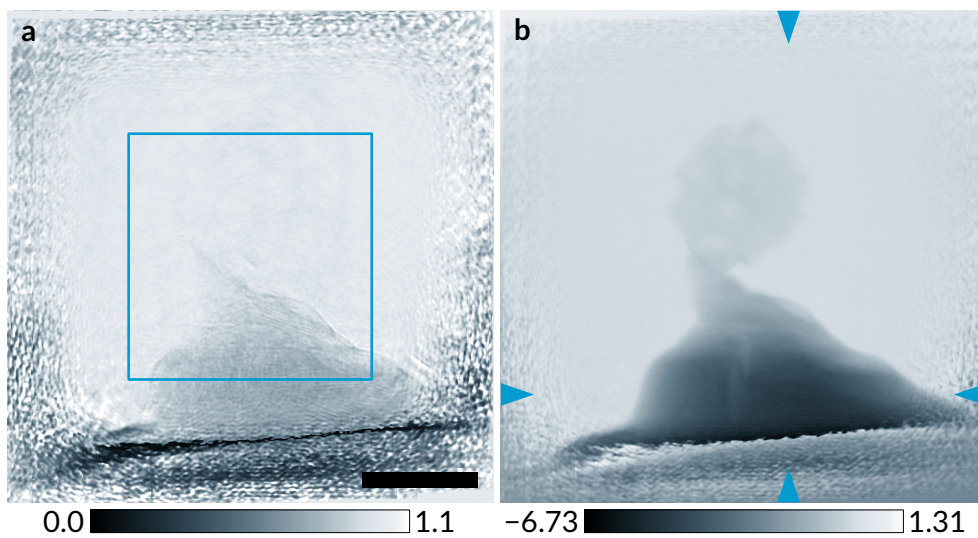


**Figure 4.7** refPIE reconstruction of the zeolite. **a** Modulus of the sample. Similar to the previous section for the simulation, this is again the exponential of the negative imaginary part of the reconstruction. The scale bar represents  $2\ \mu\text{m}$ , the square marks the scan area. **b** Phase shift of the sample. The arrows indicate where the line profiles in Figure 4.8 are extracted.

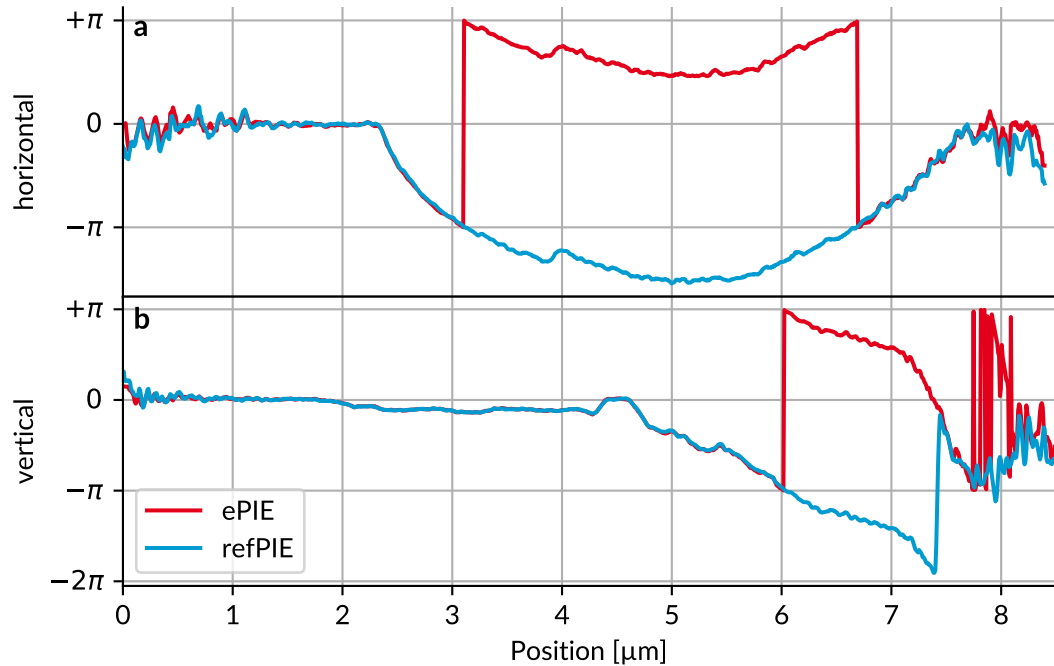


**Figure 4.8 Horizontal/Vertical profiles across the zeolite phase shift.** The profiles are plotted starting from the top-left. **a** Horizontal profile across the ePIE and refPIE reconstruction. **b** Vertical profile across the ePIE and refPIE reconstruction.

Figure 4.7 shows the reconstruction result from refPIE with the inherent ambiguities in ptychographic reconstructions removed (see Appendix A.2). Both ePIE and refPIE reconstruct nearly the same sample modulus. They match, except for a strongly absorbing horizontal band at the bottom of the refPIE reconstruction, outside the region of interest. This band is caused by the vastly bigger sample holder, compare Figure 4.4. The reconstructed phase on the other hand differs notably between the two algorithms. In the ePIE reconstruction, the phase shift in the glue jumps from  $-\pi$  to  $\pi$  over the span of a single pixel. Strikingly, the phase in the refPIE reconstruction is continuous and shows no jumps. Apart from the  $2\pi$  offset, the two reconstructions are identical, as can be seen in the horizontal and vertical phase profile in Figure 4.8. The curves only start to diverge near the edges, outside the scanned area, due to the noise in the reconstruction.

In conclusion, this section demonstrated a successful refPIE reconstruction of measured data that avoids the phase jumps which occur when ePIE is used. The phase wraps in this situation were rather weak, with the total phase shift of the sample being slightly more than  $2\pi$ . This situation could alternatively be resolved by shifting the range from  $[-\pi, \pi]$  to, for example,  $[-2\pi, 0]$ . Nonetheless, refPIE manages to fulfil the expectations and directly reconstructs the real and imaginary part of the projected

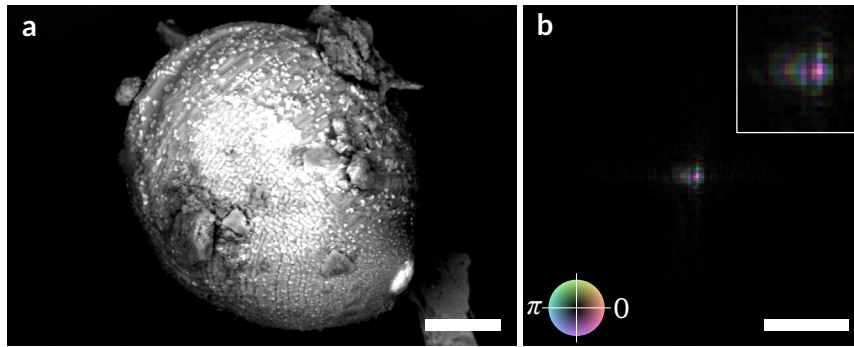


**Figure 4.9** Image of the micrometeorite and the probe. **a** SEM image of the micrometeorite. The tip of the sample pin can be seen on the bottom right. The scale bar represents 20  $\mu\text{m}$ , the particle is about 80  $\mu\text{m}$  in size. **b** Complex coloured display of the probe in the sample plane. The scale bar represents 2  $\mu\text{m}$ . In the upper right corner is a two times enlarged view of the 1.5  $\mu\text{m} \times 1.5 \mu\text{m}$  central region.

complex refractive index from measured data.

## 4.4 Micrometeorite

After the results for the reconstruction of the zeolite in the previous section, we will now look at a sample that is big enough to wrap the phase shift multiple times. The sample is a micrometeorite of 80  $\mu\text{m}$  diameter that is scanned in a combined ptychographic-fluorescence experiment to study its composition and structure. Micrometeorites are extraterrestrial particles found on Earth that are between 50  $\mu\text{m}$  and 1 mm in size. Every year about 40 000 t of new micro particles fall down, but only 10 % of these reach the ground [Mor15; TLH98]. Finding them among dust and human pollution is difficult and most are therefore found in Antarctica or deep sea sediments. However, if the dust from roofs that aggregates in the rain gutter is filtered and carefully selected, micrometeorites can be found even in urban areas [Gen+17]. The urban micrometeorite used in this study is mostly made out of olivine and traces of iron, cobalt and nickel. Olivine is a mineral made of magnesium silicate and iron silicate. Due to the olivine, the micrometeorite creates a strong phase shift that makes it an ideal test case for refractive ptychography.

The experiment was performed by Dennis Brückner at the P06 beamline of PETRA III in Hamburg, using the combined micro-/nanoprobe set-up for a long detector distance. The 18 keV X-ray beam was focused by a pair of KB-mirrors, focal length 250 mm, to a full width at half maximum (FWHM) spot size of 110 nm  $\times$  110 nm. The sample was placed 500  $\mu\text{m}$  behind the focus where the beam had expanded so that 50 % of the total beam intensity fell within a 190 nm  $\times$  190 nm circle. To quickly scan a sample of this size, the scanning stage never stopped but moved continuously in

**Table 4.3** Parameters of the micrometeorite experiment.

Parameters	Micrometeorite
Energy	18 keV
Flux	$3.75 \times 10^8$ ph/s
Exposure	1 ms
Scan size	$100 \mu\text{m} \times 100 \mu\text{m}$
Step size	$200 \text{ nm} \times 200 \text{ nm}$
Probe diameter	190 nm
Detector distance	8752 mm
Detector pixel	$75 \mu\text{m} \times 75 \mu\text{m}$
Image size	$128 \times 128$ pixels
Pixel size (rec.)	62.8 nm

zigzags across the sample. These fly-scans allow acquisition rates in the kilohertz range [Cla+14; Pel+14]. The micrometeorite was scanned over a  $100 \mu\text{m} \times 100 \mu\text{m}$  area with 1 ms exposure for each diffraction pattern. The velocity of the stage was set to  $200 \mu\text{m s}^{-1}$ , so that it moved 200 nm during one exposure. Each new line was vertically offset similarly by 200 nm. One scan recorded more than a quarter of a million diffraction patterns in less than 9.5 min. The diffraction patterns were recorded with an Eiger 500k situated 8.75 m downstream of the sample in the nanoprobe hutch. A 7 m long evacuated flight tube between sample and detector reduced air scattering on the detector. The reconstructions use the central  $128 \times 128$  pixels of the Eiger images, resulting in a pixel size of 62.8 nm in the ptychographic reconstruction. All parameters are summarized in Table 4.3.

The probe is very small compared to the overall sample size, leading to a slow convergence of long-range features in the ptychographic reconstruction. To accelerate the convergence, we use momentum accelerated gradients for both algorithms, as described in Section 3.4. We set the momentum damping factors  $\eta_{\text{obj}}$  and  $\eta_{\text{prb}}$  to 0.98 and apply the momentum to every second iteration. For this dataset the classic sequential ptychographic update easily gets stuck in wrong solutions. To avoid this, we use the parallel ptychography variant described in Section 3.2 for both ePIE and refPIE. We also constrain the object modulus to only range from 0.2 to 2.0.

Both reconstructions start with a transparent object and a 250 nm Gaussian with a phase curvature of 0.75 mm radius as probe. We run each reconstruction for 1000 iterations. For ePIE, the reconstructed sample modulus and phase shift are shown in Figure 4.10. The reconstruction shows phase wraps and two phase vortices at the top of the meteorite. These singularities are especially problematic for tomographic reconstructions.

This problem is solved by refPIE. The refractive reconstruction is shown in Fig-

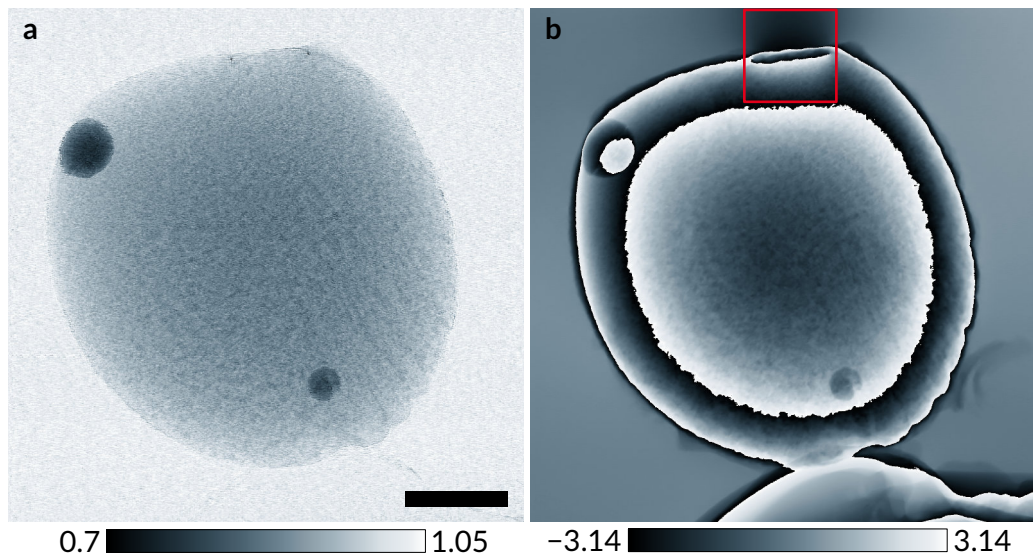


**Figure 4.10 ePIE reconstruction of the micrometeorite.** **a** Modulus of the micrometeorite. The scale bar represents  $20\ \mu\text{m}$ . **b** Phase shift of the micrometeorite, showing multiple phase wraps. A closeup of the two vortices at the top is shown in Figure 4.12a.

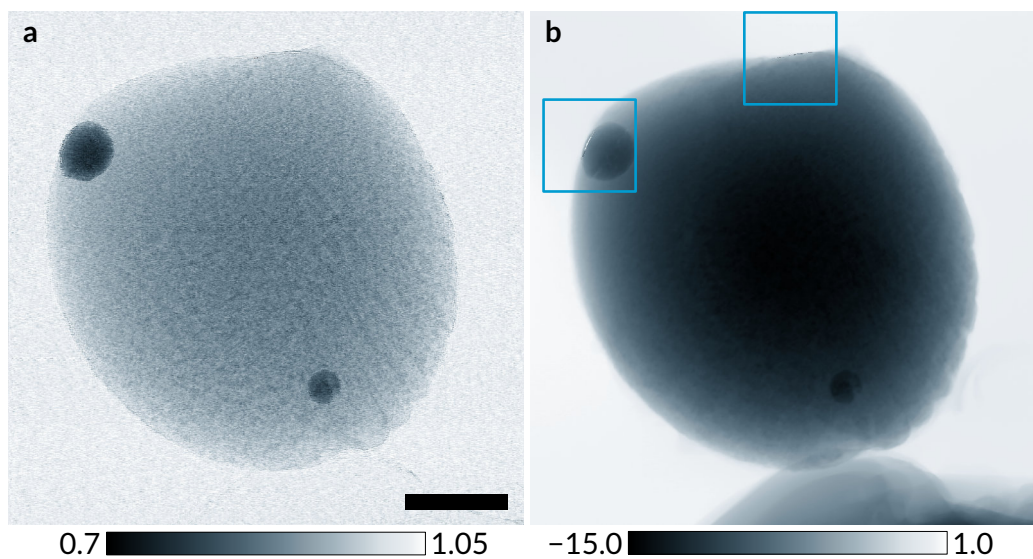


**Figure 4.11 refPIE reconstruction of the micrometeorite.** **a** Modulus of the micrometeorite. As before, this is again the exponential of the negative imaginary part of the reconstruction. The scale bar represents  $20\ \mu\text{m}$ . **b** Phase shift of the micrometeorite. The phase is continuous, except for two small areas where the gradient is steepest and the algorithm has difficulties. Close-ups of the two regions are shown in Figure 4.12b, c.

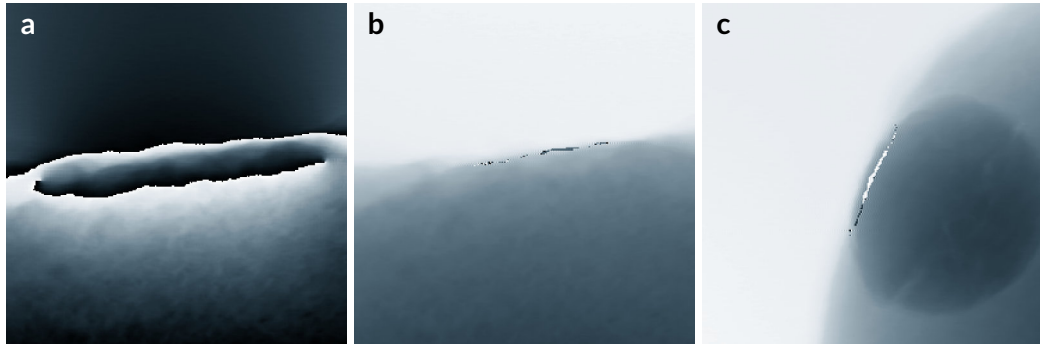


**Figure 4.12** Details from the ePIE and refPIE reconstructions of the micrometeorite. All images have a field of view of  $18\ \mu\text{m} \times 18\ \mu\text{m}$ . **a** The two vortices in the ePIE reconstruction. **b** The same region in the refPIE reconstruction only has a few small artefacts. **c** Artefact in the top left of the refPIE reconstruction. This artefact is offset by  $\pm 2\pi$  to the rest of the meteorite and can easily be fixed.

ure 4.11. Notably, the real part of the reconstructed projection of the complex refractive index, the phase shift, is continuous and shows no phase wrapping, while having a maximum phase shift of about 15 rad. Two small areas at the top and the top left contain wrong values. These areas have the largest phase slope and both ePIE and refPIE struggle in the reconstruction. The top left area is simply offset by  $2\pi$ , which can be easily fixed. The top area is exactly where the vortices are in ePIE and demonstrates exemplarily that refPIE is able, even in challenging circumstances, to reconstruct the unaffected parts of the sample without detriments.

The reconstruction errors  $E_{\text{diff}}$  in Figure 4.13 for both reconstructions are nearly identical. Here, again, refPIE falls behind in the beginning with a margin of about 20 iterations to ePIE. But at iteration 400 refPIE first catches up to ePIE and then even overtakes it around iteration 500. Afterwards both reconstructions are converged and show only minuscule improvements.

## 4.5 Conclusion

In summary, we have developed refPIE, the refractive ptychographical iterative engine, which reconstructs the projected complex refractive index of the sample. We demonstrated this capability on simulated and measured data for weakly and strongly scattering samples. Especially the last sample, the micrometeorite, shows the advantage of avoiding phase wrapping. The strong phase shift of up to 15 rad creates two phase jumps, which is challenging for ePIE. Phase jumps, especially if there are multiple, are often not accurately reconstructed, which can create phase vortices. The vortices might be removed [Sto+15], but this requires monitoring for vortices and is no guarantee that they will not reappear in later iterations.

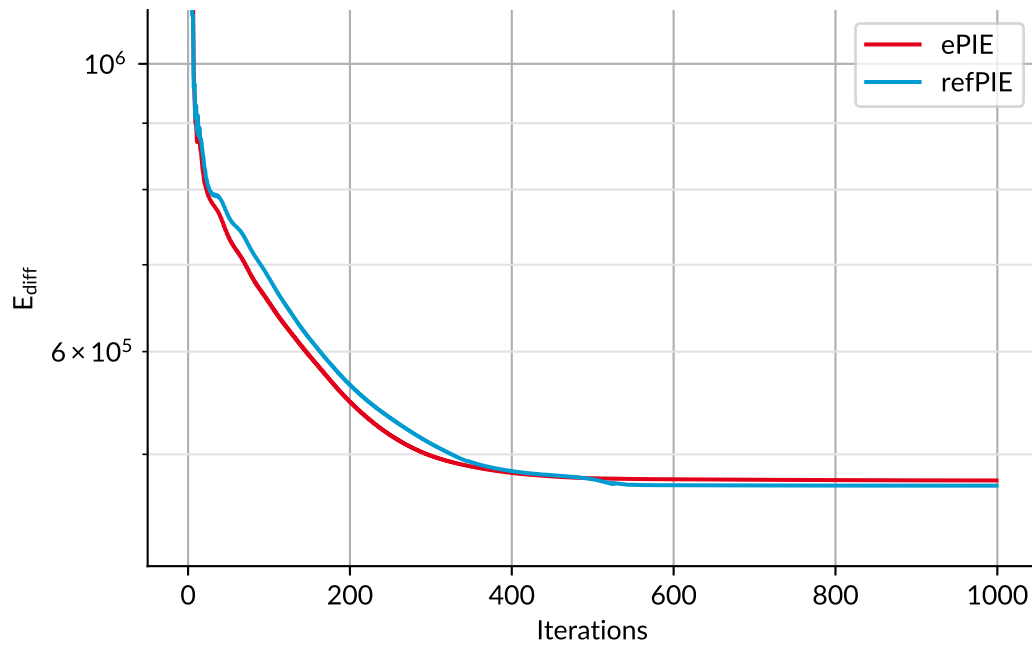


**Figure 4.13** Error of the micrometeorite reconstructions comparing ePIE and refPIE. The error calculation is described in appendix A.3.

At the end of Section 4.1 we outlined how other ptychography algorithms can be converted into a refractive variant. In the next chapter we will generalize this idea and show that other phase retrieval techniques can also be transformed to reconstruct the projected complex refractive index.



# 5 Refractive Phase Retrieval

In this chapter we generalize the principle behind refractive ptychography to other phase retrieval techniques. For Fourier ptychography, Chowdhury *et al.* already demonstrated a refractive algorithm [Cho+19]. We start in Section 5.1 with the development of a refractive holography algorithm that allows inline near-field holography (NFH) [Clo+99; Gab48] to reconstruct the projected refractive index. In Section 5.2 we establish a refractive CXDI algorithm that is marked by a more consistent reconstruction result compared to the standard difference-map (DM) algorithm.

## 5.1 Inline near-field holography

Inline near-field holography is a phase retrieval technique similar to ptychography [AO01; Mis73]. In holography, the sample is scanned in the X-ray beam along the optical axis and images, called holograms, are captured at different distances. It is also possible to reconstruct the sample from a single hologram, this is also called Fresnel CXDI and the reconstruction is analogous to CXDI in Section 5.2. We describe here therefore only multi-distance holography.

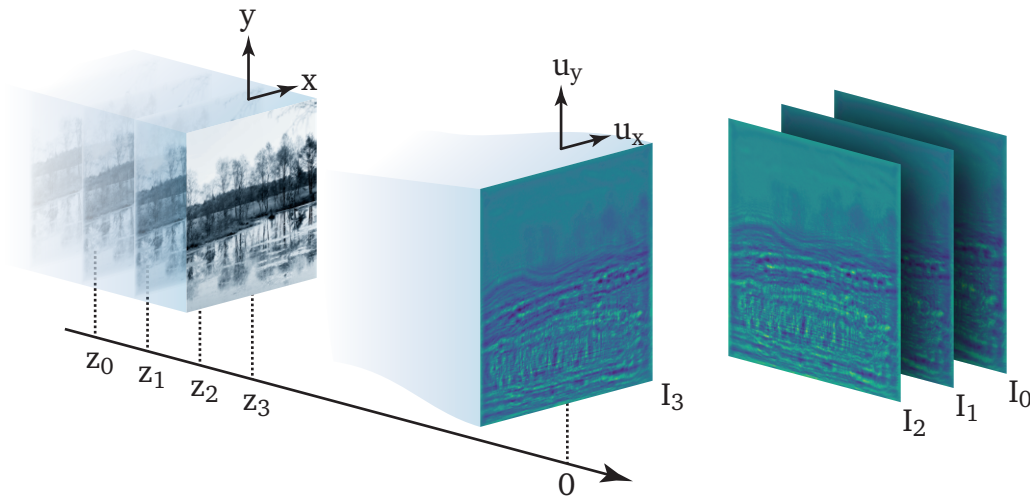


**Figure 5.1 Near-field holography set-up.** The sample is placed in the collimated X-ray beam at different distances  $z_j$  from the detector. The detector records a hologram  $I_j$  for each distance.

### 5.1.1 Reconstruction algorithm

A typical holography set-up is shown in Figure 5.1. The partially coherent X-ray beam illuminates the sample, the X-rays scatter off the sample, interfere with the original beam and both propagate to the imaging detector, which records the resulting hologram  $I_j$ . For the scan, the sample is moved along the beam to different positions  $z_j$ , varying the propagation distance. Since the detector is positioned in the optical near-field of the sample, the propagation can be described by Fresnel propagation, as outlined in Section 2.1.1.

Expressed in mathematical form, the wavefield  $\psi_{\mathbf{r}}$ , describing the interference between the original and the scattered beam, propagates over a set of distances  $z_j$  to the imaging detector

$$\psi_{j,\mathbf{u}} = \mathcal{P}_{z_j}(\psi_{\mathbf{r}}), \quad (5.1)$$

where the holograms

$$I_{j,\mathbf{u}} = |\psi_{j,\mathbf{u}}|^2 \quad (5.2)$$

are recorded. To reconstruct the sample, we back-propagate the hologram, which is spoiled by artefacts without knowing the phases (see Section 2.4). Each hologram is also missing specific spatial frequencies, but by measuring multiple holograms at different propagation distances, these gaps can be filled in [Zab+05]. For the reconstruction algorithm, similar to ptychography in Section 3.1, we start with a quadratic error function

$$L = \sum_j \sum_{\mathbf{u}} \left( \sqrt{I_{j,\mathbf{u}}} - \sqrt{n_{j,\mathbf{u}}} \right)^2, \quad (5.3)$$

that measures the agreement between the modelled holograms  $I_j$  and the measured holograms  $n_j$ . We reconstruct the sample by minimizing this error function. For this, we need to calculate the gradient with respect to the scattered wavefield

$$\frac{\partial L}{\partial \psi_{\mathbf{r}}} = \sum_j \sum_{\mathbf{u}} \frac{\partial \left( \sqrt{I_{j,\mathbf{u}}} - \sqrt{n_{j,\mathbf{u}}} \right)^2}{\partial I_{j,\mathbf{u}}} \cdot \frac{\partial I_{j,\mathbf{u}}}{\partial \psi_{\mathbf{r}}}, \quad (5.4)$$

similar to Section 3.1 by using Wirtinger derivatives, see Appendix A.1. The first factor can be calculated straightforward

$$\frac{\partial \left( \sqrt{I_{j,\mathbf{u}}} - \sqrt{n_{j,\mathbf{u}}} \right)^2}{\partial I_{j,\mathbf{u}}} = \left( 1 - \frac{\sqrt{n_{j,\mathbf{u}}}}{\sqrt{I_{j,\mathbf{u}}}} \right). \quad (5.5)$$

For the second factor, we need to calculate the derivative of the Fresnel propagation we defined in Equation 2.8. Using the Fresnel kernel  $H_z$  and the definition of the

discrete Fourier transform (DFT), we get

$$\frac{\partial I_{j,\mathbf{u}}}{\partial \psi_{\mathbf{r}}} = \psi_{j,\mathbf{u}}^* \cdot \frac{\partial \psi_{j,\mathbf{u}}}{\partial \psi_{\mathbf{r}}} \quad (5.6)$$

$$= \psi_{j,\mathbf{u}}^* \cdot \frac{\partial}{\partial \psi_{\mathbf{r}}} \mathcal{P}_{z_j}(\psi_{\mathbf{r}'}) \quad (5.7)$$

$$= \psi_{j,\mathbf{u}}^* \cdot \frac{\partial}{\partial \psi_{\mathbf{r}}} \mathcal{F}^{-1} \left( \mathcal{F}(\psi_{\mathbf{r}'}) \cdot H_{z_j,\mathbf{q}} \right) \quad (5.8)$$

$$= \psi_{j,\mathbf{u}}^* \cdot \frac{\partial}{\partial \psi_{\mathbf{r}}} \frac{1}{N} \sum_{\mathbf{q}} e^{-i\mathbf{q}\mathbf{u}} H_{z_j,\mathbf{q}} \sum_{\mathbf{r}'} e^{i\mathbf{q}\mathbf{r}'} \psi_{\mathbf{r}'}. \quad (5.9)$$

We can commute the sums with the partial derivative and have the second factor

$$\frac{\partial I_{j,\mathbf{u}}}{\partial \psi_{\mathbf{r}}} = \psi_{j,\mathbf{u}}^* \cdot \frac{1}{N} \sum_{\mathbf{q}} e^{-i\mathbf{q}\mathbf{u}} H_{z_j,\mathbf{q}} \sum_{\mathbf{r}'} e^{i\mathbf{q}\mathbf{r}'} \delta_{\mathbf{r}\mathbf{r}'} \quad (5.10)$$

$$\frac{\partial I_{j,\mathbf{u}}}{\partial \psi_{\mathbf{r}}} = \frac{1}{N} \cdot \psi_{j,\mathbf{u}}^* \sum_{\mathbf{q}} H_{z_j,\mathbf{q}} \cdot e^{-i\mathbf{q}\mathbf{u}} e^{i\mathbf{q}\mathbf{r}}. \quad (5.11)$$

When we combine the two factors, we get

$$\frac{\partial L}{\partial \psi_{\mathbf{r}}} = \sum_{j,\mathbf{q},\mathbf{u}} \frac{1}{N} \left( 1 - \frac{\sqrt{n_{j,\mathbf{u}}}}{\sqrt{I_{j,\mathbf{u}}}} \right) \psi_{j,\mathbf{u}}^* \cdot H_{z_j,\mathbf{q}} \cdot e^{-i\mathbf{q}\mathbf{u}} e^{i\mathbf{q}\mathbf{r}}. \quad (5.12)$$

We group the terms containing  $\mathbf{u}$  in one sum at the end of the equation and collect the terms depending on  $\mathbf{q}$  in another sum:

$$\frac{\partial L}{\partial \psi_{\mathbf{r}}} = \sum_j \frac{1}{N} \left\{ \sum_{\mathbf{q}} H_{z_j,\mathbf{q}} \cdot e^{i\mathbf{q}\mathbf{r}} \left[ \sum_{\mathbf{u}} \left( 1 - \frac{\sqrt{n_{j,\mathbf{u}}}}{\sqrt{I_{j,\mathbf{u}}}} \right) \psi_{j,\mathbf{u}}^* \cdot e^{-i\mathbf{q}\mathbf{u}} \right] \right\}. \quad (5.13)$$

Afterwards, we conjugate the gradient. This is necessary, since we are using Wirtinger derivatives, which are defined as  $\partial/\partial z = \partial/\partial x - i\partial/\partial y$ . This changes the sum over  $\mathbf{u}$  into a Fourier transform and vice versa the sum over  $\mathbf{q}$  is changed into an inverse Fourier transform. Conjugating the Fresnel kernel is identical to propagating in the opposite direction, so overall we get

$$\frac{\partial L}{\partial \psi_{\mathbf{r}}}^* = \sum_j \mathcal{F}^{-1} \left( H_{-z_j} \cdot \mathcal{F} \left( \psi_j \cdot \left[ 1 - \frac{\sqrt{n_j}}{\sqrt{I_j}} \right] \right) \right) \quad (5.14)$$

$$= \sum_j \mathcal{P}_{-z_j} \left( \psi_j \cdot \left[ 1 - \sqrt{n_j/I_j} \right] \right) \quad (5.15)$$

$$= \sum_j \mathcal{P}_{-z_j} \left( \mathcal{P}_{z_j}(\psi) \cdot \left[ 1 - \sqrt{n_j/I_j} \right] \right). \quad (5.16)$$

The gradient is the sum of the contributions of each propagation distance  $z_j$ . The contributions are calculated by first propagating the wavefield over the distance  $z_j$  to the detector plane. There, the difference between the estimated hologram  $I_j$  and the measured hologram  $n_j$  is calculated. The difference is then propagated back to the sample plane.

For refractive holography, we cannot directly use the two conversion steps for ptychography algorithms from the end of Section 4.1, since holography does not separate the exit wavefront into illuminating probe and object. Therefore, we start again by propagating the refractive object

$$\psi_{j,\mathbf{u}} = \mathcal{P}_{z_j}(\mathbf{e}^{i\tilde{O}_r}). \quad (5.17)$$

We use the same nomenclature as in Chapter 4,  $\psi$  will remain the exit wavefront and  $\tilde{O}$  will be the refractive object. We call  $\arg(\psi) = \Re(\tilde{O})$  the phase shift of the object and  $|\psi| = e^{-\Im(\tilde{O})}$  its modulus.

The first difference in the calculation occurs in Equation 5.10. The exponential remains unaffected by the derivative and a new multiplication with the imaginary unit occurs. The steps afterwards are not affected, since the new term commutes with all sums. Finally, after the complex conjugation, we end up with nearly the same gradient

$$\frac{\partial L^*}{\partial \psi_r} = -i e^{-i\tilde{O}_r^*} \cdot \sum_j \mathcal{P}_{-z_j} \left( \mathcal{P}_{z_j}(\mathbf{e}^{i\tilde{O}}) \cdot \left[ 1 - \sqrt{n_j/I_j} \right] \right), \quad (5.18)$$

except for the additional factor  $-i \exp(i\tilde{O}^*)$ . To ensure a stable reconstruction, we slightly modify the two gradients in Equation 5.16 and Equation 5.18, by dividing each by the number of holograms  $M$  and the refractive variant also by the maximum modulus. In the end we get

$$\Delta O = \frac{1}{M} \sum_j \mathcal{P}_{-z_j} \left( \mathcal{P}_{z_j}(\psi) \cdot \left[ 1 - \sqrt{n_j/I_j} \right] \right) \quad (5.19)$$

$$\Delta \tilde{O} = -\frac{i \cdot O^*}{M \cdot \max |O|^2} \sum_j \mathcal{P}_{-z_j} \left( \mathcal{P}_{z_j}(O) \cdot \left[ 1 - \sqrt{n_j/I_j} \right] \right) \quad (5.20)$$

for the normal and refractive update functions, respectively, with  $O = \exp(i\tilde{O})$  for the refractive update.

### 5.1.2 Numerical simulation

We compare the two algorithms with a numerical simulation of polystyrene spheres. Polystyrene contains only carbon and hydrogen atoms, the small spheres have therefore a negligible absorption for 1 Å photons. Each sphere has a diameter of 70 μm

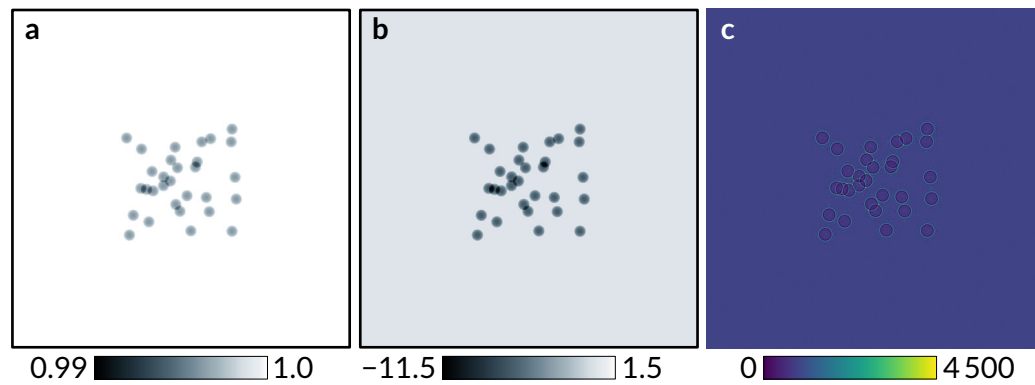


**Figure 5.2 Holography simulation.** **a** The sample modulus with surrounding padding. Colour scale in arbitrary units. **b** The sample phase shift with surrounding padding. Colour scale in radian. **c** One of the four holograms. Colour scale in photons.

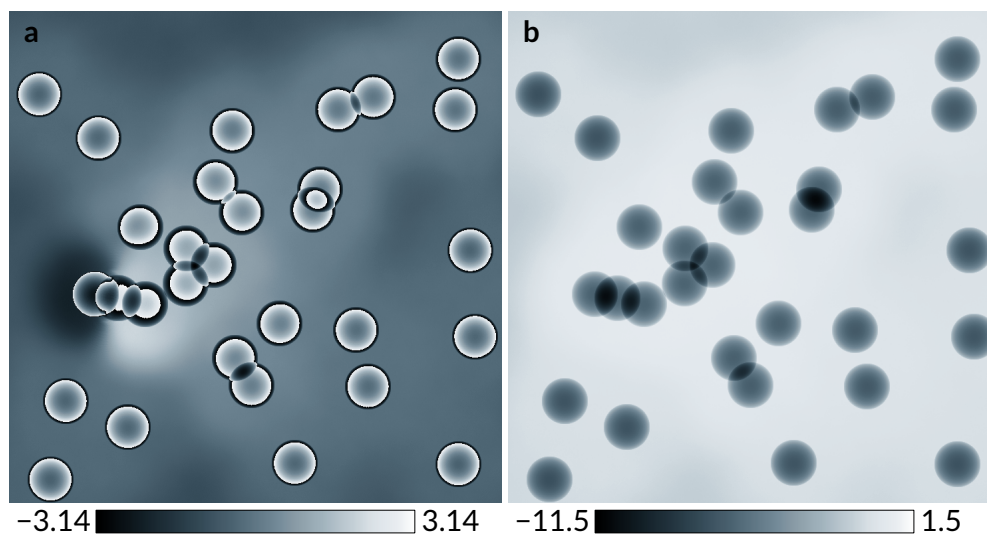


**Figure 5.3 Holographic phase reconstructions.** All ambiguities were removed relative to the original phase. Both images show the central part of the sample without the empty padding. **a** Standard holography reconstruction, limited to a phase range of  $2\pi$ . **b** Refractive holography reconstruction, the phase is continuous without any need for additional phase unwrapping.

**Table 5.1** Parameters used in the holography simulation.

Parameters	Simulation
Wavelength	1 Å
Detector distance	0.15, 0.25, 0.75 and 1.0 m
Fresnel number $\times 10^3$	66.7, 40.0, 13.3 and 10.0
Detector pixel	1 $\mu\text{m} \times 1 \mu\text{m}$
Detector size	2048 $\times$ 2048 pixels
Object modulus	[0.993; 1.0]
Object phase	[-11.3; 0.0]
Photons/pixel	910

and a maximum phase shift of 6.40 rad. The modulus and phase shift of the sample are shown in Figure 5.2.

Again, like in Section 4.2, the real part of the refractive object corresponds to the phase shift and the exponential of the negative imaginary part to the modulus. For ease of reading we call these *phase shift* and *modulus* of the refractive object. The detector pixel size is 1  $\mu\text{m}$  in parallel beam geometry, the magnification is therefore also one and the object pixel size is also 1  $\mu\text{m}$ . The wavelength of the X-rays is 1 Å. The simulation uses four holograms from four propagation distances: 0.15 m, 0.25 m, 0.75 m and 1.0 m. To simulate photon statistics, we add Poisson noise to each hologram equivalent to  $3.8 \times 10^9$  photons on the sample. All parameters are summarized in Table 5.1.

To accelerate the reconstruction, we add Nesterov accelerated gradient [MJL17; Rud17]. We do this similar to momentum-accelerated ptychography in Section 3.4. In each iteration  $l$ , we first update the momentum  $D_l$  with the update function

$$D_l = \eta D_{l-1} + \Delta O, \quad (5.21)$$

before we subtract the update and the momentum from the object

$$O_l = O_{l-1} - \Delta O - \eta D_l. \quad (5.22)$$

We set the momentum damping factor  $\eta$  to 0.99 and run the standard and refractive holography reconstruction for 2000 iterations each. To avoid local minima, we blur for the first 1000 iterations the reconstruction with a Gaussian filter with a  $\sigma$  of 2 pixels.

The reconstructed phases in Figure 5.3 illustrate the difference between the two algorithms. The phase of the refractive object is continuous and contains no phase jumps even though the total phase range is nearly  $4\pi$ . Contrarily, the phase in the standard reconstruction is wrapped and contains two phase vortices, which are an

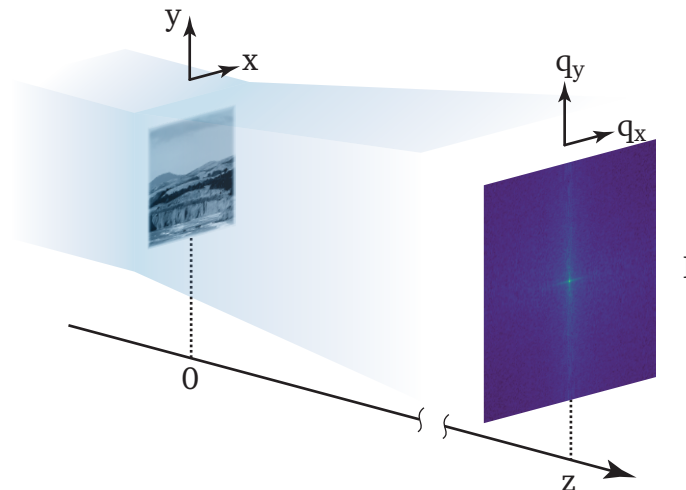


**Figure 5.4 CXDI scheme.** The sample is confined in a support. The support must be small enough so that the detector can fully resolve the diffraction patterns.

obstacle to direct unwrapping. Both images contain weak long-range artefacts, but the standard reconstruction contains additionally the artefacts from the vortices. The reconstructed moduli in both reconstructions contain no significant features because the original sample is practically transparent.

## 5.2 Refractive coherent diffractive imaging

Since Miao *et al.* have extended phasing algorithms from protein crystallography to non-crystalline samples [Mia+99], coherent X-ray diffraction imaging (CXDI) has become a widely used X-ray microscopy technique [CN10; Eke+15; New+10]. Unlike ptychography or holography, CXDI is able to reconstruct the exit wavefront from a single diffraction pattern if the sample is only inside a compact support. This allows for fast imaging schemes such as diffraction-before-destruction performed at XFELs [Cha+06].

CXDI is a lensless imaging technique with no optical elements between sample and detector. In Figure 5.4, a spatially isolated sample, typically on a membrane, is fully illuminated by a coherent X-ray beam. The beam is scattered by the sample and the resulting far-field diffraction pattern  $I$  is recorded by an imaging detector. The pixels of the detector must be small enough to correctly resolve the fringes in the diffraction pattern. As the size of the fringes is inversely proportional to the sample size, the diffraction patterns are resolved if the sample is small and confined to a compact support. If the propagation distance is shorter and in the Fresnel regime, this technique is called Fresnel CXDI. The reconstruction algorithms for this case are

nearly the same, only substituting the Fresnel for the Fraunhofer propagation.

Many algorithms have been developed to reconstruct single diffraction patterns [Mar07]. In this section, we will modify the commonly used difference-map (DM) algorithm to reconstruct the complex refractive index projection of the sample. The difference-map algorithm is an iterative algorithm that can be applied in many situations where a solution under two different constraints  $P_A$  and  $P_B$  is sought [ERT07; Els03]. These constraints are alternatively applied to refine the current estimate  $x_n$ . The order and strength of the constraints can be adapted to the problem at hand. In the simplest case, the update is

$$x_{n+1} = x_n + P_A(2P_B(x_n) - x_n) - P_B(x_n). \quad (5.23)$$

For CXDI, the two constraints are typically given by the support in the sample plane  $P_S$  and the diffraction pattern in the detector plane  $P_M$ . We use the phase-constrained DM algorithm, which assumes a pure phase object with no absorption for the reconstruction. This assumption is justified for thin samples that mostly consist of light elements, for example biological samples.

The first projector  $P_S$  constrains the wavefield  $\psi_n$  in the  $(x, y)$ -sample plane to a phase object inside the support area  $S$

$$P_S(\psi_n) = \begin{cases} \exp[i \cdot \arg(\psi_{n,\mathbf{r}})] & \text{if } \mathbf{r} \in S, \\ \exp[i \cdot 0] & \text{if } \mathbf{r} \notin S. \end{cases} \quad (5.24)$$

The second projector  $P_M$  constrains the wavefield in the  $(q_x, q_y)$ -detector plane to be consistent with the measured diffraction pattern

$$P_M(\psi_n) = \mathcal{F}^{-1} \left( \sqrt{I_q} \cdot \exp \{i \cdot \arg [\mathcal{F}(\psi_{n,\mathbf{r}})]\} \right). \quad (5.25)$$

In  $P_M$ , the wave is first propagated forward, then its modulus is replaced with the square root of the diffraction pattern  $I$  and finally it is propagated back to the sample plane. One iteration of DM combines both projectors to update the wavefield

$$\psi_{n+1} = \psi_n + P_M(2P_S(\psi_n) - \psi_n) - P_S(\psi_n). \quad (5.26)$$

For the refractive DM algorithm we modify the two constraints so that they act directly on the complex refractive index. We call the refractive wavefield  $\tilde{\psi}$  and the refractive constraints  $\tilde{P}_S$  and  $\tilde{P}_M$ . The standard and the refractive wave are related by the exponential function:

$$\psi_{n,\mathbf{r}} = \exp(i \cdot \tilde{\psi}_{n,\mathbf{r}}). \quad (5.27)$$

The modifications for  $\tilde{P}_S$  are straightforward. We retain only the real part inside the support:

$$\tilde{P}_S(\tilde{\psi}_n) = \begin{cases} \Re(\tilde{\psi}_{n,\mathbf{r}}) + 0i & \text{if } \mathbf{r} \in S, \\ 0 + 0i & \text{if } \mathbf{r} \notin S. \end{cases} \quad (5.28)$$

The modifications for  $\tilde{P}_M$  are more complex, as we need to propagate the wave into the far-field and back again. The first step is therefore to calculate the standard wave from the refractive wave with Equation 5.27. Then, we calculate the standard constraint using  $P_M$  to get the updated wavefield  $\psi'_n$ . Now we need to calculate the updated refractive wave  $\tilde{\psi}'_n$  from  $\psi'_n$ . For this, we work backwards from the refractive wave to the standard wave. We start by adding zero in the form of  $\tilde{\psi}_n$ :

$$\tilde{\psi}'_{n,\mathbf{r}} = \tilde{\psi}'_{n,\mathbf{r}} + (\tilde{\psi}_{n,\mathbf{r}} - \tilde{\psi}_{n,\mathbf{r}}). \quad (5.29)$$

Afterwards, we invert Equation 5.27 to replace two of the refractive waves with the logarithm of the standard wave

$$\tilde{\psi}'_{n,\mathbf{r}} = -(\mathbf{i} \cdot \log \psi'_{n,\mathbf{r}}) + \tilde{\psi}_{n,\mathbf{r}} + \mathbf{i} \cdot \log \psi_{n,\mathbf{r}}, \quad (5.30)$$

$$= \tilde{\psi}_{n,\mathbf{r}} - \mathbf{i} \cdot \log \frac{\psi'_{n,\mathbf{r}}}{\psi_{n,\mathbf{r}}}. \quad (5.31)$$

Because computing the logarithm is complex and computationally expensive, we replace it by a simpler calculation. For this, we approximate the logarithm by using the Taylor series up to the second order. The Taylor series of the logarithm around  $z = 1$  is

$$\log z \Big|_{z=1} = (z - 1) - \frac{(z - 1)^2}{2} + \dots \quad (5.32)$$

As the reconstruction converges, the fraction of  $\psi'_n$  and  $\psi_n$  will approach one and the logarithm will approach zero. Thus, the Taylor approximation will become more and more accurate with each iteration. We combine the Taylor series with Equation 5.31 to define the refractive constraint  $\tilde{P}_M$ :

$$\tilde{P}_M(\tilde{\psi}_n) = \tilde{\psi}_{n,\mathbf{r}} - \mathbf{i} \cdot \left[ \left( \frac{\psi'_{n,\mathbf{r}}}{\psi_{n,\mathbf{r}}} - 1 \right) - \frac{1}{2} \left( \frac{\psi'_{n,\mathbf{r}}}{\psi_{n,\mathbf{r}}} - 1 \right)^2 \right], \quad (5.33)$$

where  $\psi_n$  is given by Equation 5.27 and  $\psi'_n$  by Equation 5.25.

We test the refractive and the standard DM algorithm on a simulated experiment. For the test sample, we combine the phase shift from the ptychography test object with a uniform amplitude. We use the same phase range of  $\pi/2$  and a quadratic support of  $741 \times 741$  pixels. To allow sufficient oversampling, the sample is embedded into a larger,  $2048 \times 2048$  pixels array of uniform intensity using a mask function. The

**Table 5.2** Parameters used in the CXDI simulation.

Parameters	Simulation
Wavelength	1 Å
Detector distance	8192 mm
Detector pixel	40 μm × 40 μm
Detector size	2048 × 2048 pixels
Pixel size (rec.)	10 nm
Object size	7.41 μm × 7.41 μm
Object phase	$[-\pi/2; 0]$
Photons/pixel	23 840

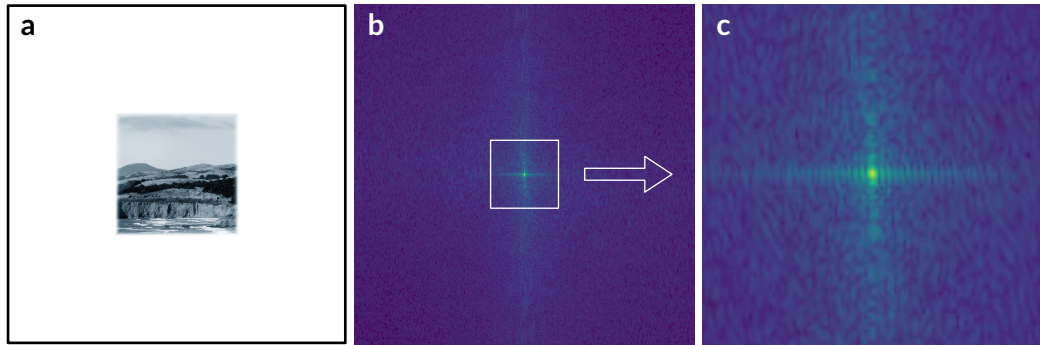


**Figure 5.5** CXDI simulation. **a** The sample phase shift with the surrounding embedding, scaled from  $-\pi/2$  to 0. **b** The diffraction pattern in logarithmic scale. The brightest pixel contains  $9.48 \times 10^{10}$  photons. **c** Zoomed in view of the central region, all fringes are well resolved.

mask function,  $1 - \exp(-d^2/2\sigma^2)$ , is a function of the distance  $d$  from the edge of the sample. The mask is zero at the edge and goes to one in the centre of the sample. The characteristic width  $\sigma$  is 20 pixels (200 nm). We add Poisson noise to the diffraction pattern to simulate a total photon count of  $10^{11}$ . This is equivalent to an average radiant exposure of 238.4 ph/nm<sup>2</sup>. All parameters of the simulation are summarized in Table 5.2. Figure 5.5 shows the phase shift of the sample and the simulated diffraction pattern.

The reconstructions, both standard and refractive, start in the detector plane with the square root of the diffraction pattern. For the initial guess, a random phase is assigned to each pixel and the pattern is propagated to the sample plane. For the support  $S$ , we use the central square of  $741 \times 741$  pixels that was used to define the sample. We run each algorithm for 300 iterations.

Figure 5.6 compares the original sample to the reconstructions from the standard and the refractive DM algorithm. As CXDI reconstructions can be ambiguous, all

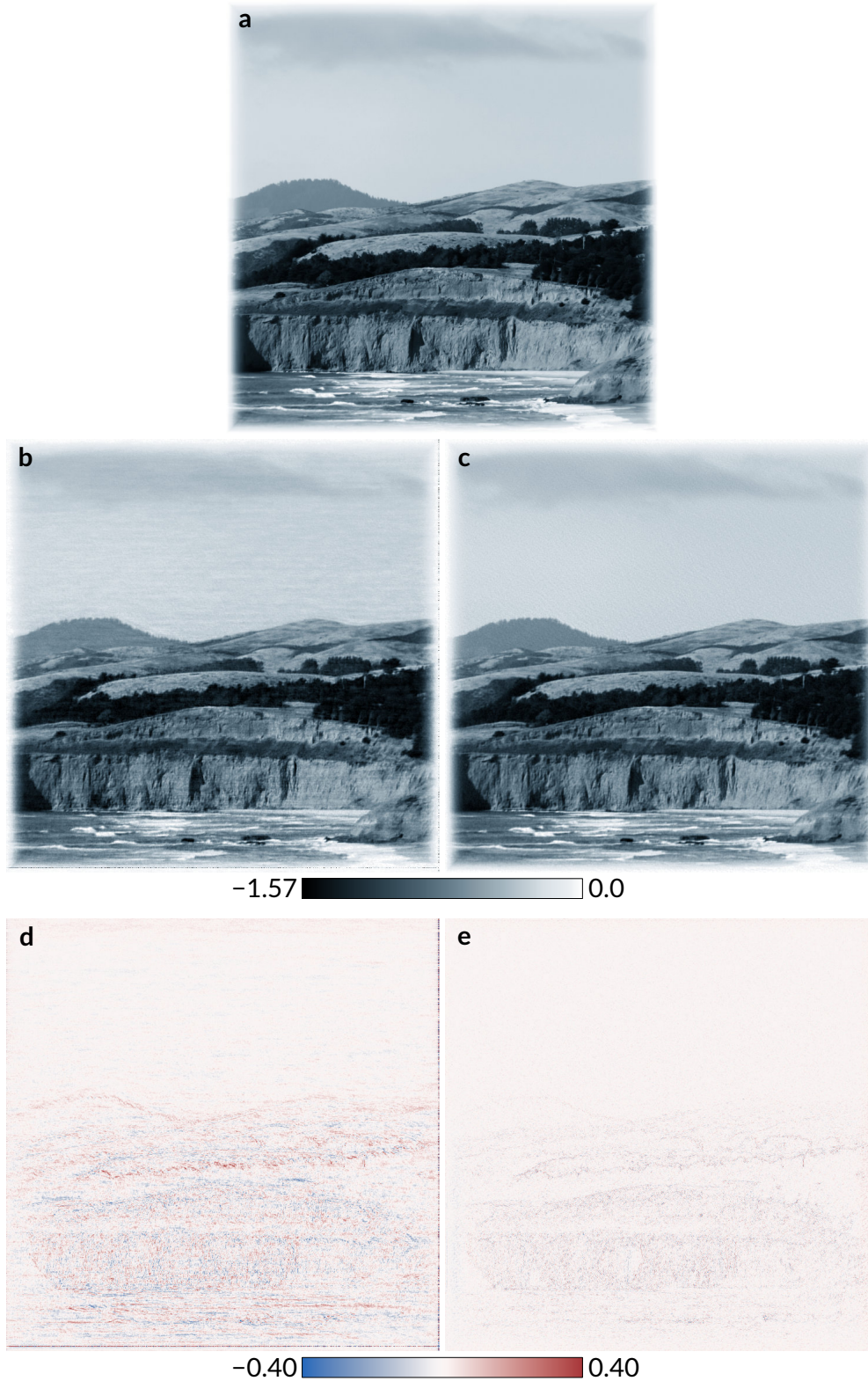


**Figure 5.6** Reconstructed phase shift of the CXDI simulation. The empty padding around the sample is removed. The images a-c and d,e use the same scaling respectively. **a** Original. **b** Standard DM reconstruction with the ambiguities removed. **c** Refractive DM reconstruction with the ambiguities removed. **d**, **e** Difference between the original phase shift and the standard or refractive reconstruction, respectively.

ambiguities are removed as described in Section A.2. The objects reconstructed by the two algorithms are slightly flawed. All main features are correctly reconstructed, but the finer details suffer from reconstruction artefacts. For instance, the sky in both reconstructions shows stripe and point patterns, while the sky in the original sample is flat. However, the pattern in the refractive reconstruction is not as strong as in the standard reconstruction and the fine details such as the tree lines turn out sharper.

To better highlight these artefacts and differences, we subtract each reconstruction from the original object. The resulting reconstruction errors are shown in Figures 5.6d and 5.6e. The artefacts in the refractive reconstruction are indeed weaker and smaller than in the standard reconstruction. As the difference-map algorithm is deterministic and the initial guess is random, this difference in reconstruction quality could be biased due to different starting points. To verify that the reconstruction of the refractive algorithm is closer to the original sample than the standard reconstruction, we run each algorithm 50 times on the same diffraction pattern. For each run, we create a new randomized initial guess for each algorithm. After each reconstruction, we remove the ambiguities from the result, align it to the original sample  $O$  as described in Section A.2 and calculate the error  $E_{\text{abs}}$ :

$$E_{\text{abs}} = \sum_{\mathbf{r} \in S} |\arg(\psi_{n,\mathbf{r}}) - \arg(O_{\mathbf{r}})|^2, \quad (5.34a)$$

$$E_{\text{abs}} = \sum_{\mathbf{r} \in S} |\Re(\tilde{\psi}_{n,\mathbf{r}}) - \arg(O_{\mathbf{r}})|^2. \quad (5.34b)$$

Equation 5.34a describes the error calculation for the standard reconstruction, Equation 5.34b for the refractive reconstruction.

All 100 errors are plotted in Figure 5.7, together with the median error for each algorithm. The median error of the refractive reconstructions is 510.6, less than a third of 1881.6, the median error of the standard reconstructions. This proves that the refractive reconstructions are repeatedly closer to the original sample than the standard reconstructions. The worst refractive reconstruction with the largest error is still better than over 80% of the standard reconstructions and the best 90% of the refractive reconstructions are better than all standard reconstructions. The reconstructions shown in Figures 5.6b and 5.6c have errors of 2532.1 and 480.8, respectively.

The result of a single CXDI reconstruction is highly dependent on the initial guess, as Figure 5.7 illustrates. To account for this, the sample is commonly reconstructed multiple times with different starting guesses and then averaged over all these reconstructions [Sch+08; Sha+05]. This way, only the correctly reconstructed features in the sample remain and the fluctuating, fine-scaled artefacts are suppressed. As the reconstructions are not unique and can be ambiguous, the reconstructions are aligned before we calculate the average. The average for each algorithm is shown

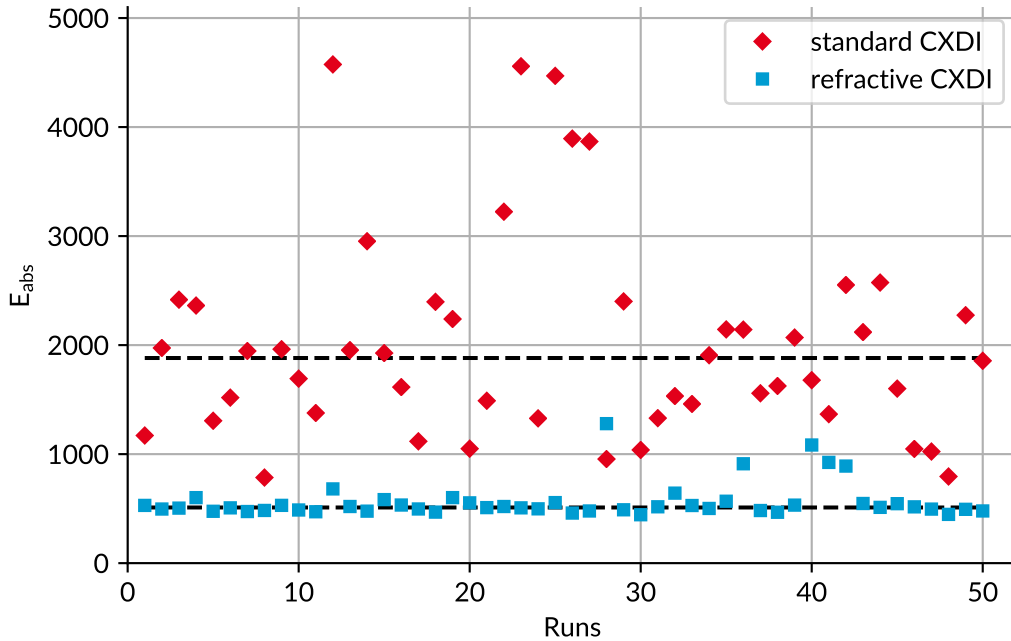


**Figure 5.7 Error of standard and refractive CXDI.** Error  $E_{abs}$  between each reconstruction and the original sample for 100 independent reconstructions, 50 with the standard and 50 with the refractive CXDI algorithm.  $E_{abs}$  is calculated according to Equation 5.34. The dashed black lines show the median errors (1881.6 for standard CXDI, 510.6 for refractive CXDI).

in Figure 5.8. Compared to the single individual reconstructions in Figure 5.6, the artefacts are imperceptible and the images are nearly indistinguishable. The only visible difference between the original and the reconstructions is a blurring, as the high-resolution features have the lowest signal-to-noise ratio in the diffraction pattern. It is only in the direct differences between the original and the averages that the two are distinguishable. The error values for both images also reflect the improved quality, both errors are smaller than any of their respective individual reconstructions. The error for the average of the standard reconstructions is 516.1, a third of the median error. Strikingly, the error of the average refractive reconstruction is only 270.5, far smaller than any individual reconstruction of either algorithm.

### 5.3 Conclusion

In this chapter, we have demonstrated that the idea to directly reconstruct the refractive index of the sample is not limited to ptychography and can be generalized to other phase retrieval techniques. Exemplary, we developed refractive holography and refractive coherent diffractive imaging. Refractive holography is derived with a least-square minimization and its performance is demonstrated on a simulated experiment.

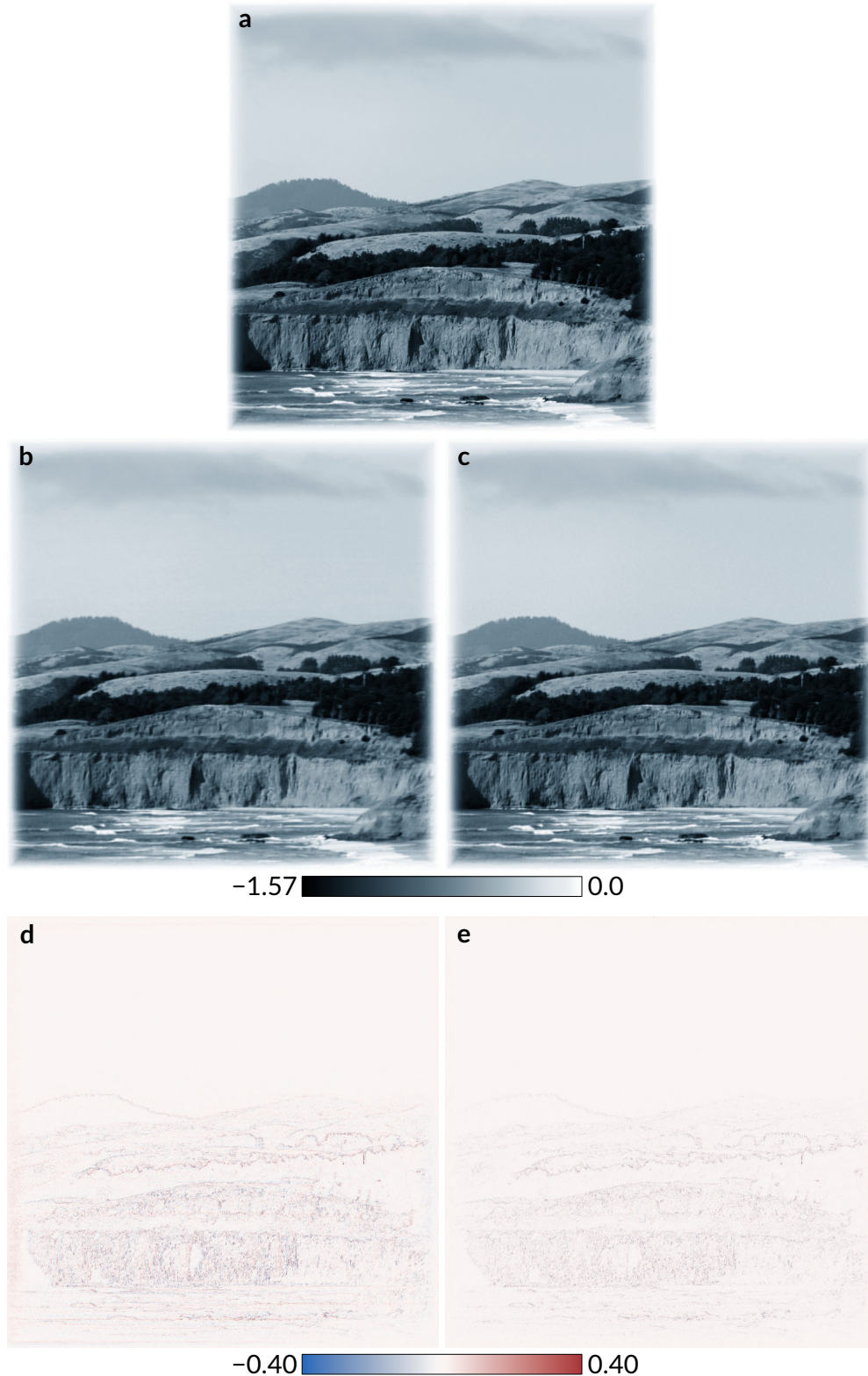


**Figure 5.8** Averaged reconstructions of the CXDI simulation. The empty padding around the sample is removed. The images **a-c** and **d,e** use the same scaling respectively. **a** Original. **b** Average of 50 standard DM reconstructions. **c** Average of 50 refractive DM reconstructions. Before the averaging, all reconstructions are aligned and all ambiguities removed. **d,e** Difference between the original phase shift and the respective averages. The calculated errors for the averages of the standard and refractive reconstruction are 516.1 and 270.5 respectively.

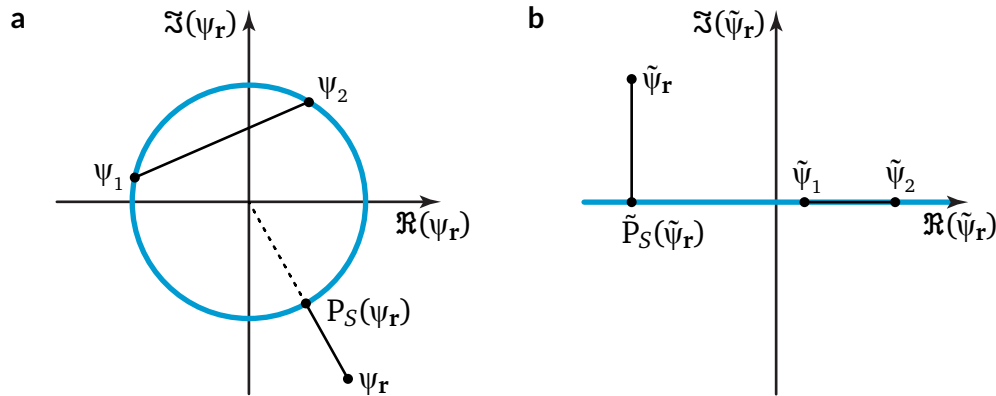


**Figure 5.9 Standard and refractive real-space projectors.** **a** In the standard projection, a point  $\psi_r$  is projected onto the closest point on the circle to enforce a pure phase object. The circle is a non-convex set, as the linear combination of two projections  $\psi_1$  and  $\psi_2$  is in general not on the circle. **b** The refractive projection projects a point  $\tilde{\psi}_r$  onto the closest point on a line parallel to the real axis. Here, the line is a convex set as a linear combination of two projections stays on the line. Adapted from [Mar07].

Similar to refractive ptychography, the refractive holography algorithm is able to directly reconstruct the phase shift of the sample without phase wrapping. Refractive coherent diffractive imaging (rCXDI), the refractive variant of CXDI, is adapted from the commonly-used difference-map (DM) algorithm. The derived refractive projectors,  $\tilde{P}_S$  and  $\tilde{P}_M$ , should generalize to other algorithms such as relaxed averaged alternating reflections (RAAR).

For rCXDI, the sample had no phase wraps and even in this relatively simple case, the refractive reconstruction was still reliably closer to the ground truth than the standard reconstruction. One probable reason for this is outlined in Figure 5.9, where in the refractive model the set of all phase objects forms a convex set. In contrast, this is generally not the case in the standard transmission model.

Refractive phase retrieval is an important development for X-ray microscopy as it requires no calculation of the complex argument or logarithm, which up to now was a necessary step for compound reconstruction schemes such as tomography or resonant scanning. Refractive phase retrieval is especially suited for strongly phase shifting samples with one or more phase wraps. In this case, refractive reconstruction algorithms can minimize the influence of phase singularities, which can occur as artefacts during the reconstruction.



## 6 Multibeam X-ray ptychography

Large, high-resolution ptychography scans are time-consuming and beamtime for experiments at synchrotron light sources is limited and scarce. Continuous fly-scans allow fast scanning of large field of views [Cla+14; Pel+14], but only by reducing the resolution, as the same number of available photons is divided over more diffraction patterns [HS17].

Multibeam X-ray ptychography allows to exploit hitherto unused photons to increase the field of view without reducing the resolution. By scanning the sample with multiple spatially separate probes, a larger area can be scanned in the same time. This technique was developed by Bevis *et al.* [Bev+18] and its applicability in the hard X-ray regime was demonstrated by Hirose *et al.* [Hir+20]. In both works, an experimental set-up similar to Figure 6.1 was used.

In this chapter we describe a novel multibeam scheme that is based on multiple independent focusing optics, which allows to use a larger fraction of the incoming flat beam. Section 6.1 discusses the multibeam reconstruction algorithm and Section 6.2 describes how 3D nanoprinting allows to manufacture multiple X-ray optics in close proximity. Then, Section 6.3 presents the ptychography results from multibeam experiments using two and six simultaneous beams.

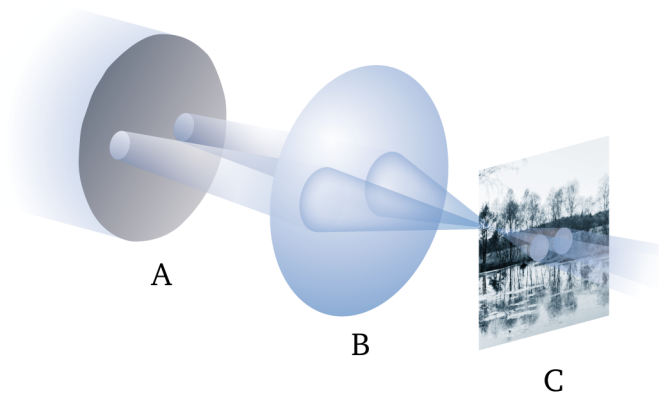


**Figure 6.1** Multibeam ptychography scheme. The pinhole array A is imaged by a lens B onto the sample C to create multiple separate probes. For X-rays, due to the small numerical aperture of X-ray optics, only short beam separations are possible with this scheme.

## 6.1 Multibeam algorithm

Many ptychography algorithms have been developed that reconstruct (partially) incoherent data [BCR14; OHG18; TM13]. They all use the high redundancy in ptychography measurements to describe the incoherence as an incoherent sum of individually coherent subcases. Some of these algorithms exploit incoherence as a feature to include more information in one scan. For example, the multiplex algorithm from Batey *et al.* uses polychromatic light to measure the response of the sample to different wavelengths in a single measurement.

The multibeam reconstruction algorithm is based on this multiplex algorithm, but instead of scanning different wavelengths, each individually coherent probe scans a different part of the sample. This allows to image a larger area without increasing the sample movement range. The derivation of the multibeam algorithm is similar to the derivation of standard ptychography in Section 3.1. In contrast to the standard ptychography set-up in Figure 3.1, the sample is here scanned by multiple probes. Each probe  $P_m$  is offset by a constant vector  $\mathbf{S}_m$  and at every scan position  $\mathbf{R}_j$ , each probe creates its own exit wavefront

$$\psi_{j,m,\mathbf{r}} = O_{\mathbf{r}} \cdot P_{m,\mathbf{r}-\mathbf{R}_j-\mathbf{S}_m}. \quad (6.1)$$

All the different wavefronts propagate to the detector

$$\Psi_{j,m,\mathbf{q}} = \mathcal{F}(\psi_{j,m}), \quad (6.2)$$

where each wavefront forms its own diffraction pattern. If each probe  $P_m$  is incoherent to every other probe, their wavefronts add up incoherently on the detector

$$I_{j,\mathbf{q}} = \sum_m |\Psi_{j,m,\mathbf{q}}|^2. \quad (6.3)$$

The reconstruction must disentangle the different contributions as there is no direct way to find out which photon originated from which probe. The update therefore enforces for each pixel  $\mathbf{q}$  that the sum  $I_{j,\mathbf{q}}$  of all contributions matches the measured photons  $n_{j,\mathbf{q}}$ . For this, the far-field update  $\Phi$  in Equation 3.10 is changed to

$$\Phi_{j,m,\mathbf{q}} := \left( 1 - \frac{\sqrt{n_{j,\mathbf{q}}}}{\sqrt{I_{j,\mathbf{q}}}} \right) \Psi_{j,m,\mathbf{q}}, \quad (6.4)$$

so that the denominator contains the sum of the wavefronts. Due to the large redundancy in ptychography, this can still converge to a solution. From the far-field update, the update for the probes follows directly from the ePIE update in Equation 3.16. As before, the probe update for subiteration  $l$  is determined by the current object

estimate  $O_l$  and  $\phi$ , the inverse Fourier transform of  $\Phi$ , yielding

$$P_{l+1,m,\mathbf{r}} = P_{l,m,\mathbf{r}} + \beta \frac{-\phi_{j,m,\mathbf{r}+\mathbf{R}_j+\mathbf{S}_m}}{\max |O_{l,\mathbf{r}+\mathbf{R}_j+\mathbf{S}_m}|^2} \cdot O_{l,\mathbf{r}+\mathbf{R}_j+\mathbf{S}_m}^*. \quad (6.5)$$

The object is updated with the changes from each wavefront  $\phi_m$ . All these changes are summed up and applied to the object. The object update is then given by

$$O_{l+1,\mathbf{r}} = O_{l,\mathbf{r}} + \alpha \sum_m \frac{-\phi_{j,m,\mathbf{r}}}{\max |P_{l,m,\mathbf{r}-\mathbf{R}_j-\mathbf{S}_m}|^2} \cdot P_{l,m,\mathbf{r}-\mathbf{R}_j-\mathbf{S}_m}^*. \quad (6.6)$$

The multibeam algorithm requires mutually incoherent beams. This is not necessarily the case in every experimental situation. If the probes are at least partially coherent, the beams can show interference effects on the detector. However, this interference between different beams can be suppressed. Without loss of generality we consider two mutually coherent probes  $P_1$  and  $P_2$ , separated by a distance  $\mathbf{S}$ . Behind the sample, each probe creates its own respective wavefront  $\psi_1$  and  $\psi_2$ . Due to the separation, the Fourier transform  $\Psi_2$  of the second wavefront gains a phase term of  $\exp(i\mathbf{S}\mathbf{q})$ . On the detector, the two wavefronts  $\Psi_1$  and  $\Psi_2$  overlap and interfere, resulting in a diffraction pattern

$$I_{\mathbf{q}} = |\Psi_{1,\mathbf{q}} + e^{i\mathbf{S}\mathbf{q}}\Psi_{2,\mathbf{q}}|^2 = |\Psi_{1,\mathbf{q}}|^2 + |\Psi_{2,\mathbf{q}}|^2 + 2\Re(e^{-i\mathbf{S}\mathbf{q}} \cdot \Psi_{1,\mathbf{q}} \cdot \Psi_{2,\mathbf{q}}^*). \quad (6.7)$$

The last term is the interference term and depends on the coherence between the two wavefronts. The product between the two wavefronts can be described by a  $\mathbf{q}$ -dependent modulus  $V_{\mathbf{q}}$  and phase  $\varphi_{\mathbf{q}}$

$$\Psi_{1,\mathbf{q}}\Psi_{2,\mathbf{q}}^* = V_{\mathbf{q}}e^{i\varphi_{\mathbf{q}}}. \quad (6.8)$$

Using  $V_{\mathbf{q}}$  and  $\varphi_{\mathbf{q}}$ , we can write the interference term in Equation 6.7 as

$$\Re(e^{-i\mathbf{S}\mathbf{q}}\Psi_{1,\mathbf{q}}\Psi_{2,\mathbf{q}}^*) = V_{\mathbf{q}}\cos(\varphi_{\mathbf{q}} - \mathbf{S}\mathbf{q}). \quad (6.9)$$

In the measurement, the signal in each detector pixel is proportional to the integral of the diffraction pattern over the area of the pixel. This is only strictly true if the pixel response is uniform throughout the pixel area. For single photon counting pixel detectors, this is a good approximation [Zam+18]. If the diffraction patterns are well sampled,  $V$  and  $\varphi$  can be assumed as constant for each pixel. In a single pixel of size  $p$ , the signal  $U$  from the interference term is then the integral

$$U = \iint_{p \times p} V\cos(\varphi - \mathbf{S}\mathbf{q}) d^2q \quad (6.10)$$

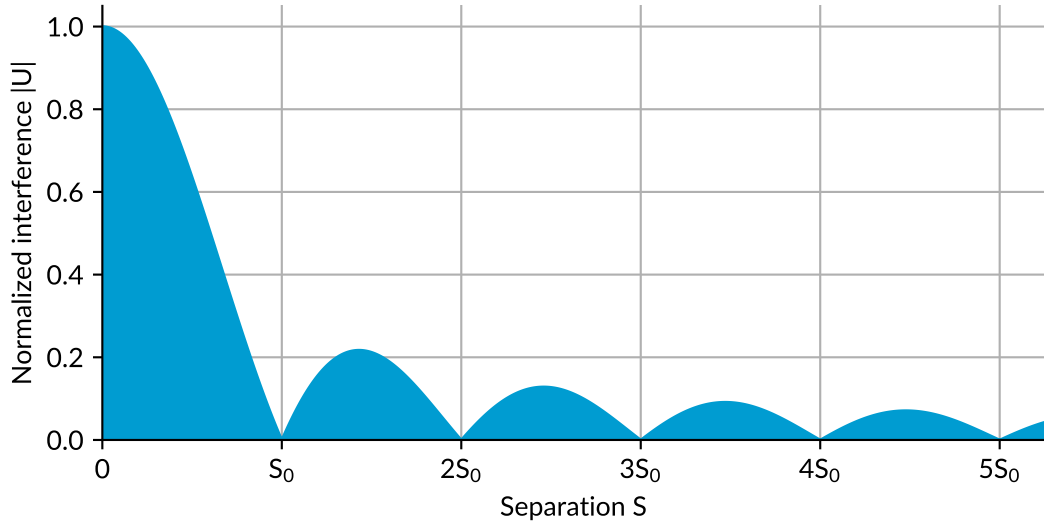


**Figure 6.2 Multibeam interference.** Simulation of  $U$ , the interference signal from a detector pixel, for purely horizontal probe separations  $\mathbf{S} = (S, 0)$ . The normalized results for all possible values of  $\varphi$  are shown, forming the shaded area. The values are enveloped by a sinc function which is zero for all multiples of the characteristic distance  $S_0$ .

over the area  $p \times p$  of the pixel. The strength of  $U$  oscillates depending on the probe separation with a characteristic oscillation period  $S_0$ , see Figure 6.2. This means the different probes can be treated as incoherent if they are integer multiples of  $S_0$  apart. In paraxial approximation, the characteristic distance is given by

$$S_0 = \frac{\lambda d}{p}, \quad (6.11)$$

with the X-ray wavelength  $\lambda$  and the sample–detector distance  $d$ . This result is identical to Equation 3.18, the field of view in the reconstructed probe. This means the different probes can be treated as incoherent if they are multiples of the field of view apart.

## 6.2 X-ray lenses by additive 3D nano-manufacturing

The previous works on multibeam ptychography by Bevis *et al.* [Bev+18] and Hirose *et al.* [Hir+20] used only a single focusing optic to create multiple beams. For X-rays, it would be advantageous to use multiple focusing optics in parallel so that a larger fraction of the incoming beam can be harnessed for ptychography. However, it is already technologically challenging to manufacture high-quality single beam X-ray optics, as the manufacturing of complex three-dimensional objects with submicrometer resolution requires high-precision techniques and instruments. Mechanic approaches are capable of producing smooth surfaces with high-precision for KB-mirrors and

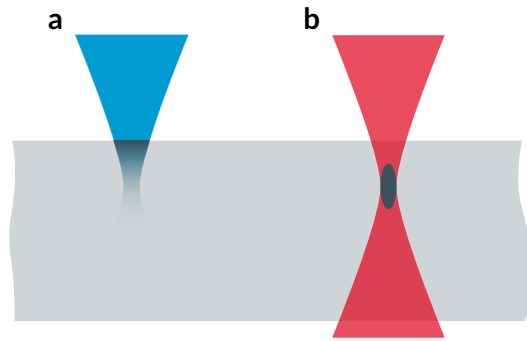


**Figure 6.3 Two-photon lithography.** The liquid resist (light grey) is exposed by two beams with different wavelengths. The light initiates a reaction in the resist and it hardens where it was exposed. **a** The ultraviolet laser is absorbed in the resist and starts polymerization (dark gray). **b** The resist is transparent for a near-infrared laser, causing no polymerization. Only in the focus is the intensity high enough for non-linear effects like two-photon absorption to occur. As this takes place only in a small and confined volume, it can be used for highly selective exposure of the resist as is needed for 3D printing.

CRLs, but these techniques have difficulties to create more complex structures such as strong curvatures or cavities. Alternatively, additive 3D manufacturing, also called 3D printing, offers more freedom in the structure design. In a bottom-up approach, the structure is assembled by printing one volume element (voxel) at a time.

Multiphoton lithography allows rapid 3D manufacturing at the nanoscale. In optical lithography, a resist changes chemically under light exposure and becomes solid or resistant/vulnerable to chemical etching. This selective etching is the basis of microelectronic and integrated circuit production. However, the resist is exposed and developed along the entire path of the light, allowing only the construction of 2D or very simple 3D structures through stereoscopic approaches. Figure 6.3a shows how an ultraviolet laser beam exposes and develops the resist. As the beam gets absorbed in the resist, how much and how quickly the resist is developed changes with the depth.

Multiphoton lithography uses liquid resists that are transparent to near-infrared light (around 800 nm) and only harden under UV light (around 400 nm). If the intensity of a near-infrared (pulsed) laser is high enough like in Figure 6.3b, non-linear processes such as two-photon absorption can occur in the focus region and cross the threshold for the development of the resist. As this depends strongly on the flux density, the size of the region can be changed by tuning the laser intensity. Typical sizes are in the range of a few hundred nanometer. By scanning either the laser or the resist in three spatial dimensions, free-shape structures can be created with submicrometer resolution. Besides the high-resolution of the "print", the surfaces are also smooth, with a surface roughness below 20 nm [Dur+18]. After the printing, the hardened

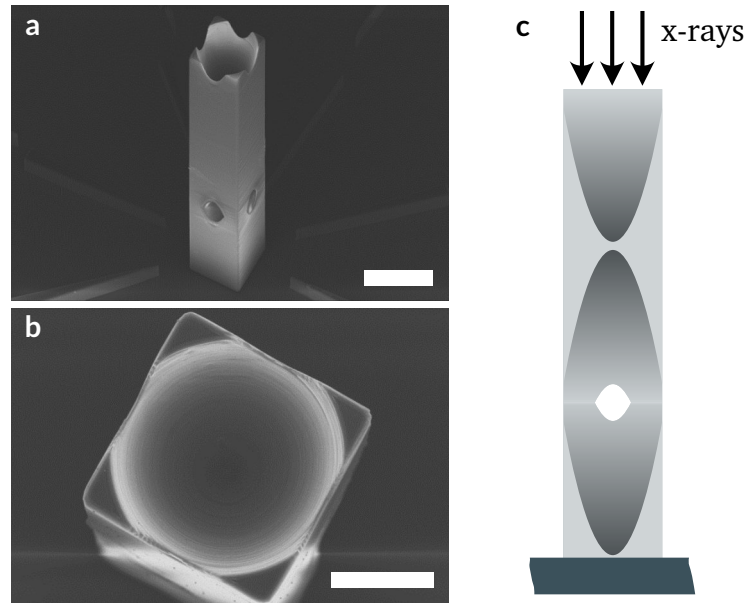


**Figure 6.4 3D printed lens tower.** **a** SEM image of the lens tower, showing the open top and the openings at the bottom to empty the cavity from undeveloped, liquid resist. The scale bar represents 50  $\mu\text{m}$ . **b** SEM view from the top of the lens tower. The parabola partially extends beyond the tower, leaving openings. The scale bar represents 10  $\mu\text{m}$ . **c** Schematic cut through the lens tower, highlighting the three parabolic surfaces and the openings in the bottom half to drain the undeveloped resist.

resist structure can be removed from the still liquid resist. For this, the structure should contain no closed voids to allow complete draining of the undeveloped, liquid resist.

Due to the small features and smooth surfaces, multiphoton lithography offers a cheap way to manufacture tailor-made X-ray lenses. The polymer is relatively radiation-hard and only starts to deform and shrink after the absorption of a few megagray [Bar+19]. Petrov *et al.* [Pet+17] were the first to fabricate x-ray lenses by two-photon lithography. Their lens design however could only achieve a focus size of 5  $\mu\text{m}$  and their optical axis is parallel to the mounting plane, allowing multibeams only in one direction. Mikhail Lyubomirskiy devised an improved lens tower design [Lyu+19] with an optical axis perpendicular to the surface that is capable of sub-micrometer focusing, see Figure 6.4. By printing multiple towers, multiple parallel beams can be readily produced in arbitrary arrangements.

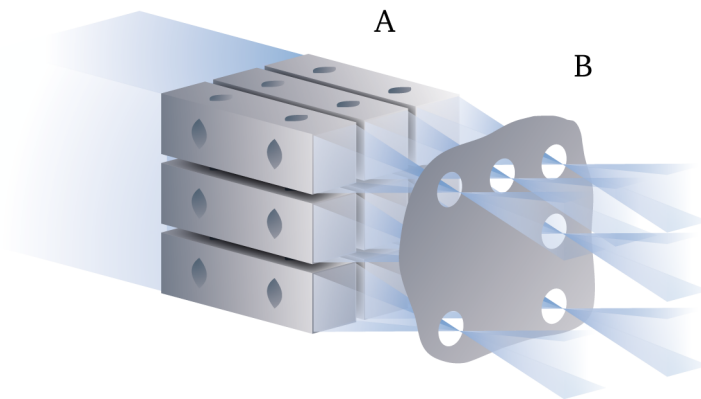


**Figure 6.5 Multibeam set-up.** Each lens tower in the lens array A creates its own beam. The tailor-made pinhole array B reduces scattering and lets up to six beams pass. Different numbers and arrangements of multibeams can be created by selectively illuminating only certain lens towers with different slit openings upstream of the lens array.

### 6.3 Multibeam experiments

In this section, two different multibeam ptychography experiments are demonstrated, the first one using two and the second one using six beams. The experiments were performed at the microprobe endstation of the P06 beamline at PETRA III in Hamburg. The multibeams for both experiments were created with the same 3D printed lens array. The lens array consists of  $10 \times 10$  lens towers in a  $47 \mu\text{m}$  raster grid. Each lens tower has a square foot print of  $45 \mu\text{m} \times 45 \mu\text{m}$  and a height of  $600 \mu\text{m}$ , leaving a gap of  $2 \mu\text{m}$  between adjacent towers. Each tower contains four parabolic surfaces, each with an apex curvature  $R$  of  $2.5 \mu\text{m}$ . The lens array was designed by Mikhail Lyubomirskiy and printed by Frieder Koch at the Paul Scherrer Institute (PSI) in Switzerland using a Nanoscribe Photonic Professional GT and Nanoscribe's IP-S resist. For 7 keV X-rays, the resist has a refractive index decrement  $\delta$  of  $5.54 \times 10^{-6}$ , giving a focal length of 113 mm and a diffraction-limited spot size of 335 nm.

For the experiments, the lens array was placed on a PI F-206 hexapod. Two different Siemens star resolution test charts from NTT-AT, both model ATN/XRESO-50HC, were used as samples for the two experiments. An intact Siemens star for the 2-beam experiment and a damaged one for the 6-beam experiment. The Siemens stars are made of 500 nm thick Tantalum and the smallest structures have a size of 50 nm. In both experiments, the sample was placed 20 mm downstream of the focal plane, where each of the probes had expanded to a size of  $7.5 \mu\text{m}$ . The photon energy was set to 7 keV and the diffraction patterns were recorded with an in-vacuum Eiger X 4M detector from Dectris [Joh+14]. The Eiger detector was situated inside the nanoprobe endstation, 8050 mm downstream of the sample, at the end of the evacuated flight tube [Sch+19a]. With these parameters, the characteristic probe

**Table 6.1** Parameters of the 2-beam experiment.

Parameters	2-Beam
Energy	7 keV
Flux	$4.3 \times 10^7$ ph/s
Exposure	1 s
Scan size	$31 \times 61$
Step size	$1.00 \pm 0.25$ $\mu\text{m}$
Probe diameter	8 $\mu\text{m}$
Number of probes	2
Detector distance	8050 mm
Detector pixel	75 $\mu\text{m} \times 75$ $\mu\text{m}$
Image size	$512 \times 512$ pixels
Pixel size (rec.)	37.1 nm

separation is  $S_0 = 19$   $\mu\text{m}$  and the distance between the lens towers is  $2.5S_0$ . Ideally, the probe separation would be  $2S_0$  or  $3S_0$  to fully suppress the interference between the beams, but due to a calculation error this was only realised after the beamtime. Fortunately, at this probe separation, the interference term has less than 15 % of its maximum value, compare Figure 6.2. Due to this, the reconstructions are only weakly affected. Figure 6.5 illustrates the set-up for the multibeam optics. To suppress scattering from the lenses, a tailor-made pinhole array was placed between the lenses and the sample. The pinhole array was made from 100  $\mu\text{m}$  thick platinum foil into which six 30  $\mu\text{m}$  holes were drilled by laser ablation. The holes are spaced 47  $\mu\text{m}$  apart. The geometry of the hole arrangement allows different probe configurations to be selected by utilizing the pair of horizontal and vertical slits upstream of the lens array.

### 6.3.1 2-Beam experiment

For the first experiment, the slits were closed to only illuminate two vertically neighbouring lenses. The Siemens star was scanned in 1  $\mu\text{m}$  steps in a grid of  $31 \times 61 = 1891$  positions ( $h \times v$ ) with 1 s exposure per point. To avoid scan grid artefacts [Thi+09], jitter was added to each scan point in the form of random horizontal and vertical offsets of up to  $\pm 0.25$   $\mu\text{m}$ . The scan areas of the two probes overlap on a  $30$   $\mu\text{m} \times 13$   $\mu\text{m}$  ( $h \times v$ ) wide area. All scan parameters are summarized in Table 6.1.

For the reconstruction, the Eiger images were cropped to  $512 \times 512$  pixels centered around the beam position, resulting in a pixel size of 37.1 nm in the reconstruction. The scan was reconstructed in two ways: first with the standard single beam algorithms and then a second time with the corresponding multi-beam variants. The

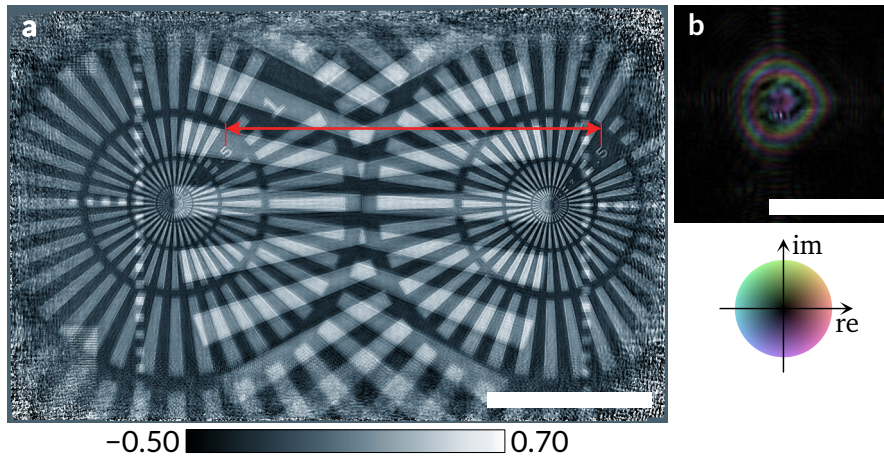


**Figure 6.6 2-Beam ePIE reconstruction.** **a** Reconstructed phase shift of the Siemens star. The image is rotated  $90^\circ$  clockwise for easier visualization. As ePIE cannot separate the two probes, the reconstructed object is a mix of the areas scanned by each probe. By measuring the distance between duplicated features, the separation distance between the probes can be accurately estimated. Here, the  $0.5 \mu\text{m}$  markers are  $45.5 \mu\text{m}$  apart, slightly deviating from the expected distance. The scale bar in the bottom right corner represents  $20 \mu\text{m}$ . **b** Reconstructed probe in complex colouring. The scale bar represents  $10 \mu\text{m}$ .

first reconstruction in Figure 6.6 was run for 500 iterations with the single beam ePIE algorithm and afterwards refined for a further 500 iterations with the parallel algorithm described in Section 3.2. Because the scanning stage could not move with the necessary precision, the positions were refined during the reconstruction with the brute-force algorithm described in Subsection 3.5.2. These corrected positions were then used in the second, multibeam reconstruction. Besides improving the scan positions, the single beam reconstruction was also used to provide a more accurate estimate of the distance between the probes by measuring the separation of duplicated features, for example the resolution markings. Here, the measured distance is  $45.5 \mu\text{m}$ , less than the design value of  $47 \mu\text{m}$ . This could result from small manufacturing errors or a slight bending of the free-standing lens towers.

With the refined scan positions and probe separation, the scan was reconstructed anew, this time using the multibeam algorithm for the first 500 iterations, before switching to the parallel multibeam algorithm for a further 500 iterations. The results are shown in Figure 6.7. The two probes in Figure 6.7a and b are well reconstructed, they are similar but not identical. However, as the lens towers have a four-fold symmetry, the same would be expected from the probes. This is not the case and the probes are slightly astigmatic, the vertical and horizontal focal length differ by 5 mm over the expected focal length of 113 mm. Most probably, the towers are tilted due to the neighbouring towers, as a single, individually printed tower showed no astigmatism [Lyu+19]. In Figure 6.7c, the full diameter of the Siemens star is reconstructed, from

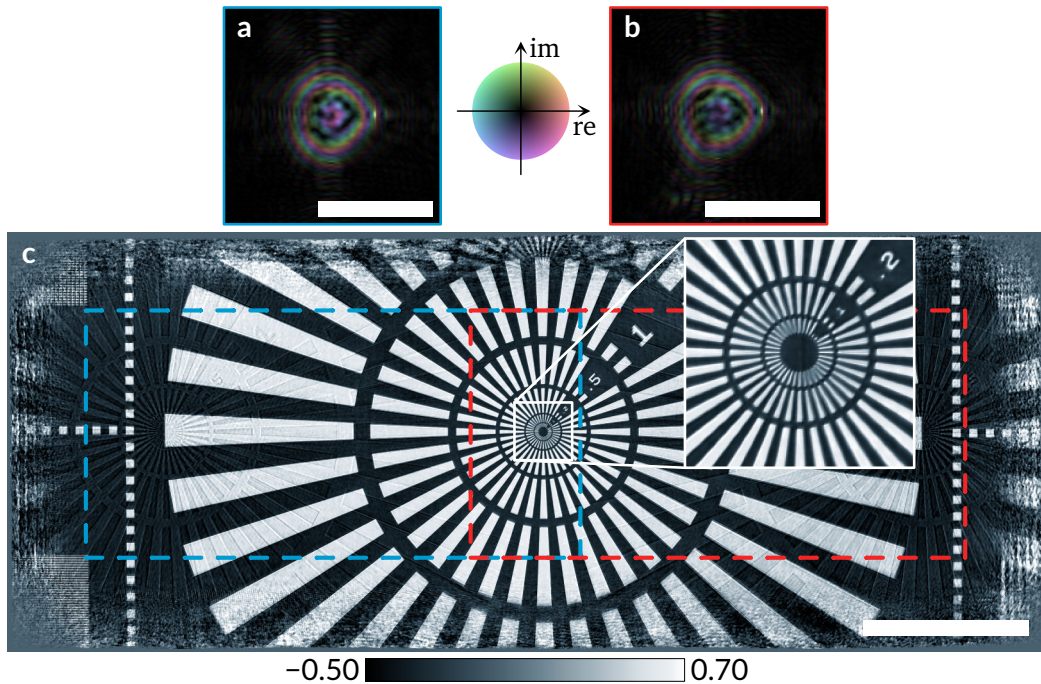


**Figure 6.7 2-Beam multibeam reconstruction.** **a,b** Reconstructed probes in complex colouring. The colour of the frame corresponds to the scan area. The scale bars represent  $10\ \mu\text{m}$ . **c** Reconstructed phase shift of the Siemens star. The image is rotated  $90^\circ$  clockwise for easier visualization. The blue and red dashed rectangle indicate the areas scanned by the two probes. The white square shows a zoom-in on the central region with the  $50\ \text{nm}$  structures. The scale bar in the bottom right represents  $20\ \mu\text{m}$ .

the outermost  $4\ \mu\text{m}$  structures down to the  $50\ \text{nm}$  spokes in the centre. The total area scanned by both probes measures  $105.5\ \mu\text{m} \times 30\ \mu\text{m}$ , while the physically scanned area was only  $60\ \mu\text{m} \times 30\ \mu\text{m}$ . This corresponds to a speed-up of 1.8 compared to a single probe scanning the same field of view. The reconstruction of the central area is free from artefacts as it was scanned by both probes. Away from the overlap area, where only one probe scanned the sample, copies of the centre of the Siemens star appear as artefacts. This has two reasons, the first is the incomplete suppression of the interference between the two beams on the detector. Accurately, the interference should be suppressed by tuning the experimental parameters as explained at the end of Section 6.1. The second reason is the similarity between the two probes. Especially in the relatively flat sample areas near the left and right edge of the reconstruction, the algorithm cannot determine which probe generated which speckle in the diffraction patterns.

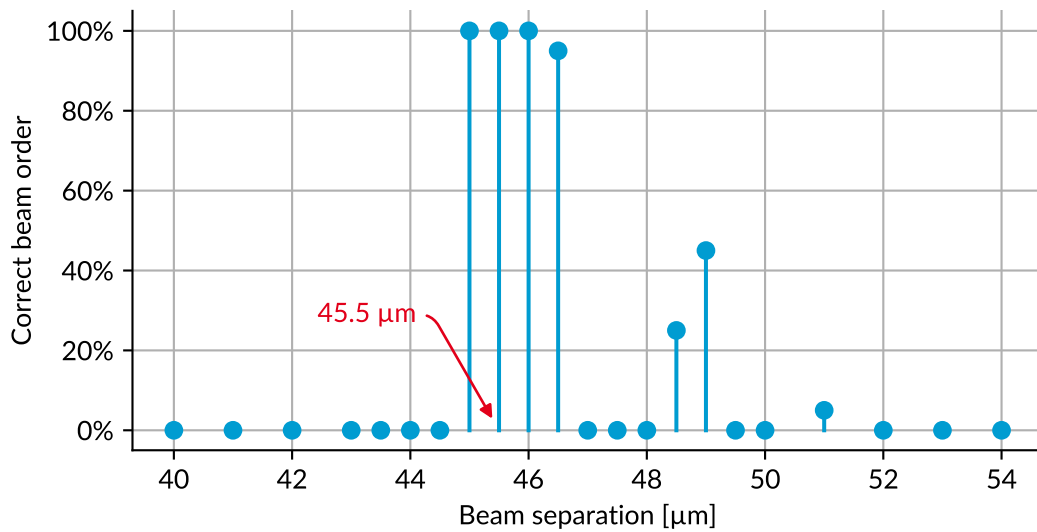


**Figure 6.8 Reconstruction sensitivity to assumed beam separation.** If the beam separation that is used in the reconstruction is too far away from the true value, the reconstruction fails to align the two object parts. In this case, the algorithm can not determine which probe is which. The plot shows the percentage of reconstructions with the correct probe order for a certain assumed beam separation.



**Figure 6.9 Wrong beam distance.** Reconstructed object after 50 iterations with an assumed beam separation of  $47\ \mu\text{m}$ . Each probe faithfully reconstructs one part of the object. However, due to the wrong order of the probes, the object is reconstructed inside out.

### 6.3.2 Sensitivity to incorrect probe separation

For the 2-beam experiment, the measured probe separation differs by  $1.5\ \mu\text{m}$  from the design value. To analyse how sensitive the multibeam algorithm is to incorrect probe separations, the scan was reconstructed assuming different separations from  $40\ \mu\text{m}$  to  $54\ \mu\text{m}$ . Each reconstruction was run for 50 iterations and was repeated 20 times to minimize random influences from the shuffling of the diffraction patterns. Ideally, the algorithm should be able to shift the probes inside their field of view to correct for wrong beam separations within a certain range. In the 2-beam scan for example, the field of view of the probes is  $19\ \mu\text{m}$ , large enough to shift the probes by several micrometer in each direction, compare Figure 6.7a,b. However, the results in Figure 6.8 show that the multibeam algorithm can shift the probes only inside a small range of  $2\ \mu\text{m}$  around the correct beam separation. For larger errors, the probes are reconstructed in the wrong order, turning the object inside-out. This can be seen

exemplarily in Figure 6.9.

For nearly all separations, the reconstructed probes are either always in the correct order or always in the wrong order. Only for a few separations are some of the reconstructions correct and some wrong. Still, only in the plateau around  $46\ \mu\text{m}$  are the two scan areas accurately aligned like in Figure 6.7.

All these results highlight the importance of accurately knowing the beam separation. Because the reconstruction algorithm can shift the probes only a small distance, the beam separation in this experiment must be correct within 2% of the true value. To determine the separation for a new multibeam array, different methods are possible. For two beams and simple objects, a test scan can be reconstructed with the single beam ePIE algorithm. The distance between duplicated object features can then serve as a close guess for the beam separation. More complex multibeam set-ups can be characterized through an X-ray fluorescence scan of a single isolated particle using all beams or by repeating a ptychographic scan with each beam individually and then stitching the different scan areas to find the correct beam separation. Any multibeam array only needs to be characterized initially. In future experiments, the refined beam separations can be directly used.

### 6.3.3 6-Beam experiment

In the second experiment the slits were opened to create six simultaneous beams in the arrangement shown in Figure 6.5. For the ptychographic measurement, the damaged Siemens star was scanned with  $1\ \mu\text{m}$  steps in a  $121 \times 121$  raster grid, where each scan position was randomly offset from the ideal grid by up to  $\pm 0.25\ \mu\text{m}$ . Due to the large scan range, each of the six probes illuminates the centre of the Siemens star at some point. At each scan point the Eiger detector was exposed for 0.3 s. All scan parameters are summarized in Table 6.2.

For the reconstruction, the diffraction patterns were cropped around the central beam position to  $512 \times 512$  pixels. The distances between the beams might also differ in the 6-beam experiment from the design values. Therefore, in the reconstruction, the probes were initialized with a probe separation of  $46\ \mu\text{m}$  and  $92\ \mu\text{m}$ , based on a compromise between the experience from the previous Subsection 6.3.2 and the original design. For the first 500 iterations, the data was reconstructed with sPIE (see Section 3.3), adapted for multibeams, using a  $2 \times 2$  upsampling. Then, the reconstruction was refined for a further 500 iterations using the parallel variant. As the scanning stage could not achieve the necessary precision, the faulty scan positions were refined with the position refinement described in Subsection 3.5.2. On average, the refinement changed the positions by 400 nm.

The reconstructed probes and object are shown in Figures 6.10 and 6.11, respectively. The six probes are nearly identical due to the high reproducibility of 3D nano printing.

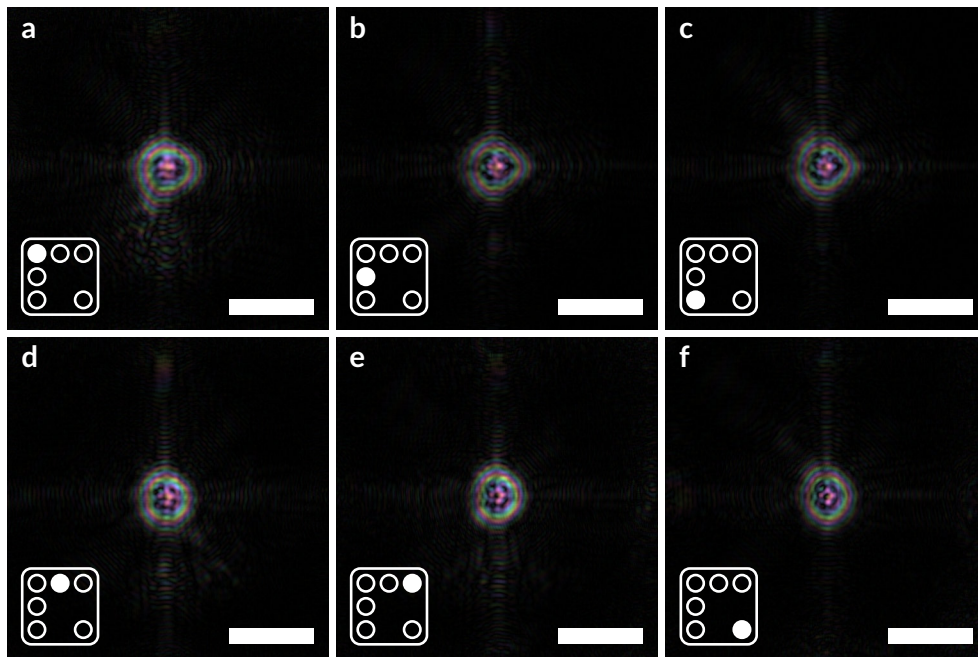


**Figure 6.10** 6-Beam reconstruction. a-f Reconstructed probes in complex colouring. The position of the probe in the multibeam is shown in the lower left corner of each probe. The scale bars represent 5  $\mu\text{m}$ .

**Table 6.2** Parameters of the 6-beam experiment.

Parameters	6-Beam
Energy	7 keV
Flux	$1.9 \times 10^8$ ph/s
Exposure	0.3 s
Scan size	$121 \times 121$
Step size	$1.00 \pm 0.25$ $\mu\text{m}$
Probe diameter	8 $\mu\text{m}$
Number of probes	6
Detector distance	8050 mm
Detector pixel	75 $\mu\text{m} \times 75$ $\mu\text{m}$
Image size	$512 \times 512$ pixels
Pixel size (rec.)	37.1 nm

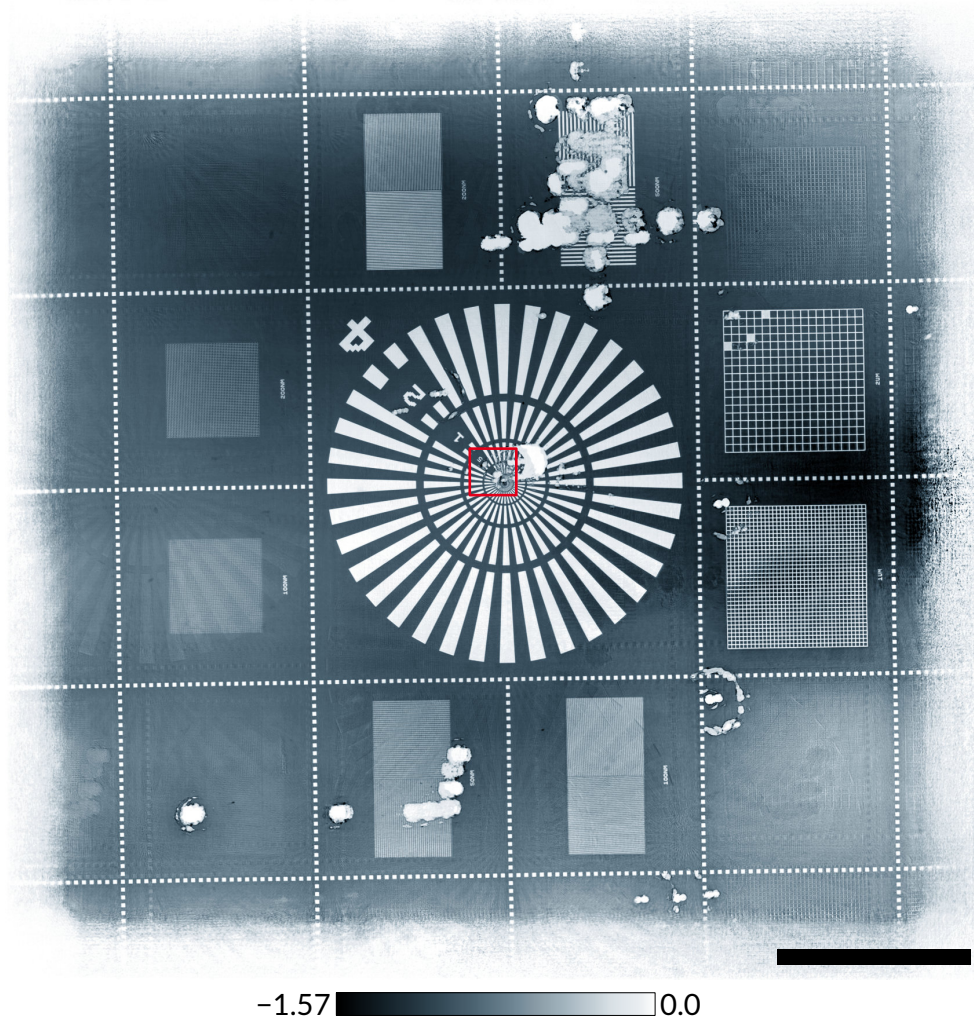


**Figure 6.11 6-Beam reconstruction.** Reconstructed phase shift of the damaged Siemens star. The reconstructed area measures  $250\ \mu\text{m} \times 250\ \mu\text{m}$  in  $6750 \times 6750$  pixels. The region at the centre of the Siemens star, outlined by the red square, is shown enlarged in Figure 6.12. The scale bar represents  $50\ \mu\text{m}$ .

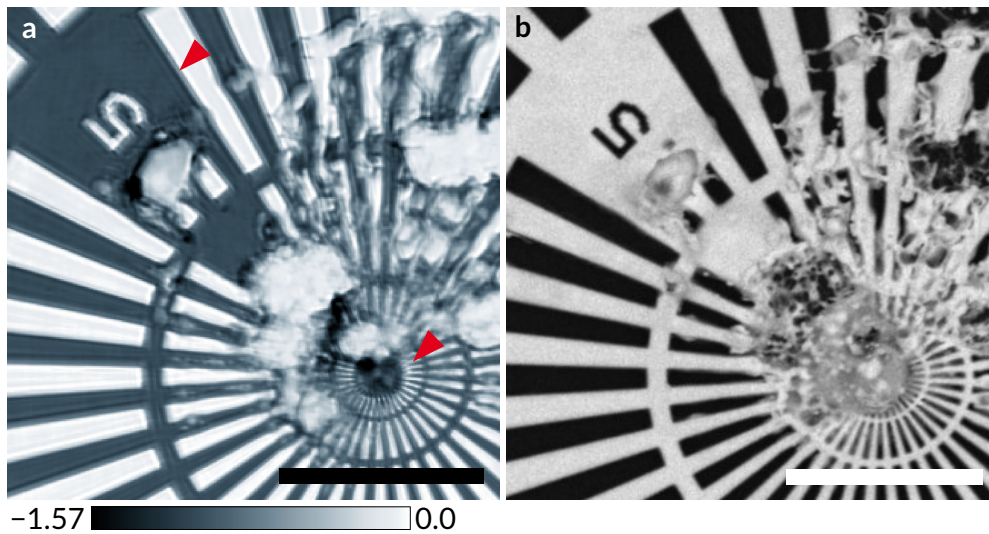


**Figure 6.12** Detail from the 6-beam reconstruction. **a** Enlarged view of the central area of the Siemens star. The red arrows mark different resolution estimates. The lower one points to the reconstructed 50 nm spokes in the centre. The top arrow points to the edge of the 500 nm spokes, which have an edge spread of 200 nm **b** Scanning electron micrograph of the same area. The scale bars represent 5  $\mu\text{m}$ .

The reconstructed object shows only weak multibeam artefacts, underlining that the probes are correctly reconstructed. Only on the left side and in the corners, faint replicas of other object parts are visible. The white spots in the object are the areas that were destroyed in a previous experiment by an X-ray free-electron laser (XFEL) beam. The centre of the Siemens star in Figure 6.12 closely matches the SEM image of the same area, with details as small as the 50 nm spokes well resolved. However, the overall resolution of the ptychography reconstruction is lower, as the sharp edges of large scale features are blurred for up to 200 nm. Different resolutions in different parts of the reconstructed object are not unusual in ptychography and depend on the local scattering of each feature, as demonstrated by Schropp *et al.* [Sch+12].

For the 6-beam experiment, the reconstructed area is more than 3.1 times larger than the real scan area of the sample. The resolution in the reconstruction varies between different features and ranges from 50 nm to 200 nm. One problem during the reconstruction is the high similarity between the six probes. The reconstruction algorithm requires many iterations to find the correct probe order, leading to multibeam artefacts in the form of duplicated object features.

## 6.4 Conclusion

In this chapter, a new scheme for multibeam X-ray ptychography was developed. This scheme was tested and proven to be viable at the P06 beamline with a two and a six beam experiment. Using multiple beams allows to scan large areas faster, the two experiments achieved a speed-up of 1.8 and 3.1, respectively. In both experiments, challenges arose from the high similarity of the different probes, making it difficult for the algorithm to separate the contributions from each probe. This can be improved by making the probes as unique as possible. For example, with orbital angular momentum (OAM), the probes become mutually orthogonal. These so called vortex beams can be easily created with refractive phase plates [Sei+19]. In combination with 3D printing, the necessary phase plates could be directly integrated into each lens tower, making additional alignment unnecessary.

Problematic in the multibeam experiments were the inaccurate scanning stages, requiring position corrections of several hundred nanometres. This is not an intrinsic problem of multibeam ptychography, but the double complication of finding the correct positions and finding the contributions of each probe slows down the reconstruction.

## 7 Conclusion and Outlook

This thesis has studied two methods to advance quantitative X-ray phase microscopy. The first is refractive phase retrieval, which allows ptychography and similar phase retrieval techniques to directly reconstruct the projected complex refractive index of the sample. In conventional phase retrieval, the algorithms recover only the complex transmission of the sample and due to phase wrapping the phase shift is known only modulo  $2\pi$ . Phase wrapping creates phase jumps, which can be removed with phase unwrapping, but noise in the reconstruction can make this difficult or even impossible. The idea to directly reconstruct the projected refractive index was first presented by Chowdhury *et al.* [Cho+19] for Fourier ptychography. The projected refractive index is not limited to a specific range and large phase shifts can be reconstructed without phase jumps or phase wrapping. Refractive reconstruction algorithms are especially suited for large samples that shift the phase by more than  $2\pi$  and can prove difficult to reconstruct with transmission models [Sto+15].

In this work, the idea of refractive reconstructions was extended to other phase retrieval techniques by developing refractive algorithms for ptychography (Section 4.1), for inline holography (Section 5.1) and for coherent diffractive imaging (Section 5.2). Ordinarily, these phase retrieval techniques describe the interaction between the sample and the X-rays with a transmission model. For the new refractive algorithms, the transmission model is changed to a complex exponential with the projected refractive index in the exponent. Setting out from this exchange, new refractive reconstruction algorithms were derived for all three techniques.

In all three cases, the performance of the new refractive algorithm was successfully verified using simulated data. For ptychography, the outstanding reconstruction quality of the refractive model was also demonstrated on two experimental datasets. The micrometeorite sample in Section 4.4 highlights in particular the benefits for large samples. With a strong phase shift of up to 15 rad, the micrometeorite is challenging for the conventional ptychography algorithm, leading to phase vortex artefacts in the reconstruction. In contrast, refractive ptychography reconstructs the micrometeorite faithfully without vortex artefacts. After alignment and removal of a phase ramp, the refractive reconstruction can be used directly in tomography. Because refractive ptychography reconstructs the projected refractive index, no additional calculations using the complex logarithm are required. This makes refractive ptychography ideally suited for combined ptycho-tomography [Gür17; Kah+19], as it requires no conversion

for the tomographic part.

Direct access to the real and imaginary part of the refractive index is also beneficial for spectro-ptychography, where multiple scans at different photon energies are combined to distinguish different elements [Hop+13]. For the combined spectro-ptychography algorithm from Hirose *et al.* [Hir+17], the real and imaginary part are calculated at every iteration. With a refractive reconstruction model, this would no longer be necessary and the technique would also be applicable for thicker samples with phase shifts of more than  $2\pi$ .

The second technique, refractive holography, is equally well suited for strongly scattering samples as refractive ptychography. In the simulated experiment, polystyrene spheres with a maximum phase shift of more than 11 rad were modelled. These spheres are challenging for the conventional holography algorithm, which reconstructs them with phase wraps and vortex artefacts. The novel refractive holography algorithm avoids all of these problems and reconstructs the phase of the sample without jumps or artefacts. Again, the refractive algorithm is better suited to cope with these challenging samples with strong phase shifts.

For the third phase retrieval technique, refractive coherent diffractive imaging, only a weakly scattering sample was simulated, with a maximum phase shift of  $\pi/2$ . Even for this small sample with no phase wrapping, the refractive reconstruction was reliably closer to the ground truth than the conventional reconstruction. In repeated reconstructions with different initial guesses, the refractive reconstructions depended less on the starting values and were more consistent. In CXDI, the average of multiple reconstructions is often better than each individual reconstruction. For the simulation, the average of the conventional reconstructions improves the quality to a level similar to a single refractive reconstruction. Strikingly, the average of the refractive reconstructions is better than any single reconstruction from either algorithm by a big margin. The only remaining errors are due to photon-noise, which limits the resolution of fine-scale features.

All refractive experiments in this work, simulated or measured, could be described with a thin, single-scatter model. If the effects of multiple scattering by the sample cannot be neglected, the algorithms must be extended to include multi-slice approaches [MHR12]. This expansion, in combination with the higher coherent flux from ultralow-emission sources [Rai16; Sch+19b; Tav+18], will make it feasible to image millimetre-sized objects down to nanoscopic details.

Beyond the algorithmic developments in the first part, the second focus of this work was X-ray multibeam ptychography, a technique that allows fast scanning of large samples. In the first demonstration of this technique by Hirose *et al.* [Hir+20], the multibeams were created through the demagnified imaging of a group of pinholes onto the sample. Due to the small numerical aperture of X-ray optics, this method achieves only small beam separations of a few micrometres. In this work, a novel way

to create X-ray multibeams was developed, using 3D-printed refractive X-ray lenses. A lens array with a separation of  $47\ \mu\text{m}$  between each lens was printed using two-photon lithography, a technique that can print millimetre-sized objects with sub-micrometre precision.

The performance of the lens array was successfully tested for two and six beams. For the simplest multibeam case, the two beam experiment, the sensitivity of the reconstruction on the correct beam separation was studied, as the real value can differ from the design value. For a successful reconstruction of the Siemens star sample, the beam separation can deviate at most  $1\ \mu\text{m}$  from the correct value, requiring a precision of 2%. Due to the high repeatability of the printing process, all lenses, and consequently all beams, are nearly identical. This similarity between the different beams and probes is challenging for the reconstruction, as an incorrect probe separation gives rise to artefacts. These artefacts occur predominantly in flat regions of the sample, which diffract only weakly. Nevertheless, details as small as 50 nm could be faithfully reconstructed in both experiments.

With regards to the main advantage of multibeam ptychography, the faster scanning speed, both experiments fulfilled the expectations. Compared to a single beam scan of the same area, the two beam experiment achieved a speed-up of 1.8 and the six beam experiment achieved an even higher speed-up of 3.1. Ideally, the speed-up can be as high as the number of beams. In both experiments, the scan areas of the individual beams overlapped, which reduced the speed-up but was necessary to ensure a stable reconstruction.

For future experiments, the probes should be more diverse by making each probe unique. One way to maximize the uniqueness is to make the probes mutually orthogonal, for example by adding a different topological charge to each probe [Sei+19]. The phase plates for the topological charges can be included directly into the lens towers during the printing, avoiding any additional alignment. Preliminary tests were promising and indicate fewer multibeam artefacts and a faster disentanglement of the probes in the reconstruction.



# A Appendix

## A.1 Wirtinger derivatives

Wirtinger derivatives were originally defined by Wirtinger [Wir27]. This short overview is based on Remmert & Schumacher [RS13], which contains more details and provides proofs to the statements given here. The Wirtinger derivatives for  $C^1$ -differentiable functions in the complex plane  $\mathbb{C} = \mathbb{R}^2 = \{(x, y) | x, y \in \mathbb{R}\}$  are defined as

$$\frac{\partial}{\partial z} := \frac{1}{2} \left( \frac{\partial}{\partial x} - i \frac{\partial}{\partial y} \right), \quad (\text{A.1})$$

$$\frac{\partial}{\partial z^*} := \frac{1}{2} \left( \frac{\partial}{\partial x} + i \frac{\partial}{\partial y} \right). \quad (\text{A.2})$$

These derivatives treat a complex variable  $z$  and its conjugated variable  $z^*$  as independent. This can be exemplarily seen for the magnitude function

$$\frac{\partial}{\partial z} |z|^2 = \frac{\partial}{\partial z} z z^* = \underbrace{\frac{\partial z}{\partial z}}_{=1} z^* + \underbrace{\frac{\partial z^*}{\partial z}}_{=0} z = z^*. \quad (\text{A.3})$$

This result can be verified using the definition of the Wirtinger derivatives

$$\frac{\partial}{\partial z} |z|^2 = \frac{1}{2} \left( \frac{\partial}{\partial x} - i \frac{\partial}{\partial y} \right) (x^2 + y^2) = \frac{1}{2} (2x - 2iy) = z^*. \quad (\text{A.4})$$

It can easily be proven that Wirtinger derivatives share many properties with the standard derivatives. Let  $f = f(z, z^*)$  and  $g = g(z, z^*)$  be two differentiable functions in the complex plane. Then the following statements are true

1. Linearity

$$\frac{\partial}{\partial z} (\alpha f + g) = \alpha \frac{\partial f}{\partial z} + \frac{\partial g}{\partial z} \quad (\text{A.5})$$

2. Product rule

$$\frac{\partial}{\partial z} (f \cdot g) = \frac{\partial f}{\partial z} \cdot g + f \cdot \frac{\partial g}{\partial z} \quad (\text{A.6})$$

3. Chain rule

$$\frac{\partial}{\partial z}(f \circ g) = \left(\frac{\partial f}{\partial z} \circ g\right) \cdot \frac{\partial g}{\partial z} + \left(\frac{\partial f}{\partial z^*} \circ g\right) \cdot \frac{\partial g^*}{\partial z} \quad (\text{A.7})$$

For the proof, consider  $f \circ g = f(g(z, z^*), g^*(z, z^*))$ .

4. Complex conjugation

$$\left(\frac{\partial f}{\partial z}\right)^* = \frac{\partial f^*}{\partial z^*} \quad (\text{A.8})$$

5. If  $f$  is twice differentiable, then

$$\frac{\partial^2 f}{\partial z \partial z^*} = \frac{\partial^2 f}{\partial z^* \partial z} \quad (\text{A.9})$$

For higher-dimensional functions in  $\mathbb{C}^n$ , the Wirtinger derivatives are extended along each dimension

$$\frac{\partial}{\partial z_1}, \dots, \frac{\partial}{\partial z_n}, \frac{\partial}{\partial z_1^*}, \dots, \frac{\partial}{\partial z_n^*}. \quad (\text{A.10})$$

## A.2 Align reconstructions and remove ambiguities

Ptychography reconstructions are not unique and can be ambiguous. Compared to the true probe  $\hat{P}$  and object  $\hat{O}$ , the reconstructed probe  $P$  and object  $O$  have the following ambiguities:

$$P_{\mathbf{r}} O_{\mathbf{r}} = (a e^{ib} e^{i\mathbf{c}\mathbf{r}} \hat{P}_{\mathbf{r}+\mathbf{d}}) (a^{-1} e^{-ig} e^{-i\mathbf{c}\mathbf{r}} \hat{O}_{\mathbf{r}+\mathbf{d}}). \quad (\text{A.11})$$

- A scaling factor  $a$  between probe and object
- Global phases  $b$  and  $g$  of probe and object
- A phase gradient along the wave vector  $\mathbf{c}$
- The probe and object are translationally invariant and can be shifted by an arbitrary vector  $\mathbf{d}$

To compare different reconstructions, these ambiguities must be removed. A procedure to align the object is given by Maiden *et al.* [MJL17] and reproduced here to align the object  $O^{\text{unique}}$  to the true object  $\hat{O}$ :

1. Estimate the global translation  $\mathbf{d}$  by cross-correlation of the amplitude of  $P$  and  $\hat{P}$  to subpixel precision, for example with the method from Guizar-Sicairos *et al.* [GTF08].
2. Initialize  $O^{\text{unique}}$  from  $O$  and shift it by  $-\mathbf{d}$ .
3. Select a well reconstructed subregion  $\mathbf{x}_c$  from  $O^{\text{unique}}$  and  $\hat{O}$ .

4. Estimate the phase ramp  $\mathbf{c}$  by
  - a) Calculating  $L_{\mathbf{q}} = \mathcal{F} \left[ e^{i \arg(O_{\mathbf{x}_c}^{\text{unique}} \hat{O}_{\mathbf{x}_c}^*)} \right]$ ,
  - b) Locating the maximum of  $L$  with subpixel precision (for example by cross correlating it with the Fourier transform of a matrix of ones).
5. Multiply  $O^{\text{unique}}$  with a compensating phase ramp.
6. Estimate the global scaling factor with

$$ae^{ig} \approx \gamma = \frac{\sum_{\mathbf{x}_c} O_{\mathbf{x}_c}^{\text{unique}} \hat{O}_{\mathbf{x}_c}^*}{\sum_{\mathbf{x}_c} |O_{\mathbf{x}_c}^{\text{unique}}|^2}. \quad (\text{A.12})$$

7. Divide  $O^{\text{unique}}$  by  $\gamma$ .

The procedure to align the refractive object is equivalent, the exponential  $e^{i\tilde{O}}$  replaces  $O$  in multiplications and instead of dividing by  $\gamma$  at the end, the logarithm of  $\gamma$  is subtracted.

Holography and CXDI reconstructions are similarly ambiguous and can be aligned in an analogous way, except for the first step where the global shift  $\mathbf{d}$  is estimated. As there is no probe, the phases of the objects are cross-correlated instead. In general the phases are better reconstructed and contain more signal. CXDI has one additional ambiguity that needs to be considered, as flipping by  $180^\circ$  and complex conjugating the object creates the same diffraction pattern.

### A.3 Calculate reconstruction errors

The progress of the ptychography reconstruction can be tracked through the error between the measured and the simulated diffraction patterns. For this, the individual error  $E_i$  of the current diffraction pattern  $n_i$  is calculated in every subiteration. After the wavefield is propagated to the farfield and before it is updated in Equation 3.10, the error is calculated from

$$E_i = \sum_{\mathbf{q}} \left( |\Psi_{i,\mathbf{q}}| - \sqrt{n_{i,\mathbf{q}}} \right)^2. \quad (\text{A.13})$$

After all diffraction patterns have been used and the iteration is finished, the errors are averaged in the reconstruction error

$$E_{\text{diff}} = \frac{1}{N} \sum_i E_i. \quad (\text{A.14})$$

The error for CXDI is calculated between the reconstructed and the original object. The objects are aligned using the procedure described in Section A.2, before the errors are calculated according to

$$E_{\text{abs}} = \sum_{\mathbf{r} \in S} |\arg(\psi_{n,\mathbf{r}}) - \arg(O_{\mathbf{r}})|^2, \quad (\text{A.15a})$$

$$E_{\text{abs}} = \sum_{\mathbf{r} \in S} |\Re(\tilde{\psi}_{n,\mathbf{r}}) - \arg(O_{\mathbf{r}})|^2. \quad (\text{A.15b})$$

## B Abbreviations

<b>CRL</b> compound refractive lens .....	16
<b>CXDI</b> coherent X-ray diffraction imaging .....	35
<b>DM</b> difference-map .....	36
<b>DFT</b> discrete Fourier transform .....	53
<b>ePIE</b> extended Ptychographical Iterative Engine .....	22
<b>ESRF</b> European synchrotron radiation facility	
<b>FWHM</b> full width at half maximum .....	45
<b>FZP</b> Fresnel zone plate .....	16
<b>GPU</b> graphic processing unit	
<b>KB-mirror</b> Kirkpatrick-Baez-mirror .....	16
<b>NAG</b> Nesterov accelerated gradient .....	29
<b>NFH</b> inline near-field holography .....	51
<b>NFL</b> nano-focusing lens .....	19
<b>OAM</b> orbital angular momentum .....	82
<b>OSA</b> order-sorting aperture .....	18
<b>PETRA</b> Positron-Electron Tandem Ring Accelerator	
<b>PSI</b> Paul Scherrer Institute .....	73

<b>PtyNAMI</b>	ptychographic nano-analytical microscope .....	40
<b>RAAR</b>	relaxed averaged alternating reflections .....	65
<b>rCXDI</b>	refractive coherent diffractive imaging .....	65
<b>refPIE</b>	refractive ptychographical iterative engine .....	36
<b>rms</b>	root mean square .....	38
<b>sPIE</b>	sampling ptychographical iterative engine .....	28
<b>XFEL</b>	X-ray free-electron laser .....	81
<b>XPCT</b>	X-ray ptychographic computed tomography .....	41

# Bibliography

- [AO01] Allen, L. J. & Oxley, M. P. Phase retrieval from series of images obtained by defocus variation. *Opt. Commun.* **199**, 65–75 (2001).
- [AM11] Als-Nielsen, J. & McMorrow, D. *Elements of modern x-ray physics* 2nd ed. ISBN: 978-0-470-97395-0 (Wiley, 2011).
- [Bar+19] Barannikov, A. *et al.* Optical performance and radiation stability of polymer X-ray refractive nano-lenses. *J. Synchrotron Radiat.* **26**, 714–719 (2019).
- [Bat+14] Batey, D. J. *et al.* Reciprocal-space up-sampling from real-space oversampling in x-ray ptychography. *Phys. Rev. A* **89**, 043812 (2014).
- [BCR14] Batey, D. J., Claus, D. & Rodenburg, J. M. Information multiplexing in ptychography. *Ultramicroscopy* **138**, 13–21 (2014).
- [Bev+18] Bevis, C. *et al.* Multiple beam ptychography for large field-of-view, high throughput, quantitative phase contrast imaging. *Ultramicroscopy* **184**, 164–171 (2018).
- [BW99] Born, M. & Wolf, E. *Principles of optics: Electromagnetic theory of propagation, interference and diffraction of light* 7th ed. ISBN: 978-0-521-78449-8 (Cambridge University Press, 1999).
- [CN10] Chapman, H. N. & Nugent, K. A. Coherent lensless X-ray imaging. *Nat. Photonics* **4**, 833–839 (2010).
- [Cha+06] Chapman, H. N. *et al.* Femtosecond diffractive imaging with a soft-X-ray free-electron laser. *Nat. Phys.* **2**, 839–843 (2006).
- [CZ00] Chen, C. W. & Zebker, H. A. Network approaches to two-dimensional phase unwrapping: intractability and two new algorithms. *J. Opt. Soc. Am. A* **17**, 401 (2000).
- [Cho+19] Chowdhury, S. *et al.* High-resolution 3D refractive index microscopy of multiple-scattering samples from intensity images. *Optica* **6**, 1211 (2019).
- [Cla+14] Clark, J. N., Huang, X., Harder, R. J. & Robinson, I. K. Continuous scanning mode for ptychography. *Opt. Lett.* **39**, 6066–6069 (2014).

- [Clo+99] Cloetens, P. *et al.* Holotomography: Quantitative phase tomography with micrometer resolution using hard synchrotron radiation x rays. *Appl. Phys. Lett.* **75**, 2912–2914 (1999).
- [DL18] DESY & Lothringer, Cyprian. *Strukturanalyse von Biomolekülen mit Röntgenlicht* [https://www.desy.de/sites2009/site\\_www-desy/content/e201564/e301702/Infographics\\_Crystallography\\_gray\\_ger.jpg](https://www.desy.de/sites2009/site_www-desy/content/e201564/e301702/Infographics_Crystallography_gray_ger.jpg). 2018.
- [Dia+12] Diaz, A., Trtik, P., Guizar-Sicairos, M., Menzel, A., Thibault, P. & Bunk, O. Quantitative x-ray phase nanotomography. *Phys. Rev. B* **85**, 020104 (2012).
- [Dur+18] Durisova, J., Pudis, D., Gorau, M. & Gaso, P. IP-Dip photoresist surfaces for photonic applications prepared by laser lithography and studied by AFM. *Applied Surface Science* **461**, 108–112 (2018).
- [Eke+15] Ekeberg, T. *et al.* Three-dimensional reconstruction of the giant mimivirus particle with an X-Ray free-electron laser. *Phys. Rev. Lett.* **114**, 098102 (2015).
- [ERT07] Elser, V., Rankenburg, I. & Thibault, P. Searching with iterated maps. *Proc. Natl. Acad. Sci. USA* **104**, 418–423 (2007).
- [Els03] Elser, V. Phase retrieval by iterated projections. *J. Opt. Soc. Am. A* **20**, 40–55 (2003).
- [Gab48] Gabor, D. A new microscopic principle. *Nature* **161**, 777–778 (1948).
- [Gen+17] Genge, M. J., Larsen, J., Ginneken, M. V. & Suttle, M. D. An urban collection of modern-day large micrometeorites: Evidence for variations in the extraterrestrial dust flux through the Quaternary. *Geology* **45**, 119–122 (2017).
- [God+12] Godard, P., Allain, M., Chamard, V. & Rodenburg, J. Noise models for low counting rate coherent diffraction imaging. *Opt. Express* **20**, 25914–25934 (2012).
- [Goh17] Goh, G. Why momentum really works. *Distill* **2**, e6 (2017).
- [GZW88] Goldstein, R. M., Zebker, H. A. & Werner, C. L. Satellite radar interferometry: two-dimensional phase unwrapping. *Radio Sci.* **23**, 713–720 (1988).
- [Goo05] Goodman, J. W. *Introduction to Fourier Optics* 3rd ed. ISBN: 978-0-9747077-2-3 (Roberts & Co, Englewood, Colo, 2005).
- [GWD13] Grunwaldt, J.-D., Wagner, J. B. & Dunin-Borkowski, R. E. Imaging catalysts at work: a hierarchical approach from the macro- to the meso- and nano-scale. *ChemCatChem* **5**, 62–80 (2013).

- [GTF08] Guizar-Sicairos, M., Thurman, S. T. & Fienup, J. R. Efficient subpixel image registration algorithms. *Opt. Lett.* **33**, 156–158 (2008).
- [Gui+11] Guizar-Sicairos, M. *et al.* Phase tomography from x-ray coherent diffractive imaging projections. *Opt. Express* **19**, 21345–21357 (2011).
- [Gür17] Gürsoy, D. Direct coupling of tomography and ptychography. *Opt. Lett.* **42**, 3169–3172 (2017).
- [HS17] Hagemann, J. & Salditt, T. The fluence–resolution relationship in holographic and coherent diffractive imaging. *J. Appl. Crystallogr.* **50**, 531–538 (2017).
- [Hir+20] Hirose, M., Higashino, T., Ishiguro, N. & Takahashi, Y. Multibeam ptychography with synchrotron hard X-rays. *Opt. Express* **28**, 1216–1224 (2020).
- [Hir+17] Hirose, M., Shimomura, K., Burdet, N. & Takahashi, Y. Use of Kramers–Kronig relation in phase retrieval calculation in X-ray spectro-ptychography. *Opt. Express* **25**, 8593–8603 (2017).
- [Hol+12] Holler, M. *et al.* An instrument for 3D x-ray nano-imaging. *Rev. Sci. Instrum.* **83**, 073703 (2012).
- [Hön10] Hönig, W. *Portierung einer Ptychographie-Anwendung auf das CUDA GPU-Modell* Großer Beleg (Technische Universität Dresden, 2010).
- [Hop+13] Hoppe, R. *et al.* High-resolution chemical imaging of gold nanoparticles using hard x-ray ptychography. *Appl. Phys. Lett.* **102**, 203104 (2013).
- [Hop19] Hoppe, R. *Anpassung und Optimierung des ptychographischen Modells für die quantitative Mikroskopie mit kohärenter Röntgenstrahlung und sichtbarem Laserlicht* Dissertation (Universität Hamburg, 2019).
- [Hop69] Hoppe, W. Beugung im inhomogenen Primärstrahlwellenfeld. I. Prinzip einer Phasenmessung von Elektronenbeugungsinterferenzen. *Acta Crystallogr. A* **25**, 495–501 (1969).
- [Jac99] Jackson, J. D. *Classical electrodynamics* 3rd ed. ISBN: 978-0-471-30932-1 (Wiley, New York, 1999).
- [Jan+13] Janssens, K. *et al.* The use of synchrotron radiation for the characterization of artists' pigments and paintings. *Annu. Rev. Anal. Chem.* **6**, 399–425 (2013).
- [Joh+14] Johnson, I. *et al.* Eiger: a single-photon counting x-ray detector. *J. Instrum.* **9**, C05032 (2014).

- [Kah+19] Kahnt, M. *et al.* Coupled ptychography and tomography algorithm improves reconstruction of experimental data. *Optica* **6**, 1282–1289 (2019).
- [KB48] Kirkpatrick, P. & Baez, A. V. Formation of optical images by X-Rays. *J. Opt. Soc. Am.* **38**, 766–774 (1948).
- [Kir74] Kirz, J. Phase zone plates for x rays and the extreme uv. *J. Opt. Soc. Am.* **64**, 301–309 (1974).
- [Len+05] Lengeler, B. *et al.* Refractive x-ray lenses. *J. Phys. D: Appl. Phys.* **38**, A218–A222 (2005).
- [Lyu+19] Lyubomirskiy, M. *et al.* Ptychographic characterisation of polymer compound refractive lenses manufactured by additive technology. *Opt. Express* **27**, 8639–8650 (2019).
- [MHR12] Maiden, A. M., Humphry, M. J. & Rodenburg, J. M. Ptychographic transmission microscopy in three dimensions using a multi-slice approach. *J. Opt. Soc. Am. A* **29**, 1606–1614 (2012).
- [Mai+12] Maiden, A. M., Humphry, M. J., Sarahan, M. C., Kraus, B. & Rodenburg, J. M. An annealing algorithm to correct positioning errors in ptychography. *Ultramicroscopy* **120**, 64–72 (2012).
- [MR09] Maiden, A. M. & Rodenburg, J. M. An improved ptychographical phase retrieval algorithm for diffractive imaging. *Ultramicroscopy* **109**, 1256–1262 (2009).
- [MJL17] Maiden, A., Johnson, D. & Li, P. Further improvements to the ptychographical iterative engine. *Optica* **4**, 736–745 (2017).
- [Mar07] Marchesini, S. Invited article: a unified evaluation of iterative projection algorithms for phase retrieval. *Rev. Sci. Instrum.* **78**, 011301 (2007).
- [McN+92] McNulty, I., Kirz, J., Jacobsen, C., Anderson, E. H., Howells, M. R. & Kern, D. P. High-resolution imaging by fourier transform X-ray holography. *Science* **256**, 1009–1012 (1992).
- [MKS00] Miao, J., Kirz, J. & Sayre, D. The oversampling phasing method. *Acta Crystallogr. D* **56**, 1312–1315 (2000).
- [Mia+99] Miao, J., Charalambous, P., Kirz, J. & Sayre, D. Extending the methodology of X-ray crystallography to allow imaging of micrometre-sized non-crystalline specimens. *Nature* **400**, 342–344 (1999).
- [Mic91] Michette, A. G. No X-ray lens. *Nature* **353**, 510 (1991).

- [Mis73] Misell, D. L. A method for the solution of the phase problem in electron microscopy. *J. Phys. D: Appl. Phys.* **6**, L6–L9 (1973).
- [Mor15] Moriarty, J. *The Dynamics of an Asteroid* (George H. Doran Company, 1915).
- [New+10] Newton, M. C., Leake, S. J., Harder, R. & Robinson, I. K. Three-dimensional imaging of strain in a single ZnO nanorod. *Nat. Mater.* **9**, 120–124 (2010).
- [OHG18] Odstrčil, M., Holler, M. & Guizar-Sicairos, M. Arbitrary-path fly-scan ptychography. *Opt. Express* **26**, 12585–12593 (2018).
- [OS08] Oszlányi, G. & Sütő, A. The charge flipping algorithm. *Acta Crystallogr. A* **64**, 123–134 (2008).
- [Pat+17] Patommel, J. *et al.* Focusing hard x rays beyond the critical angle of total reflection by adiabatically focusing lenses. *Appl. Phys. Lett.* **110**, 101103 (2017).
- [Pel+14] Pelz, P. M., Guizar-Sicairos, M., Thibault, P., Johnson, I., Holler, M. & Menzel, A. On-the-fly scans for X-ray ptychography. *Appl. Phys. Lett.* **105**, 251101 (2014).
- [Pet+17] Petrov, A. K. *et al.* Polymer X-ray refractive nano-lenses fabricated by additive technology. *Opt. Express* **25**, 14173–14181 (2017).
- [Pfe18] Pfeiffer, F. X-ray ptychography. *Nat. Photonics* **12**, 9–17 (2018).
- [Rai16] Raimondi, P. ESRF-EBS: The Extremely Brilliant Source Project. *Synchrotron Radiation News* **29**, 8–15 (2016).
- [Rei+17] Reinhardt, J. *et al.* Beamstop-based low-background ptychography to image weakly scattering objects. *Ultramicroscopy* **173**, 52–57 (2017).
- [RS13] Remmert, R. & Schumacher, G. *Funktionentheorie 1* 5th ed. ISBN: 978-3-540-41855-9 (Springer Berlin Heidelberg, 2013).
- [RM19] Rodenburg, J. & Maiden, A. in *Springer Handbook of Microscopy* (eds Hawkes, P. W. & Spence, J. C. H.) 2–2 (Springer International Publishing, Cham, 2019). ISBN: 978-3-030-00069-1.
- [Rön95] Röntgen, W. C. Ueber eine neue Art von Strahlen. (Vorläufige Mittheilung.) *Aus den Sitzungsberichten der Würzburger Physik.-medic. Gesellschaft Würzburg* **137**, 132–141 (1895).
- [Rud17] Ruder, S. An overview of gradient descent optimization algorithms. *arXiv:1609.04747 [cs]*. arXiv: 1609.04747 [cs] (2017).
- [SA10] Sakdinawat, A. & Attwood, D. Nanoscale X-ray imaging. *Nat. Photonics* **4**, 840–848 (2010).

- [SR69] Schmahl, G. & Rudolph, D. Lichtstarke Zoneplatten als abbildende Systeme für weiche Röntgenstrahlung. *Optik* **29**, 577–585 (1969).
- [Sch14] Scholz, M. *Refraktive Lamellarlinsen (RLL) für die Mikroskopie mit harter Röntgenstrahlung* Diploma Thesis (Technische Universität Dresden, Institute of Structural Physics, 2014).
- [Sch+03] Schroer, C. G. *et al.* Nanofocusing parabolic refractive x-ray lenses. *Appl. Phys. Lett.* **82**, 1485–1487 (2003).
- [Sch+08] Schroer, C. G. *et al.* Coherent X-ray diffraction imaging with nanofocused illumination. *Phys. Rev. Lett.* **101**, 090801 (2008).
- [Sch+16] Schroer, C. G. *et al.* Hard x-ray nanoprobe of beamline P06 at PETRA III. *AIP Conf. Proc.* **1741**, 030007 (2016).
- [SL12] Schroer, C. G. & Lengeler, B. in *Springer Handbook of Lasers and Optics* (ed Träger, F.) 1461–1474 (Springer Berlin Heidelberg, 2012). ISBN: 978-3-642-19409-2.
- [Sch+17] Schroer, C. G. *et al.* PtyNAMi: Ptychographic Nano-Analytical Microscope at PETRA III: interferometrically tracking positions for 3D x-ray scanning microscopy using a ball-lens retroreflector in *X-Ray Nanoimaging: Instruments and Methods III* **10389** (SPIE, 2017), 8–17.
- [Sch+19a] Schroer, C. G. *et al.* Ptychographic Nano-Analytical Microscope (PtyNAMi) at PETRA III: signal-to-background optimization for imaging with high sensitivity in *X-Ray Nanoimaging: Instruments and Methods IV* **11112** (International Society for Optics and Photonics, 2019), 111120D.
- [Sch+19b] Schroer, C. *et al.* *PETRA IV: Upgrade of PETRA III to the Ultimate 3D X-ray Microscope - Conceptual Design Report (CDR)* pages 259 (Deutsches Elektronen-Synchrotron, DESY, Hamburg, 2019).
- [Sch+12] Schropp, A. *et al.* Hard x-ray scanning microscopy with coherent radiation: Beyond the resolution of conventional x-ray microscopes. *Appl. Phys. Lett.* **100**, 253112 (2012).
- [Sch+13] Schropp, A. *et al.* Full spatial characterization of a nanofocused x-ray free-electron laser beam by ptychographic imaging. *Sci. Rep.* **3**, 1633 (2013).
- [Sch+20] Schropp, A. *et al.* PtyNAMi: ptychographic nano-analytical microscope. *J. Appl. Crystallogr.* **53**, 957–971 (2020).
- [Sei+14] Seiboth, F. *et al.* Hard x-ray nanofocusing by refractive lenses of constant thickness. *Appl. Phys. Lett.* **105**, 131110 (2014).

- [Sei+17] Seiboth, F. *et al.* Perfect X-ray focusing via fitting corrective glasses to aberrated optics. *Nat. Commun.* **8**, 14623 (2017).
- [Sei+19] Seiboth, F. *et al.* Refractive hard x-ray vortex phase plates. *Opt. Lett.* **44**, 4622–4625 (2019).
- [Sha49] Shannon, C. E. Communication in the presence of noise. *Proc. IRE* **37**, 10–21 (1949).
- [Sha+05] Shapiro, D. *et al.* Biological imaging by soft x-ray diffraction microscopy. *Proc. Natl. Acad. Sci. USA* **102**, 15343–15346 (2005).
- [She+15] Shechtman, Y., Eldar, Y. C., Cohen, O., Chapman, H. N., Miao, J. & Segev, M. Phase retrieval with application to optical imaging: a contemporary overview. *IEEE Signal Process. Mag.* **32**, 87–109 (2015).
- [Shv+10] Shvyd'ko, Y. V., Stoupin, S., Cunsolo, A., Said, A. H. & Huang, X. High-reflectivity high-resolution X-ray crystal optics with diamonds. *Nat. Phys.* **6**, 196–199 (2010).
- [Sni+96] Snigirev, A., Kohn, V., Snigireva, I. & Lengeler, B. A compound refractive lens for focusing high-energy X-rays. *Nature* **384**, 49–51 (1996).
- [Sto+15] Stockmar, M. *et al.* X-Ray near-field ptychography for optically thick specimens. *Phys. Rev. Appl.* **3**, 014005 (2015).
- [Tav+18] Tavares, P. F. *et al.* Commissioning and first-year operational results of the MAX IV 3 GeV ring. *J. Synchrotron Radiat.* **25**, 1291–1316 (2018).
- [Tay03] Taylor, G. The phase problem. *Acta Crystallogr. B* **59**, 1881–1890 (2003).
- [TLH98] Taylor, S., Lever, J. H. & Harvey, R. P. Accretion rate of cosmic spherules measured at the South Pole. *Nature* **392**, 899–903 (1998).
- [TG12] Thibault, P. & Guizar-Sicairos, M. Maximum-likelihood refinement for coherent diffractive imaging. *New J. Phys.* **14**, 063004 (2012).
- [Thi+09] Thibault, P., Dierolf, M., Bunk, O., Menzel, A. & Pfeiffer, F. Probe retrieval in ptychographic coherent diffractive imaging. *Ultramicroscopy* **109**, 338–343 (2009).
- [Thi+08] Thibault, P., Dierolf, M., Menzel, A., Bunk, O., David, C. & Pfeiffer, F. High-resolution scanning X-ray diffraction microscopy. *Science* **321**, 379–382 (2008).
- [TM13] Thibault, P. & Menzel, A. Reconstructing state mixtures from diffraction measurements. *Nature* **494**, 68–71 (2013).
- [Tho+09] Thompson, A. C. *et al.* *X-ray data booklet* 3rd ed (Lawrence Berkeley National Laboratory, University of California Berkeley, CA, 2009).

- [Wei+12] Weinhausen, B. *et al.* X-ray nano-diffraction on cytoskeletal networks. *New J. Phys.* **14**, 085013 (2012).
- [Wei+19] Weissenberger, T. *et al.* Synthesis and characterisation of hierarchically structured titanium silicalite-1 zeolites with large intracrystalline macropores. *Chem. Eur. J.* **25**, 14430–14440 (2019).
- [Wir27] Wirtinger, W. Zur formalen Theorie der Funktionen von mehr komplexen Veränderlichen. *Math. Ann.* **97**, 357–375 (1927).
- [Yan+11] Yang, C., Qian, J., Schirotzek, A., Maia, F. & Marchesini, S. Iterative Algorithms for Ptychographic Phase Retrieval. *arXiv:1105.5628 [physics]*. arXiv: 1105.5628 [physics] (2011).
- [Zab+05] Zabler, S., Cloetens, P., Guigay, J.-P., Baruchel, J. & Schlenker, M. Optimization of phase contrast imaging using hard x rays. *Rev. Sci. Instrum.* **76**, 073705 (2005).
- [Zam+18] Zambon, P., Radicci, V., Rissi, M. & Broennimann, C. A fitting model of the pixel response to monochromatic X-rays in photon counting detectors. *Nucl. Instrum. Meth. A* **905**, 188–192 (2018).
- [Zha+13] Zhang, F. *et al.* Translation position determination in ptychographic coherent diffraction imaging. *Opt. Express* **21**, 13592–13606 (2013).
- [Zha+17] Zhao, C. *et al.* Real-time monitoring of laser powder bed fusion process using high-speed X-ray imaging and diffraction. *Sci. Rep.* **7**, 3602 (2017).

# List of Publications

- Kahnt, M., Grote, L., Brückner, D., Seyrich, M., Wittwer, F., Koziej, D. & Schroer, C. G. Multi-slice ptychography enables high-resolution measurements in extended chemical reactors. *Sci. Rep.* **11**, 1500 (2021).
- Schropp, A., Döhrmann, R., Botta, S., Brückner, D., Kahnt, M., Lyubomirskiy, M., Ossig, C., Scholz, M., Seyrich, M., Stuckelberger, M. E., Wiljes, P., Wittwer, F., Garrevoet, J., Falkenberg, G., Fam, Y., Sheppard, T. L., Grunwaldt, J.-D. & Schroer, C. G. PtyNAMi: ptychographic nano-analytical microscope. *J. Appl. Crystallogr.* **53**, 957–971 (2020).
- Seiboth, F., Brückner, D., Kahnt, M., Lyubomirskiy, M., Wittwer, F., Dzhigaev, D., Ullsperger, T., Nolte, S., Koch, F., David, C., Garrevoet, J., Falkenberg, G. & Schroer, C. G. Hard X-ray wavefront correction via refractive phase plates made by additive and subtractive fabrication techniques. *J. Synchrotron Radiat.* **27** (2020).
- Fam, Y., Sheppard, T. L., Becher, J., Scherhauser, D., Lambach, H., Kulkarni, S., Keller, T. F., Wittstock, A., Wittwer, F., Seyrich, M., Brueckner, D., Kahnt, M., Yang, X., Schropp, A., Stierle, A., Schroer, C. G. & Grunwaldt, J.-D. A versatile nanoreactor for complementary in situ X-ray and electron microscopy studies in catalysis and materials science. *J. Synchrotron Radiat.* **26** (2019).
- Kahnt, M., Becher, J., Brückner, D., Fam, Y., Sheppard, T., Weissenberger, T., Wittwer, F., Grunwaldt, J.-D., Schwieger, W. & Schroer, C. G. Coupled ptychography and tomography algorithm improves reconstruction of experimental data. *Optica* **6**, 1282–1289 (2019).
- Lyubomirskiy, M., Koch, F., Abrashitova, K. A., Bessonov, V. O., Kokareva, N., Petrov, A., Seiboth, F., Wittwer, F., Kahnt, M., Seyrich, M., Fedyanin, A. A., David, C. & Schroer, C. G. Ptychographic characterisation of polymer compound refractive lenses manufactured by additive technology. *Opt. Express* **27**, 8639–8650 (2019).
- Schroer, C. G., Seyrich, M., Schropp, A., Döhrmann, R., Botta, S., Wiljes, P., Brückner, D., Kahnt, M., Wittwer, F., Grote, L., Koziej, D., Garrevoet, J. & Falkenberg, G. *Ptychographic Nano-Analytical Microscope (PtyNAMi) at PETRA III: signal-to-background optimization for imaging with high sensitivity in X-Ray*

- Nanoimaging: Instruments and Methods IV 11112* (International Society for Optics and Photonics, 2019), 111120D.
- Seiboth, F., Kahnt, M., Lyubomirskiy, M., Seyrich, M., Wittwer, F., Ullsperger, T., Nolte, S., Batey, D., Rau, C. & Schroer, C. G. Refractive hard x-ray vortex phase plates. *Opt. Lett.* **44**, 4622–4625 (2019).
- Kahnt, M., Falkenberg, G., Garrevoet, J., Hartmann, J., Krause, T., Niehle, M., Scholz, M., Seyrich, M., Trampert, A., Waag, A., Wehmann, H.-H., Wittwer, F., Zhou, H., Hanke, M. & Schroer, C. G. Simultaneous hard X-ray ptychographic tomography and X-ray fluorescence tomography of isolated hollow core-shell GaN rods. *Microsc. Microanal.* **24**, 34–35 (2018).
- Schropp, A., Bruckner, D., Bulda, J., Falkenberg, G., Garrevoet, J., Seiboth, F., Wittwer, F., Koch, F., David, C. & Schroer, C. G. Scanning hard X-ray microscopy based on Be CRLs. *Microsc. Microanal.* **24**, 188–189 (2018).
- Seiboth, F., Wittwer, F., Scholz, M., Kahnt, M., Seyrich, M., Schropp, A., Wagner, U., Rau, C., Garrevoet, J., Falkenberg, G. & Schroer, C. G. Nanofocusing with aberration-corrected rotationally parabolic refractive X-ray lenses. *J. Synchrotron Radiat.* **25** (2018).
- Stuckelberger, M. E., Nietzold, T., West, B. M., Walker, T., Ossig, C., Kahnt, M., Wittwer, F., Deng, J., Maser, J. M., Lai, B., Cai, Z., Rose, V., Ulvestad, A., Holt, M. V., Hruszkewycz, S., Dynes, J. J., Wang, J., Salomon, D., Tucoulou, R., Huang, X., Yan, H., Nazaretski, E., Chu, Y. S., Schroer, C. G. & Bertoni, M. I. Challenges and opportunities with highly brilliant X-ray sources for multi-modal in-situ and operando characterization of solar cells. *Microsc. Microanal.* **24**, 434–435 (2018).
- Wittwer, F., Hoppe, R., Seiboth, F., Reinhardt, J., Scholz, M. & Schroer, C. G. Ptychography with a virtually enlarged illumination. *Microsc. Microanal.* **24**, 48–49 (2018).
- Bernert, C., Hoppe, R., Wittwer, F., Woike, T. & Schroer, C. G. Ptychographic analysis of the photorefractive effect in LiNbO<sub>3</sub>:Fe. *Opt. Express* **25**, 31640–31650 (2017).
- Patommel, J., Klare, S., Hoppe, R., Ritter, S., Samberg, D., Wittwer, F., Jahn, A., Richter, K., Wenzel, C., Bartha, J. W., Scholz, M., Seiboth, F., Boesenberg, U., Falkenberg, G. & Schroer, C. G. Focusing hard x rays beyond the critical angle of total reflection by adiabatically focusing lenses. *Appl. Phys. Lett.* **110**, 101103 (2017).
- Schroer, C. G., Seyrich, M., Kahnt, M., Botta, S., Döhrmann, R., Falkenberg, G., Garrevoet, J., Lyubomirskiy, M., Scholz, M., Schropp, A. & Wittwer, F. *PtyNAMI: Ptychographic Nano-Analytical Microscope at PETRA III: interferometrically tracking*

positions for 3D x-ray scanning microscopy using a ball-lens retroreflector in *X-Ray Nanoimaging: Instruments and Methods III* **10389** (SPIE, 2017), 8–17.

Seiboth, F., Schropp, A., Scholz, M., Wittwer, F., Rödel, C., Wünsche, M., Ullsperger, T., Nolte, S., Rahomäki, J., Parfeniukas, K., Giakoumidis, S., Vogt, U., Wagner, U., Rau, C., Boesenberg, U., Garrevoet, J., Falkenberg, G., Galtier, E. C., Lee, H. J., Nagler, B. & Schroer, C. G. *Aberration correction for hard x-ray focusing at the nanoscale in Advances in X-Ray/EUV Optics and Components XII* **10386** (SPIE, 2017), 41–50.

Seiboth, F., Schropp, A., Scholz, M., Wittwer, F., Rödel, C., Wünsche, M., Ullsperger, T., Nolte, S., Rahomäki, J., Parfeniukas, K., Giakoumidis, S., Vogt, U., Wagner, U., Rau, C., Boesenberg, U., Garrevoet, J., Falkenberg, G., Galtier, E. C., Ja Lee, H., Nagler, B. & Schroer, C. G. Perfect X-ray focusing via fitting corrective glasses to aberrated optics. *Nat. Commun.* **8**, 14623 (2017).

Parfeniukas, K., Rahomäki, J., Giakoumidis, S., Seiboth, F., Wittwer, F., Schroer, C. G. & Vogt, U. Improved tungsten nanofabrication for hard X-ray zone plates. *Microelectronic Engineering* **152**, 6–9 (2016).

Schroer, C. G., Baumbach, C., Döhrmann, R., Klare, S., Hoppe, R., Kahnt, M., Patommel, J., Reinhardt, J., Ritter, S., Samberg, D., Scholz, M., Schropp, A., Seiboth, F., Seyrich, M., Wittwer, F. & Falkenberg, G. Hard x-ray nanoprobe of beamline P06 at PETRA III. *AIP Conf. Proc.* **1741**, 030007 (2016).

Seiboth, F., Kahnt, M., Scholz, M., Seyrich, M., Wittwer, F., Garrevoet, J., Falkenberg, G., Schropp, A. & Schroer, C. G. *Quantitative characterization of aberrations in x-ray optics in Advances in X-Ray/EUV Optics and Components XI* **9963** (SPIE, 2016), 88–95.



# Danksagung

Dass diese Arbeit nach fünf Jahren endlich fertig ist, wäre nicht möglich gewesen ohne die Unterstützung und Mithilfe vieler Menschen. Ich möchte ihnen allen dafür von ganzem Herzen danken.

Ich danke an erster Stelle Prof. Christian Schroer für die Betreuung, Unterstützung, Rat und Motivation während der Promotion, auch wenn sein Postfach und Terminkalender wieder mal überquillte. Seine Ermutigungen und Erfahrungen haben über manchen Fehlschlag hinweggeholfen und sein Optimismus hat die gesamte Arbeitsgruppe positiv geprägt. Ich danke Dr. Andreas Schropp für seine Geduld, Erfahrung und Hilfsbereitschaft in allen Fragen, vor allem wenn Christian verhindert war und Deadlines mal wieder bedrohlich näher tickten. Mein Dank gebührt auch Prof. Peter Modregger für die Übernahme des Zweitgutachtens, für seine Nachsicht, Geduld und Inspiration zu neuen Ideen. Ich danke allen weiteren Gutachtern und Mitgliedern der Prüfungskommission dafür, dass sie sich die Zeit für diese Promotion genommen haben.

Mein besonderer Dank geht an alle Mitglieder der Arbeitsgruppe, die sie zu der offenen und hilfsbereiten Umgebung machen die sie auszeichnet und die zusammen dafür sorgen, dass man sich auch bei typischem Hamburgwetter auf die Fahrt ins Büro freuen kann. Ich danke den jetzigen und ehemaligen Doktoranden, Juliane, Maik, Maria, Martin, Dennis, Christina und Saba, denn geteiltes Leid ist halbes Leid und geteilte Freude doppelte Freude. Das Wissen das andere gerade dieselben Probleme und Schwierigkeiten haben oder hatten, hat über manche Hürde hinweggeholfen. An dieser Stelle eine kurze Aufmunterung an alle, die auch gerade beim Schreiben sind und das Ziel fast vor Augen haben. Danke für die schöne Zeit auch abseits von Arbeit und Röntgenstrahlung, die mit Ausflügen, vielen gemeinsamen Abendessen, Laufen oder Klettern gefüllt wurde. Ein Extradank noch an Maik und Martin für die gegenseitige Rückhilfe auf dem Hamburger Wohnungsmarkt. Ich danke Frank, Johannes, Mikhail, Xiaogang und Michael, die das alles schon lange hinter sich haben und ihre Erfahrung und Ratschlägen gerne geteilt haben.

Die Experimente an PETRA waren oft geprägt von kurzfristigen Änderungen und Unvorhergesehenem, in solchen Momenten war es gut, dass man sich auf das Ingenieurteam von Ralph, Stephan und Patrik verlassen konnte, die schnell wussten was zu tun war und die in der Bürokratie bei Desy manche Abkürzung kannten. Im selben Zug möchte ich Christina Newiger und Julia Barth danken, die mir bei Anträgen und

Formularen aus der Patsche geholfen haben.

Ich möchte allen in der alten und neuen Dresdner Gruppe danken, insbesondere Robert Hoppe und Jens Patommel, sowie Dirk Samberg und Jochen Geck. In der Zeit bei Desy war ich an unzähligen Messzeiten an P06 beteiligt, die ohne die Unterstützung von Gerald, Kathryn und Jan nicht möglich gewesen wären. Im selben Atemzug will ich auch den Teams an allen anderen Beamlines, an denen ich gemessen habe, danken. Ich danke auch den verschiedenen IT-Zuständigen, die bei manchem Problem zu später Stunde ausgeholfen haben. Ich danke meinen Editoren Louise, Florian, Martin und Oliver für sehr lehrreiche Diskussionen über die Englische Sprache bei denen oft kein Wort auf dem anderen blieb, sowie meinen Korrekturlesern Juliane, Maik, Martin, Maria und Johannes für ihre gründliche Fehlersuche.

Zum Schluss möchte ich noch meiner Familie und meinen Freunden für die langjährige Unterstützung und Nachsicht danken, ohne die all das nie möglich gewesen wäre.

# Eidesstattliche Versicherung

Hiermit erkläre ich an Eides statt, dass ich die vorliegende Dissertationsschrift selbst verfasst und keine anderen als die angegebenen Quellen und Hilfsmittel benutzt habe.

Hamburg, den 15. Oktober 2020

---

Felix Wittwer